

**Motion-Robust Pulse Design for Parallel
Transmission Excitation at Ultra-High Field
MRI**

May 2023

Luke Watkins

A thesis presented for the degree of
Doctor of Philosophy

School of Physics and Astronomy
Cardiff University

Acknowledgements

I would like to take this opportunity to thank my supervisors Emre Kopanoglu and Kevin Murphy for their support and invaluable mentoring throughout my time at Cardiff. I would also like to thank my fellow PhD students Alix Plumley and Ryan Beckerleg, who were always willing to help with anything. This extends to everybody who worked at Cardiff University Brian Research Imaging Centre (CUBRIC) during my time there, I cannot imagine a nicer and more inspiring group of people to be surrounded by while embarking on my most difficult challenge yet. I would also like to thank the Engineering and Physical Sciences Research Council (EPSRC), Cardiff University School of Physics and Astronomy, and Cardiff University School of Psychology, for their sponsorship.

Finally I would like to thank my family, my mum Sue, my dad David, my brother Adam, my cousin Hannah and her husband Tom, my friends Oliver and Luke, and my girlfriend Rebeca, whose emotional support during a challenging time meant the world to me.

Thesis Summary

Ultra-high field (UHF) MRI offers higher signal-to-noise and contrast-to-noise ratios compared to lower B_0 -field strengths, which can be leveraged for improved spatial or temporal resolution, but suffers from B_1^+ -field inhomogeneity, which can lead to artificial signal and contrast variations in an image. Parallel transmission excitation (pTx) systems allow non-identical radiofrequency (RF) pulses to be simultaneously applied, reducing excitation pulse duration, and increasing global excitation homogeneity, which can reduce image artifacts related to B_1^+ -field inhomogeneity at UHF.

Within-scan patient head motion can lead to imaging artifacts such as blurring or aliasing. Variation in image contrast caused by patient motion is related to the RF excitation, therefore requires prospective motion correction to recover contrast homogeneity. The added complexity of pulse design for pTx increases computation times past what is feasible for typical prospective motion correction, therefore an alternative method is required.

In this thesis, a method was demonstrated in-silico for reducing the effects of patient head motion on radiofrequency field homogeneity for pTx. This was achieved by designing motion robust pulses (MRPs), which were optimised over the centred head position, and off-centre positions during initial pulse design, using B_1^+ -maps simulated within a generic 8-channel pTx transmit array. The MRPs required multiple input B_1^+ -maps which would increase scan complexity. Recent literature has been published demonstrating how a deep learning neural network could be used to estimate off-centre B_1^+ -maps from a single B_1^+ -map, collected at the centred position. This could improve the practicality of the MRPs, and would allow any desired combination of input B_1^+ -maps. MRPs were designed using off-centre B_1^+ -maps estimated from the centred position, and evaluated over simulated positions. Finally, a pseudo in-vivo investigation

of the MRP design was performed using ten B_1^+ -maps collected in-vivo using an 8-32-channel pTx/Rx coil (Nova Medical, MA, USA) within a Siemens 7T Magnetom scanner (Siemens Healthcare, Erlangen, Germany).

Contents

List of Figures	7
1 Introduction	24
1.1 MR Signal	25
1.2 RF Excitation Pulses	30
1.3 Gradients	31
1.4 k-Space	33
1.5 Ultra-High Field MRI	34
1.6 Parallel Transmission Excitation	35
1.7 Slice Selective Excitation and Spokes Pulses	36
1.8 Specific Absorption Rate	39
1.9 Effects of Patient Motion	41
1.10 Current Motion Correction Techniques for pTx	43
1.11 Thesis Overview	44
2 Motion-Robust pTx Excitation Pulse Design: In-Silico Proof of Concept	46
2.1 Introduction	46
2.2 Methods	49
2.2.1 Phase-Relaxed Motion-Robust Pulses	49

2.3	Results	56
2.3.1	3-spoke MRPs vs 3-spoke Ref-Pulses	56
2.3.2	Adding Additional Spokes	65
2.4	Discussion	70
2.5	Conclusion	73
3	Non-Phase-Relaxed Motion-Robust Pulses, with Optimisation of Candidate Spoke Selection	74
3.1	Introduction	74
3.2	Methods	76
3.3	Results	79
3.4	Discussion	95
3.5	Conclusion	99
4	Motion-Robust pTx Excitation Pulse Design Using Estimated B_1^+-maps Predicted Using Deep Learning	100
4.1	Introduction	100
4.2	Methods	102
4.3	Results	108
4.3.1	MRPs _{set-1} : 23 Design Positions	108
4.3.2	MRPs _{set-2} : 18 Design Positions	118
4.3.3	MRPs _{set-3} : 10 Design Positions	125
4.3.4	SAR	132
4.4	Discussion	135
4.5	Conclusion	140
5	Motion-Robust pTx Excitation Pulse Design Using In-Vivo B_1^+- maps Collected at 7T	141
5.1	Introduction	141

5.2	Methods	142
5.2.1	B_1 Data Collection	142
5.2.2	Pulse Design	143
5.3	Results	145
5.4	Discussion	153
5.5	Conclusion	156
6	Conclusion	157
6.1	Thesis Summary	157
6.2	Possible Future Directions	160
	Bibliography	164

List of Figures

2.1	The Ella body model inside the generic 8-channel pTx coil designed in Sim4Life (panel a), slice positions (panel b), slice thickness not to scale, and the positions of the centred and 52 off-centre B_1^+ -map simulations (panel c). The displacements shown are for demonstration purposes, and are not to scale.	50
2.2	Magnitude (top) and phase (bottom) profiles of the flip-angle at the centered position for each of the slice specific 3-spoke reference pulses. Magnitude nRMSEs for slices 1 to 6 (left to right) were 4.2%, 9.1%, 9.6%, 7.6%, 7.0%, 4.5% respectively. There was no associated phase error for the centred positions, as discussed in the text.	56

2.3	Magnitude profiles for all 13 positions used in pulse design for each of the six slice-specific 3-spoke MRPs. The slice with the lowest mean nRMSE (averaged across positions) was slice 5 (indicated in green), and the slice with the largest mean nRMSE is indicated in red. Magnitude nRMSE for the centred positions in slices 1 to 6 were 9.0%, 8.4%, 7.7%, 6.9%, 3.6%, and 5.5%, respectively. Off-centre magnitude nRMSE ranged between, 9.0%-22.1%, 8.1%-17.5%, 7.5%-16.3%, 6.6%-16.9%, 3.6%-10.1%, and 5.5%-14.0%, for slices 1 to 6 respectively.	58
2.4	Phase profiles for all 13 positions used in pulse design for each of the six slice-specific 3-spoke MRPs. Off-centre phase RMSE, calculated relative to the phase distribution at the centred position, ranged between $1.8^\circ - 10^\circ$, $0.9^\circ - 15.1^\circ$, $0.5^\circ - 12.5^\circ$, $0.6^\circ - 12.2^\circ$, $0.9^\circ - 15.4^\circ$, and $2.3^\circ - 17.3^\circ$, for slices 1 to 6 respectively. The slice with the lowest mean RMSE (averaged across positions) is indicated in green, and the slice with the largest mean RMSE is indicated in red.	59
2.5	Magnitude nRMSE (panel a) and phase RMSE (panel b) across all design positions for all six slice-selective MRPs. For magnitude nRMSE, slice 1 had the largest range (9.0%-22.1%), and slice 5 the least (3.6%-10.1%). Slice 1 had the largest mean magnitude nRMSE across positions (12.7%, $\sigma = 3.7$), and slice 5 the least (6.3%, $\sigma = 2.0$). For phase RMSE, slice 6 had the largest range ($2.3^\circ - 17.3^\circ$), and slice 1 the least ($1.8^\circ - 10.0^\circ$). Slice 5 had the largest mean phase RMSE across positions (5.6° , $\sigma = 4.3$), and slice 4 the least (3.7° , $\sigma = 3.3$).	60

2.6	Magnitude nRMSE (panel a) and phase RMSE (panel b) for each motion type included in the MRP design, across all slice-selective MRPs. Pitch, roll and yaw rotations ($^{\circ}$) and left-right (LR), anterior-posterior (AP) and superior-inferior (SI) translations (mm). For magnitude nRMSE, overall, roll rotations had the largest nRMSE averaged (mean) across positions (14.1%, $\sigma = 2.2$), and the centred positions the smallest (6.9% $\sigma = 1.8$). For overall phase RMSE, pitch rotations had the largest mean RMSE across positions (8.7° , $\sigma = 3.8$), and superior-inferior translations the smallest (1.1° , $\sigma = 0.7$).	61
2.7	(panel a) Magnitude nRMSE (%) and (panel b) phase RMSE (deg) of motion-robust pulses (MRPs) vs reference pulses over all evaluated positions, for all slices. Green and blue regions show positions improved by the MRP and marker size represents the extent of the displacement, either 1, 2 or 5 mm/deg. Considering all slices, the MRPs improved magnitude nRMSE in 251/318 (79%) positions, by an average of 3.6% ($\sigma = 3.3$), and improved phase RMSE in 225/312 (72%) evaluations by an average of 1.4° ($\sigma = 1.6$).	62

2.8	Magnitude/phase excitations for the centre, and the positions most improved by the MRPs, with absolute difference profiles between the two designs, for each slice. Roll and pitch rotations were consistently the most improved motion-type (when considering both magnitude and phase), and the MRPs were able to remove almost all high intensity error regions. Where motion error is shown as zero, this is where the pulses achieved the target flip angle (magnitude), or achieved consistent phase with the centred position.	66
2.9	(panel a) Magnitude nRMSE and (panel b) phase RMSE evaluations of 5-spoke motion-robust pulses (MRPs) vs 3-spoke MRPs over all evaluated positions, for all slices. Green and blue regions show positions improved by the 5-spoke MRPs and marker size represents the extent of the displacement, either 1, 2 or 5 mm/deg. Considering all slices, the 5-spoke MRPs improved magnitude nRMSE in 316/318 (99%) of positions, reducing mean nRMSE, averaged across positions, from 8.4% ($\sigma = 2.8$) to 5.4% ($\sigma = 2.0$). Phase RMSE was improved in 145/312 (46%) of evaluations, reducing mean RMSE from 4.4° ($\sigma = 3.4$) to 3.9° ($\sigma = 3.1$). The remaining 167/312 (54%) of phase evaluations performed similarly to the 3-spoke MRPs	67

2.10	(panel a) Magnitude nRMSE and (panel b) phase RMSE evaluations of 5 and 3-spoke reference pulses over all evaluated positions, for all slices. Green and blue regions show positions improved by the 5-spoke reference pulses and marker size represents the extent of the displacement, either 1, 2 or 5 mm/deg. Considering all slices, the 5-spoke reference pulses improved magnitude nRMSE in 274/318 (86%) positions, by an average of 3.5% ($\sigma = 2.0$), and improved phase RMSE in 129/312 (41%) evaluations by an average of 0.6° ($\sigma = 0.9$). The remaining 183/312 (59%) of phase evaluations were degraded, with a mean increase in RMSE of 0.8° ($\sigma = 1.1$).	68
2.11	(panel a) Magnitude nRMSE and (panel b) phase RMSE evaluations of 5-spoke motion-robust pulses (MRPs) and 5-spoke reference pulses over all evaluated positions, for all slices. Green and blue regions show positions improved by the 5-spoke MRPs and marker size represents the extent of the displacement, either 1, 2 or 5 mm/deg. Considering all slices, the 5-spoke MRPs improved magnitude nRMSE in 211/318 (66%) positions, by an average of 4.3% ($\sigma = 4.5$), and improved phase RMSE in 217/312 (70%) evaluations by an average of 1.4° ($\sigma = 1.6$).	69
3.1	The RF vs magnitude nRMSE at the centred position for slice-selective reference pulses designed using different Tikhonov regularisation terms ($\beta = 0.1, 10, 50, 100, 200, 500, 1000$), plotted from left to right respectively. The $\beta = 100$ pulse, shown in red, presented a good trade-off between the RF and magnitude nRMSE at the centred position, and was selected as the regularisation term for reference pulse design.	80

3.2	The magnitude and phase excitations at the centred positions for the 3-spoke reference pulse ($\beta = 100$) for slices 1 to 6 (left to right). The magnitude nRMSEs at the centred positions for slices 1 to 6 were 12.5%, 9.2%, 6.5%, 6.4%, 8.6%, and 14.7% respectively.	81
3.3	The magnitude excitations centred and 12 off-centre positions used in pulse design for the 5-spoke MRP, for slices 1 to 6 (bottom to top). The magnitude nRMSEs at the centred positions for slices 1 to 6 were 5.5%, 5.3%, 4.6%, 4.3%, 4.5%, and 4.6% respectively.	82
3.4	The phase excitations centred and 12 off-centre positions used in pulse design for the 5-spoke MRP, for slices 1 to 6 (bottom to top).	83
3.5	Magnitude nRMSE (panel a) and phase RMSE (panel b) across all design positions for all six slice-selective MRPs. For magnitude nRMSE, slices 4 and 6 had the largest range (4.2% - 10.9% and 4.6% - 11.3%, respectively), and slice 5 the least (4.5% - 9.9%). Slice 1 had the largest mean magnitude nRMSE across positions (8.3%, $\sigma = 2.1$), and slice 4 the least (6.4%, $\sigma = 1.8$). For phase RMSE, slice 4 had the largest range ($0.4^\circ - 10.5^\circ$), and slice 1 the least ($1.6^\circ - 8.9^\circ$). Slice 2 had the largest mean phase RMSE across positions (5.0° , $\sigma = 3.1$), and slice 5 the least (3.7° , $\sigma = 2.6$).	84

3.6	Magnitude nRMSE (panel a) and phase RMSE (panel b) for each motion type included in the MRP design, across all six slice-selective MRPs. Pitch, roll and yaw rotations ($^{\circ}$) and left-right (LR), anterior-posterior (AP) and superior-inferior (SI) translations (mm). For magnitude nRMSE, overall, pitch rotations had the largest nRMSE averaged (mean) across positions (10.2%, $\sigma = 0.9$), and the centred positions the smallest (4.8%, $\sigma = 0.4$). For overall phase RMSE, yaw rotations had the largest mean RMSE across positions (6.8° , $\sigma = 3.3$), and superior-inferior translations the smallest (1.1° , $\sigma = 0.6$).	85
3.7	(panel a) Magnitude nRMSE (%) and (panel b) phase RMSE ($^{\circ}$) of motion-robust pulses (MRPs) vs reference pulses over all evaluated positions, for all slices. Green and blue regions show positions improved by the MRPs and marker size represents the extent of the displacement, either 1, 2 or 5 mm/ $^{\circ}$. The MRPs improved 100% and 80% of magnitude and phase evaluations, respectively.	87

3.8	The 53 magnitude nRMSE (a, c) and 52 phase RMSE (b, d) evaluations for the slices most (a, b) and least (c, d) improved by the MRP, respectively. The MRP improved 100% of magnitude evaluations in both cases, by an average of 9.5% ($\sigma = 1.3$) for the most improved slice, and 2.3% ($\sigma = 0.9$) for the least improved slice. For the most improved slice, the MRP improved phase in 41/52 (79%) positions by an average of 2° ($\sigma = 1.9$) and degraded 11/52 (21%) by an average of 0.8° ($\sigma = 0.6$). For the least improved slice, phase was improved in 43/52 (83%) positions by an average of 2.1° ($\sigma = 2.6$) and degraded 9/52 (17%) positions by an average of 0.8° ($\sigma = 1.3$).	88
3.9	The magnitude and phase excitations at the centred positions, most improved off-centre excitations, and difference profiles. For slices 1 to 6, the MRPs reduced ref-pulse magnitude nRMSE from 19.4% to 9.8%, 16.2% to 8.8%, 11.8% to 11.0%, 13.4% to 10.9%, 17.5% to 8.8%, and 19.8% to 8.1% respectively. For phase, the MRPs reduced ref-pulse RMSE from 13.7° to 4.1° , 13.1° to 7.7° , 17.1° to 4.0° , 17.8° to 4.3° , 15.7° to 2.7° , and 12.1° to 4.4° , for slices 1 to 6 respectively. Where motion error is shown as zero, this is where the pulses achieved the target flip angle (magnitude), or achieved consistent phase with the centred position.	90

3.10	The magnitude and phase excitations at the centred positions, least improved off-centre excitations, and difference profiles. For slices 1 to 6, the MRPs reduced ref-pulse magnitude nRMSE from 10.5% to 10.3%, 8.0% to 5.9%, 7.5% to 6.1%, 5.7% to 4.2%, 7.4% to 7.1%, and 12.5% to 10.1% respectively. For phase, the MRPs reduced ref-pulse RMSE in slices 3, 5, and 6, from 1.9° to 1.7°, 1.0° to 0.9°, 3.1° to 1.9°, respectively. Phase RMSE was degraded in slices 1, 2, and 4, from 1.4° to 1.6°, 0.8° to 0.9°, and 1.4° to 1.6°, for slices 1 to 6 respectively.	91
3.11	(panel a) The central $\text{SAR}_{10\text{g-avg}}$ and maximum off-centre $\text{SAR}_{10\text{g-avg}}$ for all slice specific MRPs and reference pulses (Ref-Ps). (panel b) A violin plot of the relative $\text{SAR}_{10\text{g-avg}}$ between off-centre positions and the centre. The MRPs reduced central and maximum $\text{SAR}_{10\text{g-avg}}$ in 3/6 slices by an average of 4.9 W/kg ($\sigma = 4.2$) and 6.0 W/kg ($\sigma = 5.5$) respectively. The MRPs increased central and maximum $\text{SAR}_{10\text{g-avg}}$ in 3/6 slices by an average of 2.1 W/kg ($\sigma = 0.2$) and 2.7 W/kg ($\sigma = 0.1$) respectively.	92
3.12	The magnitude and phase evaluations of the gradient updated Ref-Ps (GU-Ref-Ps) vs the Ref-Ps (a, b), the MRPs vs the GU-Ref-Ps (c, d), and the GU-MRPs vs the GU-Ref-Ps (e, f), over all positions for all slices (318 magnitude, 312 phase).	94

- 4.1 (panel a) The 6 slice locations and (panel b, panel c) 23 head positions of predicted and ground-truth B_1^+ -maps of the “Billie” body model provided by Plumley *et al.* for MRP design and evaluation. Positions included on and off-axis translations in the right and posterior directions, and three yaw rotations. Three sets of six slice-selective MRPs were designed by optimising pTx channel weightings over different combinations of positions shown in (panel b) and (panel c) for each slice shown in (panel a). . . . 104
- 4.2 Slice-wise magnitude nRMSE (panel a) and phase RMSE (panel b) across all 23 evaluated positions for the six slice-selective reference pulses. Variation in magnitude nRMSE (panel c) and phase RMSE (panel d) is shown for the different motion types (across all slices) including the centre, on-axis posterior translations (P), on-axis right translations (R), 2 mm posterior off-axis (P+2 / R), 5 mm posterior off-axis (P+5 / R), 10 mm posterior off-axis (P+10 / R), and yaw rotations (Yaw). The centred position is not shown in (panel d) because it is the reference for other positions. 110
- 4.3 Slice-wise magnitude nRMSE (panel a) and phase RMSE (panel b) across all 23 evaluated positions for the six slice-selective MRPs included in set 1 (all 23 positions included in design). Variation in magnitude nRMSE (panel c) and phase RMSE (panel d) is shown for the different motion types (across all slices) including the centre, on-axis posterior translations (P), on-axis right translations (R), 2 mm posterior off-axis (P+2 / R), 5 mm posterior off-axis (P+5 / R), 10 mm posterior off-axis (P+10 / R), and yaw rotations (Yaw). The centred position is not shown in (panel d) because it is the reference for other positions. 112

4.4	(panel a) Magnitude nRMSE (%) and (panel b) phase RMSE ($^{\circ}$) of MRPs _{set-1} (23 design positions) vs reference pulses (Ref-Ps) including all 23 magnitude and 22 phase evaluations, for each of the six slices. Green and blue regions show positions improved by the MRP and marker size represents the extent of the displacement, up to 20 mm right, 10 mm posterior, 15 $^{\circ}$ rotation and 20 mm right 10 mm posterior off-axis	114
4.5	The magnitude and phase excitations at the centred positions, most improved off-centre excitations, and difference profiles. For slices 1 to 6, MRPs _{set-1} reduced ref-pulse magnitude nRMSE from 48.0% to 12.0%, 19.4% to 18.6%, 39.8% to 14.0%, 50.0% to 13.3%, 48.4% to 13.3%, and 43.6% to 13.0% respectively. For phase, the MRPs reduced ref-pulse RMSE from 70.8 $^{\circ}$ to 16.3 $^{\circ}$, 35.2 $^{\circ}$ to 18.2 $^{\circ}$, 44.6 $^{\circ}$ to 15.5 $^{\circ}$, 71.7 $^{\circ}$ to 12.6 $^{\circ}$, 68.8 $^{\circ}$ to 13.0 $^{\circ}$, and 47.3 $^{\circ}$ to 13.3 $^{\circ}$, for slices 1 to 6 respectively. The +15 $^{\circ}$ yaw rotation was the most improved position for all slices. Where motion error is shown as zero, this is where the pulses achieved the target flip angle (magnitude), or achieved consistent phase with the centred position.	117

4.6	Slice-wise magnitude nRMSE (panel a) and phase RMSE (panel b) across all 23 evaluated positions for the six slice-selective MRPs in set 2 (18 design positions). Variation in magnitude nRMSE (panel c) and phase RMSE (panel d) is shown for the different motion types (across all slices) including the centre, on-axis posterior translations (P), on-axis right translations (R), 2 mm posterior off-axis (P+2 / R), 5 mm posterior off-axis (P+5 / R), 10 mm posterior off-axis (P+10 / R), and yaw rotations (Yaw). The centred position is not shown in (panel d) because it is the reference for other positions.	120
4.7	(panel a) Magnitude nRMSE (%) and (panel b) phase RMSE (°) of MRPs _{set-2} (18 design positions) vs reference pulses (Ref-Ps) including all 23 magnitude and 22 phase evaluations, for each of the six slices. Green and blue regions show positions improved by the MRP and marker size represents the extent of the displacement, up to 20 mm right, 10 mm posterior, 15° rotation and 20 mm right 10 mm posterior off-axis	121

4.8	The magnitude and phase excitations at the centred positions, most improved off-centre excitations, and absolute difference profiles. For slices 1 to 6, MRPs _{set-2} reduced ref-pulse magnitude nRMSE from 48.0% to 14.2%, 39.8% to 19.2%, 50.0% to 18.0%, 48.4% to 18.3%, 43.6% to 11.7% for slices 1 and 3 to 6 respectively. Slice 2 reported an increase in magnitude nRMSE from 19.4% to 25.4%. For phase, the MRPs reduced ref-pulse RMSE from 70.8° to 17.7°, 35.2° to 15.5°, 44.6° to 13.5°, 71.7° to 13.7°, 68.8° to 24.2° and 47.3° to 19.6° for slices 1 to 6 respectively. The +15° yaw rotation was the most improved position for all slices, despite not being included in the MRPs _{set-2} design. Where motion error is shown as zero, this is where the pulses achieved the target flip angle (magnitude), or achieved consistent phase with the centred position.	124
4.9	Slice-wise magnitude nRMSE (panel a) and phase RMSE (panel b) across all 23 evaluated positions for the six slice-selective MRPs in set 3 (10 design positions). Variation in magnitude nRMSE (panel c) and phase RMSE (panel d) is shown for the different motion types (across all slices) including the centre, on-axis posterior translations (P), on-axis right translations (R), 2 mm posterior off-axis (P+2 / R), 5 mm posterior off-axis (P+5 / R), 10 mm posterior off-axis (P+10 / R), and yaw rotations (Yaw). The centred position is not shown in (panel d) because it is the reference for other positions.	126

4.10	(panel a) Magnitude nRMSE (%) and (panel b) phase RMSE ($^{\circ}$) of MRPs _{set-3} (10 design positions) vs reference pulses (Ref-Ps) including all 23 magnitude and 22 phase evaluations, for each of the six slices. Green and blue regions show positions improved by the MRP and marker size represents the extent of the displacement, up to 20 mm right, 10 mm posterior, 15 $^{\circ}$ rotation and 20 mm right 10 mm posterior off-axis	128
4.11	The magnitude and phase excitations at the centred and off-centre positions, most improved off-centre excitations, and absolute difference profiles. For slices 1 to 6, MRPs _{set-2} reduced ref-pulse magnitude nRMSE from 48.0% to 30.0%, 38.1% to 20.2%, 50.0% to 13.9%, 48.4% to 24.5%, 43.6% to 22.0% for slices 1 and 3 to 6 respectively. Slice 2 reported an increase in magnitude nRMSE from 19.4% to 30.1%. For phase, the MRPs reduced ref-pulse RMSE from 70.8 $^{\circ}$ to 21.3 $^{\circ}$, 35.2 $^{\circ}$ to 18.6 $^{\circ}$, 32.1 $^{\circ}$ to 12.4 $^{\circ}$, 71.7 $^{\circ}$ to 17.7 $^{\circ}$, 68.8 $^{\circ}$ to 29.8 $^{\circ}$ and 47.3 $^{\circ}$ to 20.5 $^{\circ}$ for slices 1 to 6 respectively. The +15 $^{\circ}$ and +10 $^{\circ}$ yaw rotations were the most improved positions, despite not being included in the MPRs _{set-3} design. Where motion error is shown as zero, this is where the pulses achieved the target flip angle (magnitude), or achieved consistent phase with the centred position.	131

4.12	The central $\text{SAR}_{10\text{g-avg}}$ (at the centred position), maximum off-centre $\text{SAR}_{10\text{g-avg}}$, and distribution of off-centre $\text{SAR}_{10\text{g-avg}}$ relative to the central $\text{SAR}_{10\text{g-avg}}$, for $\text{MRP}_{\text{set-1}}$ (panel a), $\text{MRP}_{\text{set-2}}$ (panel b), $\text{MRP}_{\text{set-3}}$ (panel c), and the six slice-selective reference pulses. The maximum central $\text{SAR}_{10\text{g-avg}}$ (across all MRP sets) was 4.8 W/kg for reference pulses, and 9.5 W/kg for MRPs, both occurring at the superior-most slice (slice 6). For maximum $\text{SAR}_{10\text{g-avg}}$, the maximum value for reference pulses was 5.6 W/kg for the inferior-most slice (slice 1), and 9.5 W/kg for MRPs in the superior-most slice.	134
5.1	The centred and off-centre positions magnitude nRMSE evaluations (panel a) and off-centre phase RMSE evaluations (panel b) for the MRPs against the ref-pulses, across all slices. The MRPs improved 47/50 (94%) of magnitude evaluations with a mean reduction in nRMSE of 4.8% ($\sigma = 2.3$). The three degraded evaluations were the centred positions for slices 1, 4, and 5 with increases in nRMSE of 1.8%, 1.0%, and 0.7% respectively. The MRPs improved all 45 off-centre phase evaluations, with a mean reduction in RMSE of 4.5° ($\sigma = 1.5$).	146
5.2	Slice-wise variation in magnitude nRMSE (panel a) and phase RMSE (panel b) across all 10 positions (9 for phase, centre omitted) for the five slice-selective reference pulses. Position-wise variation in magnitude nRMSE (panel c) and phase RMSE (panel d) across all slices is also shown. The motion parameters associated with each off-centre position are shown in Table 5.1. Position 1 is the centred position.	149

5.3	Slice-wise variation in magnitude nRMSE (panel a) and phase RMSE (panel b) across all 10 positions (9 for phase, centre omitted) for the five slice-selective MRPs. Position-wise variation in magnitude nRMSE (panel c) and phase RMSE (panel d) across all slices is also shown. The motion parameters associated with each off-centre position are shown in Table 5.1. Position 1 is the centred position.	151
5.4	Centred and off-centre positions magnitude and phase excitations for the positions most improved by the MRPs for each slice, with profiles of the absolute difference between off-centre and centred positions excitations. For slices 1 to 5, the MRPs reduce magnitude nRMSE from 18.9% to 7.1%, 11.0% to 7.3%, 12.3% to 5.6%, 18.5% to 9.8%, and 27.7% to 17.0%, respectively. The MRPs reduce phase RMSE from 9.7° to 6.0°, 10.6° to 5.3°, 8.0° to 5.1°, 18.2° to 9.1°, and from 12.9° to 8.7° for slices 1 to 5 respectively. Where motion error is shown as zero, this is where the pulses achieved the target flip angle (magnitude), or achieved consistent phase with the centred position.	152

5.5	Centred position magnitude (magn) excitations and error profiles for each slice-selective reference pulse and MRP for the positions least improved by the MRPs. For each slice, the least improved position was the centred position excitation. Only the magnitude profiles are shown as there is no target phase for the centre. The error profiles are the absolute difference between the centred position excitation and a homogeneous profile of the target flip-angle (60°). For slices 2 and 3, the MRPs reduced magnitude nRMSE from 8.6% to 7.4% and 9.2% to 8.5% respectively. For slices 1, 4, and 5, the MRPs increased magnitude nRMSE by a mean of 1.2% ($\sigma = 0.4$).	154
-----	---	-----

Chapter 1

Introduction

Magnetic resonance imaging (MRI) is a popular technique for non-invasive intra-body imaging, and commonly used in clinical and research settings. Structural MRI has allowed the identification and diagnosis of pathology, while functional MRI (fMRI) can measure changes in blood flow and oxygenation, proving particularly useful in identifying brain region activation in neuroimaging. To produce a practical image for research or clinical purpose, careful consideration of MR physics principles are required in order to achieve the desired image, of sufficient quality, and ensuring patient safety. The design of specialised radiofrequency (RF) “pulse” sequences, applied during MRI, is an integral part of producing a practical image and is a widely studied topic within the MRI community. It is also well documented that within-scan patient motion can greatly affect the quality of an MR image, often resulting in repeated scanning, which is costly and time consuming. Post-processing motion correction techniques for lower field ($< 7\text{T}$) MRI have been developed to retrospectively reduce the effects of patient motion during scanning. While ultra-high field strengths ($> 7\text{T}$) allow higher resolution imaging, it is accompanied by higher levels of RF-field inhomogeneity.

geneity, as the operational wavelength becomes comparable to body dimensions. The distribution of RF-field inhomogeneity is affected by patient motion, which consequently affects image contrast. Therefore, retrospective motion correction is no longer suitable, and prospective methods are required. These techniques either update RF pulses in real time, or account for motion before it occurs (such as the RF pulses designed in this thesis). Parallel transmission excitation (pTx) coils use independently powered channels to apply RF pulses simultaneously, which can improve RF-field homogeneity. This thesis focuses on the design of specialist RF excitation pulses that are able to mitigate the effects of within-scan patient motion in parallel transmit coils, for ultra-high field neuroimaging. Initial proof of concept experiments are performed in-silico that show motion-robust pulses can maintain high quality excitations across many head positions. The performance of the motion-robust pulses are investigated when designed using off-centre RF transmit fields estimated by a novel deep-learning technique developed by Plumley *et al.* [1]. It is demonstrated that this is a very useful approach to addressing the practical issue of needing many input off-centre RF transmit fields for the motion-robust pulse design. Finally, the motion-robust design is tested in a pseudo in-vivo setting, using in-vivo RF transmit distributions to design pulses, and then evaluate their subsequent excitations, giving clearer insight into how the pulses would perform in a practical setting.

1.1 MR Signal

Atomic and sub-atomic particles possess an intrinsic magnetic moment. In quantum mechanics, this is due to a fundamental particle property called “spin”, which is an intrinsic form of angular momentum. For particles such as protons and electrons, the combination of charge and angular momentum leads to their intrinsic magnetic moments. Spin is fundamentally a quantum mechanical

property, however a more classical view can be used to aid understanding. In classical physics, protons and electrons can be considered as electrically charged spinning spheres. Maxwell's equations describe how a moving electric charge produces a magnetic field, leading to a particle's magnetic moment. A particles intrinsic magnetic moment (μ) can be expressed as,

$$\mu = \gamma \mathbf{J} \quad (1.1)$$

where γ is the gyromagnetic ratio, a particle-specific constant considering size, mass and spin. \mathbf{J} is the particle's spin angular momentum, the direction of which also dictates the direction of μ .

The net magnetic moment of a system is the vector sum of the particles' intrinsic magnetic moments, and any magnetic moment caused by the motion of electric charge, for example orbital motion of electrons about a nucleus. This net magnetic moment is called the total magnetization (\mathbf{M}). Applying a strong magnetic field (B_0) to a system of magnetic moments aligns them either parallel or anti-parallel to the direction of the B_0 field, and therefore aligns the total magnetization. It also produces a torque on the particle spins, acting perpendicular to both the B_0 -field and the direction of their angular momentum. The resultant circular motion of the particles, perpendicular to the B_0 -field, is called precession. Precession occurs at a specific angular frequency (ω_0), measured in radians/sec, and acts around the direction of the B_0 -field. In the presence of the B_0 -field, the total magnetization precesses about the direction of B_0 is described by the Bloch equation [2],

$$\frac{d\mathbf{M}}{dt} = \gamma \mathbf{M} \times \mathbf{B}_0 \quad (1.2)$$

Equation 1.2 can be split into it's x, y, and z components,

$$M_x = M\sin(\theta)\cos(\omega t); \quad M_y = \pm M\sin(\theta)\sin(\omega t); \quad M_z = M\cos(\theta) \quad (1.3)$$

where M is the magnitude of the magnetization, θ is a polar angle, and ω is the circular frequency of the RF/ B_1 field, described later in this section [2]. The precession frequency (f_0) exerted on the nuclei by a magnetic field of strength B_0 , is described by the Larmor relationship,

$$f_0 = \gamma B_0 \quad (1.4)$$

The precession of the magnetization about the B_0 -field includes a transverse component. This transverse portion of the net magnetization can induce an electric current in receive coils due to Faraday's law. The current induced in the receive coil by the time-varying transverse magnetization, is called the receive signal. As the magnetization precesses, the current oscillates at the same frequency (the Larmor frequency). The receive signal is then demodulated by removing the carrier signal to produce the MR signal. To produce a more effective receive signal, a secondary magnetic field (B_1) can be briefly applied perpendicular to B_0 , and oscillating at the resonant frequency of the protons spins in the B_0 -field (the Larmor frequency, f_0). This allows magnetic resonance to occur, and spins can be excited to higher energy quantum states, allowing the net magnetization to be tipped out of alignment with B_0 by a tip/flip angle (α). This increases the precessing magnetization vector in the transverse plane and induces a stronger current in the receive coils. The B_1 -field is applied as single or multiple "RF pulses" (discussed Section 1.2), and can be either linearly or circularly polarized based on coil set up [3]. Linearly oscillating fields are generated when transmission acts along a single axis, and consists of

two counter-rotating circular fields. One field acts in the same direction and frequency as the MR spin system, commonly denoted as B_1^+ , and the other opposite to it (B_1^-). The field acting opposite to the spin system does not affect the spins and is considered wasted RF-power that creates adverse tissue heating through induced electrical currents. However, the B_1 -field can be circularly polarized by adding transmission along a second axis perpendicular to the first, and driven with a 90° sinusoidal phase shift. The counter-rotating B_1^- fields along each axis are now 180° out of phase and destructively interfere, leaving only the useful rotating B_1^+ field. Circularly polarized (quadrature transmission) B_1 -fields are most commonly used as they are more power efficient [3]. For more information on polarization of the B_1 -field the reader is pointed to Ref [3] and the appendix of Ref [4].

The induced MR signal varies in time, and for small tip angles ($\alpha \leq 90^\circ$) can be written as,

$$s(t) = \int m(\mathbf{x}) e^{i\gamma \mathbf{x} \cdot \mathbf{k}(t)} d\mathbf{x} \quad (1.5)$$

where $m(\mathbf{x})$ is the transverse plane excitation pattern produced by the B_1 -field, and $\mathbf{k}(t)$ is the excitation k-space trajectory (discussed in section 1.4). For a single transmit RF coil, the transverse excitation pattern can be described as,

$$m(\mathbf{x}) = i\gamma m_0 s(\mathbf{x}) \int_0^T b(t) e^{i\mathbf{x} \cdot \mathbf{k}(t)} dt \quad (1.6)$$

where m_0 is the equilibrium magnetization magnitude, $s(\mathbf{x})$ is the transmit coil's complex sensitivity pattern across the imaged sample, $b(t)$ is a complex RF pulse of length T (discussed in section 1.2). Once the B_1 -field is switched off, the excited spins relax to lower energy states. There are two types of spin relaxation, T1 (longitudinal, spin-lattice) relaxation, and T2 (transverse, spin-spin) relaxation. T1 relaxation is the process of the net magnetization returning to

its initial maximum value, in alignment with the B_0 -field. T1 is the time taken for z-component of the net magnetization to reach about 63% ($1 - 1/e$) of its maximum value [2]. As T1 relaxation occurs, the energy of the spin system decreases, and radiofrequency waves are emitted. The energy is transferred into nearby tissue, however, the amount of energy is small compared to normal molecular kinetic energies and is largely unnoticeable at body temperatures. T2 relaxation is the decay of the transverse component of the net magnetization, caused by dephasing of the spins. The transverse magnetization follows a simple exponential decay, where T2 is the time required for the transverse magnetization to fall to about 37% ($1/e$) of its initial value. Spin dephasing can be caused by T1 relaxation. The spins energy exchange affects both the transverse and longitudinal components of its angular momentum, causing it to lose phase relations with other spins. This means T2 relaxation always occurs with T1 relaxation, but it can occur independently of T1. Static local fields can affect the precessional frequency of the spin, causing it to dephase from other spins. A dipolar interaction, where a pair of spins simultaneously exchange their longitudinal angular momentum, can also cause loss of T2 coherence with no net T1 effect. Dephasing of the spins in the transverse plane reduces the net magnetization vector, causing the MR signal to decay to zero over time. This is called “free induction decay” (FID). The FID oscillates at the Larmor frequency but is damped by T2* decay, where T2* is the observed/effective T2, which is always less than or equal to the theoretical T2 value due to B_0 inhomogeneities. Due to imperfections in the magnet, the B_0 -field is not always perfectly homogeneous, resulting in spatial variation in spins precession frequencies, and an accrued phase $e^{i\gamma\Delta B_0(\mathbf{x})(t-T)}$ which affects the excitation pattern in Eq. 1.6,

$$m(\mathbf{x}) = i\gamma m_0 s(\mathbf{x}) \int_0^T b(t) e^{i\gamma\Delta B_0(\mathbf{x})(t-T)} e^{i\mathbf{x}\cdot\mathbf{k}(t)} dt \quad (1.7)$$

The rotating frame of reference is commonly used when describing MRI phenomena. By convention, the z -axis points in the direction of the B_0 -field. The x and y -axes are orthogonal that form a plane normal to the B_0 -field. The xy -plane is referred to as the transverse plane. In the rotating frame, the transverse plane rotates about the z -axis (B_0 -field direction) with an angular frequency ω_0 . When the theoretical observation point and the transverse plane both rotate at the Larmor frequency, the spins appear stationary. If the FID is considered in the rotating frame of reference, the MR signal becomes an exponential decay curve.

1.2 RF Excitation Pulses

The purpose of RF excitation pulses are to tip the magnetization vector out of alignment with the direction of the main magnetic field (B_0), by a tip/flip angle, α [5–7]. This results in a transverse component of the magnetization, which leads to the MR signal, as described in Section 1.1. RF excitation pulses are “played” by switching on the RF field modulation envelope $b_1(t)$ for a short time (typically 200 μ s to 5 ms); short enough that T1 and T2 relaxations can typically be ignored whilst the pulse is played [8]. The area under the applied RF field envelop is the resulting flip-angle of the on-resonance spins. The flip-angle produced by an excitation pulse can vary across the imaged sample, resulting in a spatial distribution of transverse magnetization. This is due to inhomogeneities in the B_1 -field caused by rapid decay of RF waves due to tissue conductivity, preventing RF field penetration [9]. Ideally, the distribution of flip-angle within the sample would be completely homogeneous, and zero outside the volume of interest. This is so spin relaxations occur from a common flip-angle across the entire sample. Achieving a completely homogeneous flip-angle distribution would require an excitation pulse of infinite duration, however

approximations can be achieved using SINC shaped RF pulses such as “spokes” pulses (discussed further in Section 1.7).

1.3 Gradients

In MRI, a subset of coils, called gradient coils, are used to create fields that cause a small, predictable distortion in the main magnetic field (B_0). The distortion created by the gradient coils cause the resonance frequency of protons to vary as a function of position, allowing spatial encoding of the MR signal. The x-gradient field is defined as,

$$B_G = G_x x \quad (1.8)$$

where G_x is the x-gradient. Sometimes B_G is also termed $B_{G,z}$ as it is the z-component of the B_0 -field that is distorted. Similarly for y-gradient field,

$$B_G = G_y y \quad (1.9)$$

or a z-gradient field,

$$B_G = G_z z \quad (1.10)$$

when a gradient field is applied, the overall magnetic field becomes,

$$\mathbf{B} = (B_0 + B_G)\mathbf{k} \quad (1.11)$$

where \mathbf{k} is vector notation for the z-axis unit vector. If all three gradients are played simultaneously, i.e. $B_G = G_x x + G_y y + G_z z$, then the overall magnetic field becomes,

$$\mathbf{B} = (B_0 + G_x x + G_y y + G_z z)\mathbf{k} \quad (1.12)$$

In vector notation, the gradient field can be written as,

$$B_G = \mathbf{G} \cdot \mathbf{r} \quad (1.13)$$

where $\mathbf{G} = (G_x, G_y, G_z) = G_x \mathbf{i} + G_y \mathbf{j} + G_z \mathbf{k}$. The direction of \mathbf{G} is the gradient direction of B_G , and \mathbf{r} is the spatial location along the gradient direction ($\mathbf{r} = x\mathbf{i} + y\mathbf{j} + z\mathbf{k}$). The complex exponential nature of the MR signal allows encoding of spatial information in two ways, frequency encoding, and phase encoding. Frequency encoding gradients assign a unique precession frequency (Larmor frequency) to each spin isochromat¹ at a distinct spatial location along the gradient direction. This causes the time-domain MR signal to consist of a range of frequencies, each of which is linearly related to a corresponding spatial location along the gradient direction. Using the Larmor equation ($f = \gamma B$), the resonant frequency ($f(x)$) varies linearly with position (x) along the frequency-encoding axis (when the x-gradient is used as the frequency encoding gradient, without loss of generality),

$$f(x) = \gamma B(x) = \gamma B_0 + \gamma x \cdot G_f = f_0 + f_g(x) \quad (1.14)$$

where f_0 is the Larmor frequency of B_0 , G_f is the frequency-encoding gradient, and $f_g(x)$ is the frequency offset based on position along the gradient. Frequency encoding allows spatial encoding of the MR signal, but only in one dimension. Consider an axial slice image. If a linearly increasing frequency-encoding gradient is applied along the x-axis, all pixels along the y-axis for each x-axis step will be encoded with the same frequency. This means there is no differentiation between positions in the y-axis, and therefore no spatial encoding in this direction. Phase encoding can be used for spatial detection in a second dimension. The purpose of a phase-encoding gradient is to dephase

¹Spin isochromat - a cluster of spins with the same precession frequency

spins along a second axis. After the gradient is applied, each spin isochromat in the phase-encoding gradient direction now has a linear spatial variation of magnetization phase. Frequency and phase encoding gradients can be used together to spatially encode a 3D sample.

1.4 k-Space

The concept of k-space is used to simplify the understanding of pulse sequences. It represents the spatial frequency information of a 2D or 3D sample and corresponds to a Fourier conjugate domain to the spatial domain which contains the object magnetization [8, 10]. Neglecting relaxation and diffusion effects, the k-space vector can be defined as,

$$\mathbf{k}(t) = \frac{\gamma}{2\pi} \int_0^t \mathbf{G}(t') dt' \quad (1.15)$$

where $\mathbf{G}(t')$ is the time variation of the gradient waveforms that drive the gradient coils. The space in which $\mathbf{k}(t)$ resides is called k-space, and has units of inverse distance (m^{-1}). This definition of k-space allows the signal $s(t)$ to take the form presented in Eq. 1.5, shown again here for comparison,

$$s(t) = \int m(\mathbf{x}) e^{i\gamma \mathbf{x} \cdot \mathbf{k}(t)} d\mathbf{x} \quad (1.16)$$

This bears a natural resemblance to a complex Fourier transform,

$$\text{FT}[g(x)] = G(k) = \int_{-\infty}^{+\infty} g(x) e^{-2\pi i k x} dx \quad (1.17)$$

where x and k are real variables, $g(x)$ is a function of x , and $G(k)$ is a function of the complex Fourier transform of $g(x)$ [8]. It then follows that by taking the inverse Fourier transform of the signal $s(t)$, the transverse excitation pattern

$m(x)$ can be recovered [8, 11]. The signal $s(t)$ moves through k-space in a path described by the time-dependent k-space vector $\mathbf{k}(t)$. The gradient direction determines the direction of motion through k-space (for positive γ nuclei). The gradient amplitude ($\|\mathbf{G}(t)\|$) and γ determine the speed of k-space traversal ($\|d\mathbf{k}/dt\| = \|\gamma\mathbf{G}\|/(2\pi)$, from Eq. 1.15). The area under the gradient waveform $\mathbf{G}(t)$ is the total distance covered in k-space during that interval. There are many different methods/trajectories for traversing k-space, selected based on case-specific requirements. For more information on k-space trajectories, see Ref [8].

1.5 Ultra-High Field MRI

Ultra-high field MRI (UHF-MRI) is generally regarded as main magnetic field strengths B_0 of $\geq 7\text{T}$. Early work has shown the intrinsic signal to noise ratio (SNR) of MRI is proportional to B_0 [12–14]. The ultimate intrinsic SNR (uSNR) is defined as the maximum possible SNR achievable by any coil positioned outside of the object. Recent work investigated the uSNR in a realistic head model at field strengths varying from 0.5 to 21 Tesla. It was found that the uSNR versus B_0 trend was linear at shallow depths of the model, and superlinear at deeper locations [15]. In-vivo UHF-MRI has also shown higher SNR and contrast-to-noise (CNR) ratios compared to lower B_0 -field strengths, which can be leveraged for improved spatial or temporal resolution [16, 17]. At 7T, spatial resolutions of 200 and 250 μm have been achieved for time-of-flight angiography [18] and whole-brain T1-weighted structural imaging, respectively [19]. However, UHF-MRI suffers from higher levels of radiofrequency field B_1^+ inhomogeneity. This is due to the shorter wavelength of operation, which becomes comparable to body dimensions. This inhomogeneity can lead to artificial signal and contrast variations in the image [3, 9, 20, 21]. Parallel transmission excita-

tion coils can be used to mitigate the increased B_1^+ inhomogeneity at ultra-high field [22–26].

1.6 Parallel Transmission Excitation

The concept of parallel imaging was first proposed to accelerate MR image acquisition [27, 28]. The same concept was then proposed for RF pulse design purposes, using parallel transmission (pTx) coils to allow simultaneous application of non-identical RF pulses through multiple independently powered transmit channels. Katscher *et al.* showed that the superposition of individual channel-specific pulse profiles, weighted by corresponding channel sensitivity profiles, can yield a desired excitation pattern [29]. It was also shown that parallel transmission of the RF allowed for shortening of the traversal path in excitation k-space. Using this technique it is possible to reduce excitation pulse duration without sacrificing spatial definition. Alternatively, pTx could be used to increase the spatial resolution of the excitation profile, while maintaining the transmit RF pulse duration [29]. The experimental implementation of pTx was first shown by Ullmann *et al.* using spatially-selective excitation on up to four transmit channels with acceleration factors of 2 and 2.67 [30]. For spin-echo sequences with a spiral k-space trajectory excitation module, RF pulse lengths were reduced from 14.13 ms (single channel) to 7.065 ms (pTx, acceleration factor = 2) and 5.3 ms (pTx, acceleration factor = 2.67). They observed a significant increase in the qualitative global excitation homogeneity when coil elements were driven with individual RF pulses, pre-calculated using complex coil sensitivity maps (B_1^+ -maps) [30].

Driving individual channels of a pTx coil simultaneously with distinct tailored RF pulses allows for additional degrees of freedom during pulse design. These can be used to shorten pulse lengths, improve the spatial definition of the

excitation pattern, and decrease RF power deposition [31]. Tailored pTx excitation pulse design requires patient specific -field maps that are collected at the start of scanning, which describe the sensitivity of the transmit coils across the imaged volume, $s(\mathbf{x})$. The single transmit channel excitation equation (Eq. 1.6) can be expanded to consider multiple transmit coils by spatially superposing the excitations to form an aggregate pattern,

$$m(\mathbf{x}) = i\gamma m_0 \sum_{r=1}^R s_r(\mathbf{x}) \int_0^T b_r(t) e^{i\mathbf{x} \cdot \mathbf{k}(t)} dt \quad (1.18)$$

where R is the number of transmit coils, each with a unique sensitivity pattern $s_r(\mathbf{x})$ and RF pulse $b_r(t)$. Using this definition of the aggregate excitation pattern, neglecting off-resonance and T1/T2 decay, the MR signal becomes,

$$s(t) = \int \left\{ i\gamma m_0 \sum_{r=1}^R s_r(\mathbf{x}) \int_0^T b_r(t') e^{i\mathbf{x} \cdot \mathbf{k}_t(t')} dt' \right\} e^{i\gamma \mathbf{x} \cdot \mathbf{k}_r(t)} d\mathbf{x} \quad (1.19)$$

where $\mathbf{k}_t(t)$ and $\mathbf{k}_r(t)$ are the transmit and receive k-space trajectories, respectively.

1.7 Slice Selective Excitation and Spokes Pulses

In this thesis, slice selective excitation is of interest. This is achieved by playing a slice selective gradient and a tailored RF pulse simultaneously [7, 32]. The slice selective gradient (G_{ss}) acts along a perpendicular axis to the plane of the desired slice, producing linear variation of potential frequencies in that direction. Each slice, located at position z along G_{ss} , exhibits a unique central frequency,

$$F_c = f_0 + \gamma \cdot z \cdot G_{ss} \quad (1.20)$$

where f_0 is the Larmor frequency in the presence of G_{ss} . A slice of width (Δz) contains some frequencies either side of the central frequency. This frequency range is described as,

$$\Delta F = \gamma \cdot G_{ss} \cdot \Delta z \quad (1.21)$$

The slice thickness can be controlled by adjusting the strength of the slice selective gradient, with stronger gradients producing thinner slices. The RF pulse is designed to match the narrow range of frequencies in the desired slice, resulting in a slice selective excitation. Sinc pulses (amplitude-modulated sine waves) can be used to achieve this frequency profile.

A commonly used type of tailored pTx excitation pulse for mitigating inhomogeneity effects in slice selective excitation is multi-spoke excitation pulses [33–35]. This work focuses on designing spokes pulses, also known as “fast- k_z ” pulses. Spokes pulses use conventional sinc-like RF pulses during each k_z traversal to achieve slice selection. In-plane flip-angle inhomogeneity can be mitigated by modulating the RF waveform of each spoke through suitable design of the complex-valued amplitude. For a single excitation channel, numerous spokes are typically required to homogenise a B_1 field that varies rapidly with position. This leads to impractical RF pulse duration. However applying spokes pulses using multiple excitation channels (pTx, Section 1.6), allows the k -space trajectory to be undersampled. This greatly accelerates the RF pulse and reduces its duration. Spokes/fast- k_z pulses were first proposed by Saekho *et al.* [33]. When compared to a stack of spirals approach, the 5-spoke pulses were able to eliminate sidelobes along the slice-select direction, and excite thin slices (1-5 mm) with short pulse lengths (4-5 ms) [33].

Some of the literature around spokes pulses is discussed to give the reader a general background in spokes pulse development, and a quantitative under-

standing on possible excitation qualities. For low-FA approximations, the combination of spokes pulses and pTx systems have demonstrated highly uniform slice-selective excitations with practical pulse durations [30, 36, 37]. A study by Setsompop *et al.* investigated a magnitude least squares (MLS) optimization of the target magnetization profile for pTx excitation to improve magnitude profile homogeneity and reduce the RF power [38]. This was done by relaxing the uniformity of the distribution of spin phases (phase relaxation) throughout the sample. A four-spoke pulse, with a pulse length of 2.86 ms, excited a magnitude profile within a doped water phantom, of which 96.4% of the data deviated by less than 10% from the flat target profile, and 100% of the data deviated by less than 20% [38]. The performance of spokes-based pulse design has also been demonstrated in-vivo on six human subjects, using a 16-element pTx coil (eight transmit, sixteen receive) at ultra-high field (7T). Spokes-based excitation was combined with MLS optimization, k-space trajectory optimization, and B_0 -field incorporation, to design 2-spoke pulses. These were compared to standard birdcage and RF shimming (equivalent to a one-spoke pulse) excitations. The 2-spoke pulses showed to produce much more homogeneous flip-angle excitations than the other excitation methods. The standard deviation of the magnitude profiles (averaged over all six subjects) was $7.6\% \pm 1.0$ for the two-spoke pulses, $13.3\% \pm 2.3$ for RF shimming, and $16.7\% \pm 3.2$ for birdcage excitations. The percentage of pixels that lay within 10% and 20% of the target excitation profile was reported for each excitation type, demonstrating the quality of the excitation. The 2-spoke pulses far outperformed the other two excitation types, with $85.2\% \pm 5.3$ of pixels within 10% of the target profile and $97.9\% \pm 1.2$ within 20%. For RF shimming, $55\% \pm 8.9$ lay within 10% and $88.9\% \pm 3.2$ within 20%. The birdcage excitations were the lowest quality, with $46.4\% \pm 6.0$ within 10% of the target profile, and $76.7\% \pm 8.1$ within 20%. It was demonstrated that highly

homogeneous slice-selective excitations could be achieved using spokes pulses in a pTx coil at 7T. The trade off for the superior excitation quality was a minor increase in pulse lengths, 2.29 ms for the 2-spoke pulses compared to 1.37 ms for birdcage and RF shimming. As spokes-based excitation has been previously demonstrated to provide high excitation quality for slice-selective excitations, they were chosen as the excitation type to investigate motion-robust pulses in this work.

1.8 Specific Absorption Rate

The B_1 -field produced by the RF transmit coil also induces an electric field within the head tissue due to Faraday’s law, which leads to tissue heating [39]. To ensure patient safety during MRI, guidelines are issued by regulatory bodies such as the International Electrotechnical Commission (IEC), stating that the localized temperature in the head should never exceed 39°C (IEC 601:2-33, 2011). However, local temperature is difficult to assess, and so specific absorption rate (SAR) thresholds are used to limit temperature increases. The SAR is a measure of the amount of power deposited by an RF field in a certain mass of tissue, measured in W/kg [40, 41]. SAR depends on many factors such as the RF coil, flip angle, pulse duration, and pulse shape. SAR can be calculated as a volume integral of the electric field,

$$SAR = \frac{1}{2\Delta V} \iiint_{\Delta V} \frac{\sigma(\vec{r})}{\rho(\vec{r})} |\vec{E}(\vec{r})|^2 dV \quad (1.22)$$

where ΔV is the tissue volume, σ is the electrical conductivity, ρ is the specific tissue density, and $|\vec{E}(\vec{r})|$ is the magnitude of the electric field [39, 42]. The SAR is then averaged over a six minute time period for the head, or a ten second period for short-term exposure, as detailed in the guidelines set by the IEC (IEC

60601-2-33, 2010).

Without SAR limits, the RF energy absorbed by tissue during exposure to the induced electric field could lead to local thermal damage or whole-body regulatory problems, therefore limits are placed on maximum local SAR in any 1-g or 10-g of tissue throughout the body [43]. Whole-body and whole-head average SAR are also constrained [43]. Characterizing the 3D electromagnetic field distribution through RF simulation is commonly used to produce realistic spatial SAR distributions for use in pulse design [41]. This can be done using realistic human body models [44]. While there are clear benefits to pTx in maintaining B_1 homogeneity, the potential for constructive interference of the electric fields between independently powered channels is a valid concern. Massire *et al.* have found that reaching global SAR limits of 3.2 W/kg can allow local temperature to exceed the IEC guideline of 39°C. However, limiting local SAR successfully ensured local temperature inside the head never exceeded 39°C [40]. Other studies found that local SAR limits are exceeded before global SAR, leading the community to investigate variation in local temperature and local SAR further [45, 46]. For pTx, the local interactions of individual coil element fields can be spatially averaged globally or locally over 1-g or 10-g of tissue [41]. The aggregate distribution can be expressed in matrix notation, called Q-matrices, and used to calculate local and global SAR [47, 48]. Eigenvalue-based SAR is an upper-bound of the local SAR and can be used as a safety metric, however it is often overly conservative. It is calculated by taking the maximum eigenvalue of the Q-matrix. RF power can be limited by using conservative local temperature and local SAR estimates during pulse design, however overly conservative SAR limits can significantly limit imaging performance. This makes SAR a complex consideration during pulse design. [31, 49, 50].

1.9 Effects of Patient Motion

Patient head motion can sometimes be unavoidable during MRI. Certain cohorts are especially effected, such as paediatric, Parkinson’s, dementia and Tourette’s syndrome cohorts [51–57]. While there are many benefits to imaging with higher field strengths (see section 1.5), it is at the cost of increased scan durations. Patients are required to remain still for longer periods of time, which is especially difficult in the aforementioned cohorts. The acquisition times for many imaging protocols at UHF can exceed 20 minutes [58].

Within-scan patient motion changes B_1^+ -maps, and therefore, can rapidly deteriorate flip-angle homogeneity of pTx pulses [59, 60]. Because the B_1^+ -field can only be measured in patient tissue, patient motion leads to areas of uncertainty, especially in regions where it could not be measured (i.e., outside the tissue in the original position). Furthermore, the variation in coil-tissue distance and the coil loading lead to further variations in the B_1 -field. The variation in B_1^+ -maps may render previously designed pulses sub-optimal, and may cause flip-angle inconsistencies when motion occurs mid-acquisition. This results in degraded excitation fidelity and imaging artefacts such as blurring or aliasing [61, 62]. Kopanoglu *et al.* showed that head motion can greatly increase SAR metrics, raising potential patient safety concerns. Realistic body models were simulated in all six degrees of motion up to 20 mm/°. In their respective worst-cases, it was found that motion increased eigenvalue-based local SAR by 42%, whole-head SAR by 60% and 10-g averaged local SAR by 210% [41].

The effects of patient motion during studies are often reported, and examples of motion effects in sedated and/or non-sedated cohorts are discussed here. Studies that do not use sedation have reported large motion errors. In a study consisting of 30 dementia patients, during 20-minute PET ² acquisitions, Chen

²PET - Positron Emission Tomography

et al. reported mean translations of 3.41 ± 2.98 mm and mean rotations of $1.92^\circ \pm 1.66^\circ$. The maximum values for translations and rotations were 12.9 mm and 6.2° , respectively [63]. An Alzheimer’s disease (AD) and Down’s syndrome study by Prasher *et al.* recruited 38 subjects, 19 with AD and 19 non-AD. Of the 38 subjects, 14 showed significant motion-related artefacts, resulting in poor image quality of volumetric scans (8 with AD, 6 non-AD) [56]. A functional connectivity MRI study of a paediatric Tourette’s syndrome cohort by Greene *et al.* removed almost half of its participants (41 of $n = 83$) due to the effects of head motion on resting state function connectivity data [57]. In a study by Malviya *et al.* on sedation of children undergoing MRI and CT scans, 22% of 60 sedated children experienced motion during MRI, and 12% experienced excessive motion resulting in the necessity of another scan [51]. Another study, by Kecskemeti *et al.*, investigated motion in 44 non-sedated children (32 diagnosed with autism spectrum disorder, 12 control). They found that the most common motion types were in the superior-inferior directions, and rotations of the sagittal plane. The largest maximum error occurred during rotations of the sagittal plane (20.3°). There also appeared to be only small differences in the extent of motion between the 32 children diagnosed with autism spectrum disorder and the 12 control participants [64].

While MRI is non-invasive, deep sedation or general anesthesia is frequently required in paediatric imaging in order to achieve quality diagnostic images unaffected by patient motion [52, 54]. While sedation can be used to address motion-related problems, it is invasive and unethical in research purposes. Even when sedated, excessive motion leading to poor image quality can still occur [51]. There are also associated risks, such as inadequate, failed, or over-sedation, and adverse reactions such as hypoxaemia [51]. During the Malviya *et al.* study ($n = 922$), 203 (22%) experienced an adverse event related to sedation [51]. The

outcomes of some applications, such as fMRI, can be affected by patient sedation [65]. Gemma *et al.* found that sedated children exhibited an fMRI cortical activation pattern different to those of non-sedated children of a similar age [65]. Liu *et al.* found that resting state fMRI BOLD signal related data (fractional amplitude low-frequency fluctuations) was reduced in a sedation dose-dependent manner [66]. Patient motion can be addressed through sedation and general anesthesia, however, it is not without its own complications and hindrances. The motion-robust excitations pulses discussed in this thesis could have future potential in providing a non-invasive alternative to sedation when addressing motion-related image quality concerns.

1.10 Current Motion Correction Techniques for pTx

Motion correction techniques are generally split into two categories, prospective and retrospective. Retrospective techniques apply motion correction in post-processing by modifying the MR k-space or image data during the reconstruction (after acquisition), and have shown to correct motion-related artefacts at lower field strengths [67–73]. However, variation in image contrast relates to the RF excitation. Post-processing techniques cannot recover contrast homogeneity, therefore needs to be corrected during a scan. This gives rise to the need for prospective motion correction techniques which perform real-time updating of the image acquisition. At lower fields, prospective motion correction techniques can compensate for motion [74, 75], however they may not be directly applied at UHF with parallel-transmit pulses. The added complexity of pulse-design for parallel transmit increases computation times past what is feasible for prospective motion correction. This requires rapid pulse design [76] and the knowledge

of the B_1^+ -map at the new patient location, which can be estimated using deep learning neural networks [1].

Alternatively, motion effects can be considered during initial pulse design. Schmitter *et al.* successfully mitigated the effect of respiratory motion during cardiac imaging by optimising spokes pTx excitation pulses over multiple respiration states at 7T [77]. B_1^+/B_0 -maps were obtained at three different breath-hold positions. Standard spokes pulses were designed conventionally using one position, and motion-robust pulses were designed using multiple positions. The excitation inhomogeneity for the standard pulses varied from normalised root-mean-squared error (nRMSE) = 8.2% (exhale, design position) to 32.5% (inhale). The motion-robust pulses varied from nRMSE = 9.1% (exhale) to 10.6% (inhale). While the motion-robust pulses slightly degraded excitation homogeneity at the exhale position, the pulses were much more stable than the standard pulses at other positions (not included in the standard pulse design). For the work presented in this thesis, it was postulated if a similar approach could be applied to neuroimaging.

1.11 Thesis Overview

The focus of this thesis is the design of parallel transmission excitation spokes pulses that are robust to within-scan patient head motion. The first research chapter demonstrates in-silico the potential of motion-robust spokes pTx pulses for maintaining homogeneity across many different head positions. This was done using a virtual body model, simulated at many different positions within a generic 8-channel pTx coil. A selection of B_1^+ -maps collected at each position were concatenated and used for motion-robust pulse design. These pulses were compared to standard spokes pulses, designed using only the B_1^+ -map from the centred head position. In the second research chapter, similar motion-robust

excitation pTx pulses were designed but using B_1^+ -maps estimated from the deep learning neural network presented in Ref [1]. Different combinations of input B_1^+ -maps were tested to determine the effect on pulse performance. In the final research chapter, motion-robust pTx pulses were designed and evaluated using in-vivo B_1^+ -maps collected using a pTx system at 7T. This provided insight into the suitability of motion-robust pulses for in-vivo MRI applications.

Chapter 2

Motion-Robust pTx

Excitation Pulse Design:

In-Silico Proof of Concept

2.1 Introduction

Ultra-high field magnetic resonance imaging (UHF-MRI) offers higher signal-to-noise (SNR) and contrast-to-noise (CNR) ratios than lower field strengths, which can be leveraged for improved spatial resolution [16, 17]. However, UHF-MRI suffers from radiofrequency field (B_1^+) inhomogeneity due to the shorter operating wavelength. This inhomogeneity can lead to artificial signal and contrast variations in the image [3, 9, 20, 21]. Parallel transmission (pTx) coils allow simultaneous application of non-identical RF pulses through multiple independently powered transmit channels, reducing excitation pulse duration and increasing global excitation homogeneity [29]. A commonly used type of tai-

lored pTx pulse for mitigating inhomogeneity effects in slice selective excitation is multi-spoke excitation pulses [33–35]. Tailored pTx pulses use patient specific field maps (B_1^+ -maps) that are collected at the start of scanning.

The spatial domain method is commonly used to design pTx pulses [78]. By approaching pulse design as a quadratic optimisation problem in the spatial domain, this allows the use of arbitrary k-space trajectories, such as spokes pulses (see Chapter 1.7) which can provide high excitation quality for slice-selective excitations when paired with pTx systems at ultra-high field [34]. Relaxation of the target phase during pulse design has been shown to improve flip-angle homogeneity and has been used before when designing spokes pulses to produce highly homogeneous excitations [35, 38].

Within-scan patient motion changes electromagnetic fields, and therefore, can rapidly deteriorate flip-angle homogeneity of pTx pulses, and can increase specific absorption rate (SAR), leading to patient safety implications [41, 59, 60]. Because the B_1^+ field can only be measured in patient tissue, patient motion leads to areas of B_1^+ uncertainty, especially in regions where B_1^+ could not be measured (i.e., outside the tissue in the original position). The variation in coil-tissue distance exacerbates the variations in the B_1^+ field and may cause flip-angle inconsistencies when motion occurs mid-acquisition, rendering previously designed pulses sub-optimal. This results in degraded excitation fidelity and imaging artefacts such as blurring or aliasing. While motion-related artefacts can be corrected via post-processing at lower field strengths, deterioration in flip-angle homogeneity necessitates prospective methods. Optical motion trackers have previously been used to determine head orientations in real time with high spatial accuracy [79]. The tracking data acquired can be used to update logical gradient field orientations to match changing head orientations.

Different motion states can be considered during initial pulse design to create

a “motion-robust” excitation. The concept of motion-robust excitation pulses was first proposed by Schmitter *et al.*, to mitigate the effects of respiratory motion during cardiac imaging [77]. This was done by optimising RF excitation pulses over multiple respiration states at the pulse design stage. A similar consideration to Ref [77] can be made when designing RF excitation pulses for neuroimaging, by optimising pulses over multiple head orientations, which is the basis of this work. The aim of this chapter was to investigate the potential of motion-robust excitation pulses in neuroimaging, testing their capability of maintaining highly homogeneous flip-angle profiles, and consistent phase distributions, across multiple head positions/orientations. This in-silico study of motion-robust pulses (MRPs) used simulated B_1^+ -maps of a realistic body model within a generic 8-channel pTx coil, at the centred and 52 off-centre positions, covering all six degrees of freedom of motion (up to 5° rotations, 5 mm on-axis translations, and 5 mm left-right 5 mm anterior-posterior off-axis translations). Three and five-spoke slice-specific excitation pulses were optimised to homogenize the flip-angle over thirteen simulated head positions, and tested fifty-three. These pulses were compared to conventionally designed reference spokes pulses designed using only the centred position slice-specific B_1^+ -map. Comparisons were drawn for the six target slices from cerebellum to crown. MRPs would require no mid-scan interruption for pulse redesign and could minimize flip-angle related motion artefacts from data that would otherwise be degraded by motion.

While not a direct outcome of this work, MRP and reference pulse 10-g averaged local specific absorption rate ($\text{SAR}_{10\text{g-avg}}$) is reported. The variation of $\text{SAR}_{10\text{g-avg}}$ during within-scan patient head motion, has previously been investigated in-silico [41]. $\text{SAR}_{10\text{g-avg}}$ was calculated for 2-,3-,5-spoke pulses at 104 head positions of the “Ella” body model within a generic 8-channel pTx coil, covering all six degrees of freedom of motion. Of the 2-,3-,5-spoke pulses, the

peak spatial value of the 3D $\text{SAR}_{10\text{g-avg}}$ distribution was found to increase by up to 2.6-fold, 3.1-fold, and 2.2-fold, respectively, compared to the $\text{SAR}_{10\text{g-avg}}$ at the centred position. Conservative bounds can be placed on SAR estimates, but this can hinder excitation quality by limiting RF power [31, 49, 50]. SAR has been shown to be an important consideration in practical pulse design, and while the focus of this work is on excitation quality, SAR is not ignored.

2.2 Methods

2.2.1 Phase-Relaxed Motion-Robust Pulses

B_1 Simulations

The B_1^+ -map simulations used in this work were a subset of the data set generated by Ref [41], where the virtual body model “Ella” was simulated in 3D (from crown to shoulders) at 53 different head locations/positions inside a generic 8-channel pTx coil using Sim4Life (Zurich MedTech, Zurich, CH) [41, 44, 80]. The coil model used was built of 8 loops, 40 mm width, 110 mm height, 230 mm inner diameter and 3 mm microstrip width. The 53 simulated positions included:

- Centred case (no motion)
- $\pm 1^\circ, \pm 2^\circ, \pm 5^\circ$ pitch/roll/yaw rotations
- ± 1 mm, ± 2 mm, ± 5 mm left-right or anterior-posterior or superior-inferior on-axis translations
- ± 2 mm, ± 5 mm left-right and anterior-posterior off-axis translations

From the 3D simulations, six axial slices were selected for RF pulse design and evaluation. The body model head orientations and slice locations are shown in

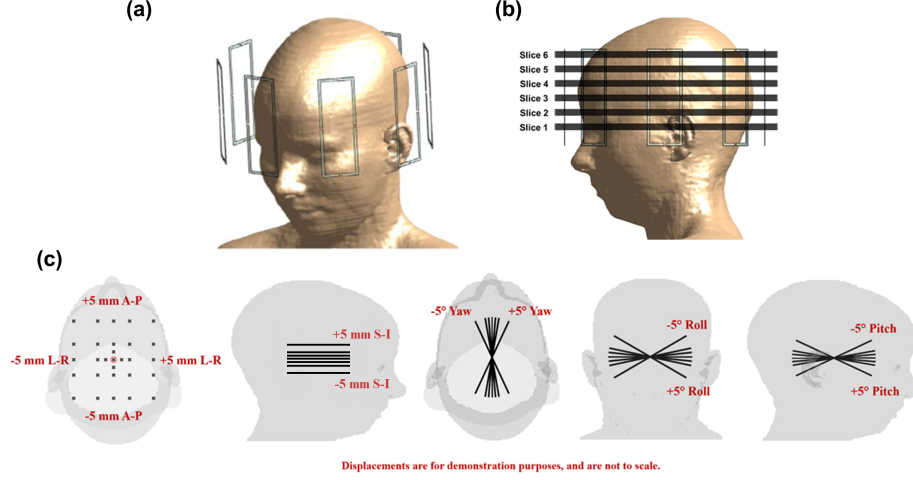


Figure 2.1: The Ella body model inside the generic 8-channel pTx coil designed in Sim4Life (panel a), slice positions (panel b), slice thickness not to scale, and the positions of the centred and 52 off-centre B_1^+ -map simulations (panel c). The displacements shown are for demonstration purposes, and are not to scale.

Figure 2.1. To avoid different voxelization across body model positions, the pTx coil was displaced relative to the head at the centred position and the voxelisation grid. However, displacing the coil can also alter its properties. Therefore, as discussed in Ref [41], automatic high-resolution adaptive voxelization with 1 mm maximum voxel size was used for the coil elements, to minimise these alterations. The loop elements forming the generic head coil were tuned to the simulation frequency of 295 MHz. To override imperfections in coil matching and positional dependencies, simulations were normalized to an accepted power (input power to the coil minus the reflected power at the port) of 1 W per channel beyond the feed port-coil interface, similar to Refs [1, 41, 81]. Coil loading and coupling, including motion-related changes to the coil loading and coupling, were inherently incorporated in the results. Coil elements were manually inspected against connectivity and voxelization issues across all positions. The distribution of the electromagnetic fields was checked for smoothness of

variation across positions. Simulation results were exported to MATLAB (The MathWorks, Natick, MA, USA) for pulse design. For further details on the B_1^+ -map simulations, the reader is referred to Ref [41]

Pulse Design

In the small-tip angle (STA) regime, the transverse magnetization can be approximated by the Fourier integral of an excitation k-space trajectory, $\mathbf{k}(t) = [k_x(t) \ k_y(t) \ k_z(t)]$, weighted by a complex RF pulse $b_r(t)$ and spatially weighted by the coil's complex transmit sensitivity $s_r(\mathbf{x})$ [78]:

$$m(\mathbf{x}) = \sum_{r=1}^{N_c} s_r(\mathbf{x}) \int_0^T b_r(t) e^{i\mathbf{x} \cdot \mathbf{k}(t)} d\mathbf{x} \quad (2.1)$$

where T is the pulse length, N_c is the number of transmit channels, and r indexes the transmit channels. In this study the main magnetic field B_0 is assumed to be homogeneous and no off-resonance effects were considered. Discretizing in time and space, the aggregate excitation pattern \mathbf{m} can be written as,

$$\mathbf{m} = \begin{bmatrix} S_1 A & \dots & S_r A \end{bmatrix} \begin{bmatrix} b_1 \\ \dots \\ b_{r \times N_{spokes}} \end{bmatrix} = \mathbf{A}_{full} \mathbf{b}_{full} \quad (2.2)$$

where \mathbf{m} , S_r , and b denote $m(\mathbf{x})$, $s_r(\mathbf{x})$ and $b_r(t)$ respectively, after discretization. A is the Fourier encoding matrix, and N_{spokes} is the number of spokes of the pulse.

Three and five-spoke reference pulses (ref-pulses) were designed in the STA regime and optimised for the B_1^+ -map from the centred position, as is conventional. RF channel weightings were optimized via matrix inversion and a phase-relaxed magnitude least-squares regression [38, 78],

$$\hat{\mathbf{b}}_{full} = \arg_{\mathbf{b}_{full}} \min\{||\mathbf{A}_{full}\mathbf{b}_{full} - \mathbf{m}_{des}||^2 + R(\mathbf{b}_{full})\} \quad (2.3)$$

where \mathbf{m}_{des} is the desired excitation and $R(\mathbf{b}_{full})$ is a Tikhonov regularisation term used to control channel-by-channel RF power, $R(\mathbf{b}_{full}) = \beta \mathbf{b}'_{full} \mathbf{b}_{full}$, where β is a tuning parameter [82, 83]. The cost function was defined as,

$$\text{cost} = (\mathbf{m}_{ach} - \mathbf{m}_{des})'(\mathbf{m}_{ach} - \mathbf{m}_{des}) + R(\mathbf{b}_{full}) \quad \{\text{cost} \in \mathbb{R} : \text{cost} \geq 0\} \quad (2.4)$$

where $\mathbf{m}_{ach} = \mathbf{A}_{full}\mathbf{b}_{full}$ is the achieved excitation, \mathbf{m}_{des} is the desired excitation, and $(\mathbf{m}_{ach} - \mathbf{m}_{des})'$ denotes the complex conjugate. The excitation phase is updated during each iteration of the optimisation to find the best solution for the magnitude of the flip-angle profile.

A 5×5 uniform $k_x - k_y$ grid of candidate spokes (5 m^{-1} spoke separation in k_x, k_y) was tested to determine spoke placement, choosing the largest l_2 -norm location as each spoke is added, and removing it as an option for subsequent spokes. The DC point ($k_x = k_y = 0$) was always chosen first. Channel weights for previously selected spokes were re-optimized when a new spoke was added. The ref-pulses used only the B_1^+ map at the centred position in their design, as is conventional. Pulse design parameters were: flip-angle, 60° ; slice thickness, 1.5 mm; peak RF amplitude, 30 μT ; dwell time, 4 μs ; time-bandwidth (TBW) product, 4; maximum gradient amplitude, 80 mT/m; maximum gradient slew rate, 200 mT/m/ms. If necessary, the dwell time was increased to satisfy the peak RF amplitude (maximum B_1^+) constraint. This sometimes resulted in varying pulse lengths across slices.

Three and five-spoke motion-robust pulses (MRPs) were designed identically to the reference pulses, except optimising over a concatenation of 13 B_1^+ -maps, each from a different head position/orientation. The positions included in the

design were:

- centred case (no motion)
- $\pm 5^\circ$ pitch/roll/yaw rotations
- ± 5 mm left-right/anterior-posterior/superior-inferior translations

The sensitivity matrix S for the r^{th} channel is,

$$S_r = \begin{bmatrix} s_r^{p_1} \\ \dots \\ s_r^{p_{13}} \end{bmatrix} \quad (2.5)$$

where p_1, \dots, p_{13} denote different positions. The sensitivity matrix was then vectorized and treated as if it were a single slice. Target profiles were concatenated and vectorized similarly. Pulse design was performed in patient co-ordinates by co-registering and concatenating all B_1^+ -maps. Positional differences were incorporated by duplicating and then adapting the gradient fields (i.e., encoding matrices $A^{p_1} \dots A^{p_{13}}$ for each of the 13 design B_1 maps, then concatenating similarly.

Pulse Evaluation

Evaluations of 3-,5-spoke MRPs against 3-,5-spoke ref-pulses were investigated. Magnitude and phase profiles of the flip-angle were extracted from the complex excitation produced in each position. The magnitude profiles were extracted by calculating the absolute value of each element of the complex excitation produced at each position. The phase information was extracted by passing the complex excitation in MATLAB's "angle" function which calculates the argument of each complex element with respect to the positive real axis. For an example element $z = x + yi$, the phase ϕ is,

$$\phi = \text{atan2}(y, x) \quad (2.6)$$

where atan2 is a two-argument variant of the arctangent function.

The two main error metrics used to determine performance of the finalised pulses were normalised root-mean-squared error (nRMSE) of the magnitude of the excitation profiles, and the RMSE of the phase profiles, calculated with respect to target profiles. The error in magnitude and phase distributions were calculated separately. Magnitude difference profiles ($\Delta m_{\text{magnitude}}$) were calculated as the absolute difference between the achieved position-specific magnitude profile ($|m_{\text{achieved}}|$), and a position-specific homogeneous profile of the target flip-angle ($|m_{\text{homogeneous}}|$),

$$\Delta m_{\text{magnitude}} = ||m_{\text{achieved}}| - |m_{\text{homogeneous}}||_{W_m} \quad (2.7)$$

and W_m represents the mask. $\Delta m_{\text{magnitude}}$ was vectorized and used to calculate magnitude nRMSE,

$$\text{nRMSE} = \frac{1}{a_t \sqrt{N_x}} ||\Delta m_{\text{magnitude}}||_2 \times 100 \quad (2.8)$$

where a_t is the target flip angle (60°), N_x is the number of non-zero voxels in the mask, and $|| \cdot ||_2$ represents the l2-norm.

Phase difference profiles (Δm_{phase}) were calculated as the absolute difference between the achieved position-specific complex profile ($m_{\text{off-centre}}$) and the complex profile at the centred position (m_{centre}), as phase must be consistent across positions. The \angle operator calculates the angle of the complex magnetisation, \oslash represents element-wise division,

$$\Delta m_{\text{phase}} = |\angle(m_{\text{off-centre}} \oslash m_{\text{centre}})|_{W_{ph}} \quad (2.9)$$

where W_{ph} represents a reduced mask to remove a peripheral band from the phase profiles. Comparing off-centre phase evaluations to the phase at the centred position caused artificially elevated error values due to partially filled voxels after co-registration of flip-angle distributions across positions. Therefore a 2-voxel thick peripheral band was masked out. Element-wise division between off-centre and centred position complex excitations was used to remove phase-wrapping effects from the profiles. Δ_{phase} was vectorized and used to calculate phase RMSE,

$$\text{RMSE} = \frac{1}{\sqrt{N_x}} \|\Delta m_{phase}\|_2 \quad (2.10)$$

Due to extending the optimisation over multiple patient positions in the MRP design, we had a directional hypothesis that the error over off-centre positions would be lower for MRPs than the reference pulses, which were optimised for the centred position only. Therefore a left-tailed paired t-test with 5% significance level ($p \leq 0.05$) was used to investigate slice-specific MRP performance against the ref-pulses. Other pulse performance metrics investigated included the number of positions improved for each slice and the mean improvement or degradation in magnitude nRMSE/RMSE.

Actual 10-g averaged local SAR ($\text{SAR}_{10\text{g-avg}}$) was calculated for the centre and the 52 off-centre positions for all slice-selective MRPs and reference pulses. $\text{SAR}_{10\text{g-avg}}$ sensitivity to motion was investigated for each pulse design and SAR at the centred position, maximum off-centre SAR and the distribution of $\text{SAR}_{10\text{g-avg}}$ were compared between designs over all slices.

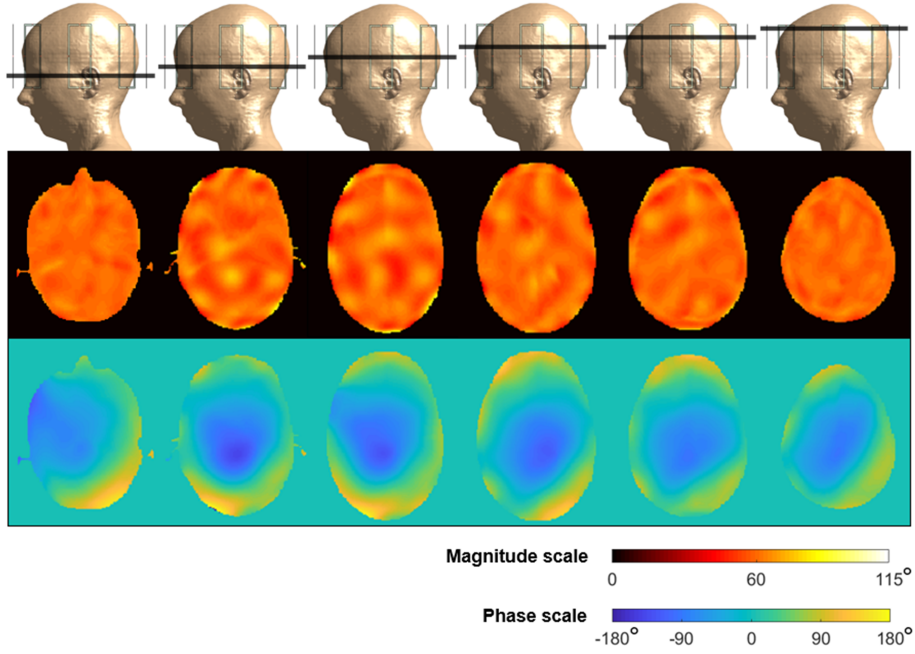


Figure 2.2: Magnitude (top) and phase (bottom) profiles of the flip-angle at the centered position for each of the slice specific 3-spoke reference pulses. Magnitude nRMSEs for slices 1 to 6 (left to right) were 4.2%, 9.1%, 9.6%, 7.6%, 7.0%, 4.5% respectively. There was no associated phase error for the centred positions, as discussed in the text.

2.3 Results

2.3.1 3-spoke MRPs vs 3-spoke Ref-Pulses

Figure 2.2 shows the magnitude and phase profiles for the design positions (centred positions only) of each slice-specific 3-spoke ref-pulse. The magnitude nRMSEs for slices 1 to 6 were 4.2%, 9.1%, 9.6%, 7.6%, 7.0%, 4.5% respectively. There was no associated RMSE with the phase profiles at the centred position, as phase relaxation was used during pulse design to improve magnitude homogeneity at the centred position. Therefore there was no strict target phase profile at the centered position.

The magnitude and phase profiles of the six slice-specific 3-spoke MRPs are

shown in Figures 2.3 and 2.4 respectively. The magnitude nRMSEs for the centred positions of slices 1 to 6 were 9.0%, 8.4%, 7.7%, 6.9%, 3.6%, 5.5% respectively. The phase profile at the centred positions had no associated error, as there was no target phase distribution. Phase relaxation was applied during pulse design to improve flip-angle magnitude homogeneity at the centred position.

Figure 2.5 displays the magnitude nRMSE and phase RMSE respectively across the design positions shown in Figures 2.3 and 2.4, for each slice. Magnitude nRMSE ranged from 3.6% to 22.1% across slices and positions, with the maximum error occurring at the $+5^\circ$ pitch rotation in the inferior-most slice (slice 1). The inferior-most slice (slice 1) also had the largest mean of magnitude nRMSE across positions (12.7%, $\sigma = 3.7$). The smallest mean magnitude nRMSE across positions was 6.3% ($\sigma = 2.0$), reported in the penultimate superior slice (slice 5). The centre was not always the lowest nRMSE position. Three slices reported superior-inferior translations with lower magnitude nRMSEs than their equivalent centred positions. While the MRPs were expected to perform worse in magnitude evaluations at the centred position due to added complexity of designing for multiple motion states, this was not the case for the four middle slices (slices 2 to 5), which reported lower nRMSEs than the ref-pulses.

Although the phase profiles at the centred positions have no associated error, if the phase distributions in off-centre positions are inconsistent with the centred position, this can lead to imaging artefacts. Off-centre phase error was calculated as the RMSE of the absolute difference between the phase profiles at an off-centre position and the equivalent centred position, to quantify phase consistency across positions. Phase RMSE ranged from 0.5° to 17.3° , with the maximum error occurring at the -5° pitch rotation in the superior-most slice

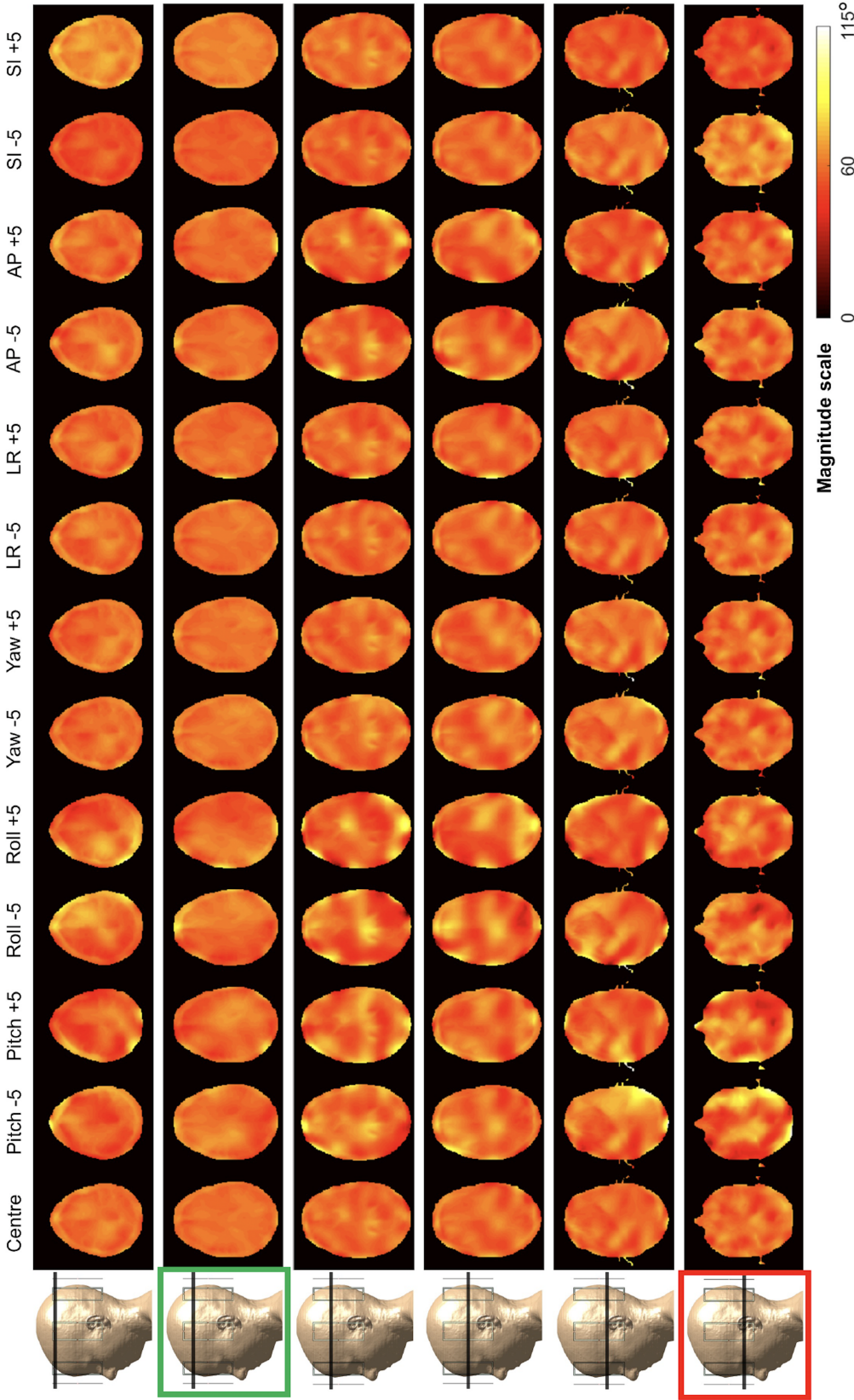


Figure 2-3: Magnitude profiles for all 13 positions used in pulse design for each of the six slice-specific 3-spoke MRPs. The slice with the lowest mean nRMSE (averaged across positions) was slice 5 (indicated in green), and the slice with the largest mean nRMSE is indicated in red. Magnitude nRMSE for the centred positions in slices 1 to 6 were 9.0%, 8.4%, 7.7%, 6.9%, 3.6%, and 5.5%, respectively. Off-centre magnitude nRMSE ranged between, 9.0%-22.1%, 8.1%-17.5%, 7.5%-16.3%, 6.6%-16.9%, 3.6%-10.1%, and 5.5%-14.0%, for slices 1 to 6 respectively.

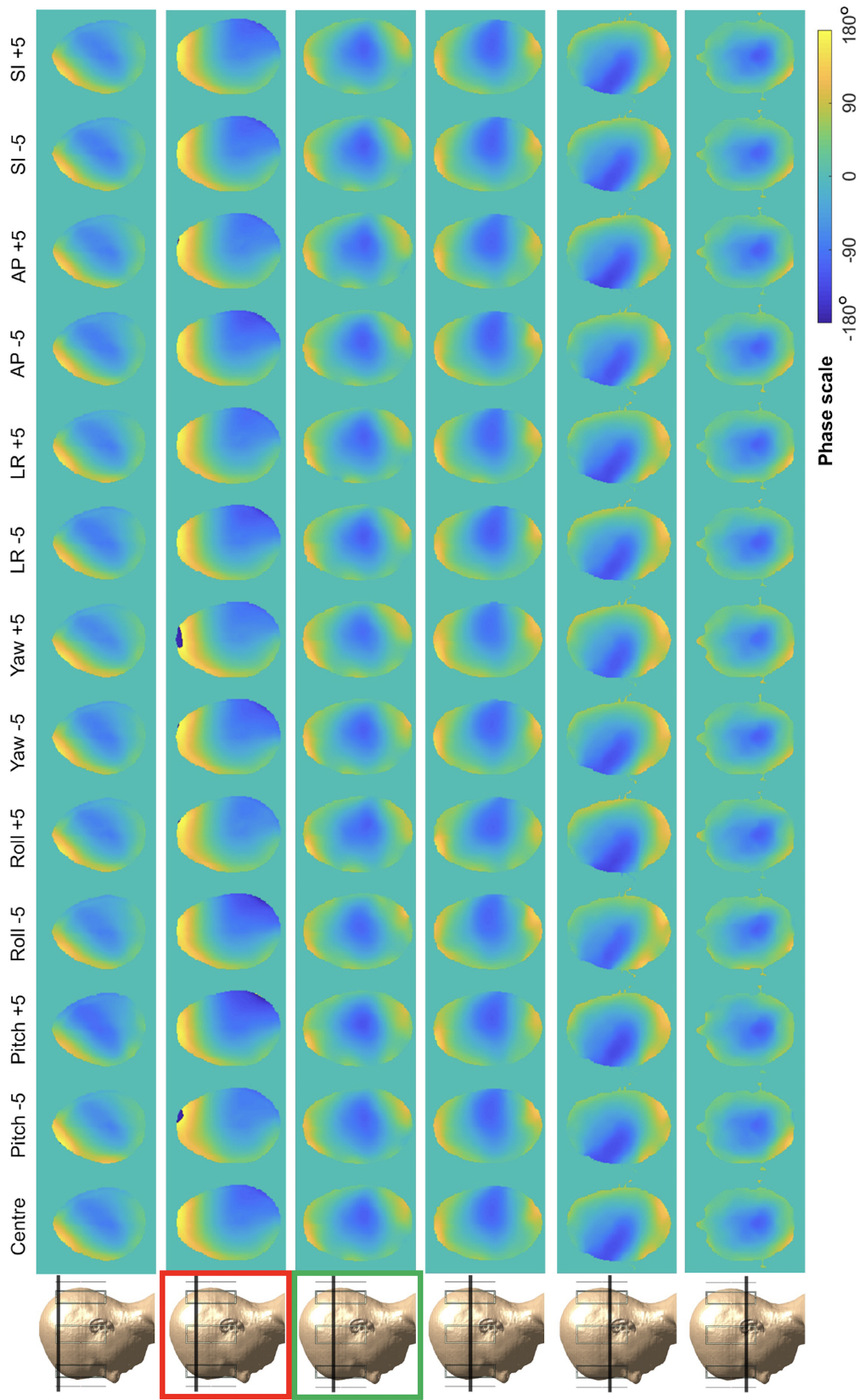


Figure 2.4: Phase profiles for all 13 positions used in pulse design for each of the six slice-specific 3-spoke MRPs. Off-centre phase RMSE, calculated relative to the phase distribution at the centred position, ranged between $1.8^\circ - 10^\circ$, $0.9^\circ - 15.1^\circ$, $0.5^\circ - 12.5^\circ$, $0.6^\circ - 12.2^\circ$, $0.9^\circ - 15.4^\circ$, and $2.3^\circ - 17.3^\circ$, for slices 1 to 6 respectively. The slice with the lowest mean RMSE (averaged across positions) is indicated in green, and the slice with the largest mean RMSE is indicated in red.

(slice 6). The penultimate superior slice (slice 5) reported the largest mean phase RMSE across positions ($5.6^\circ, \sigma = 4.3$).

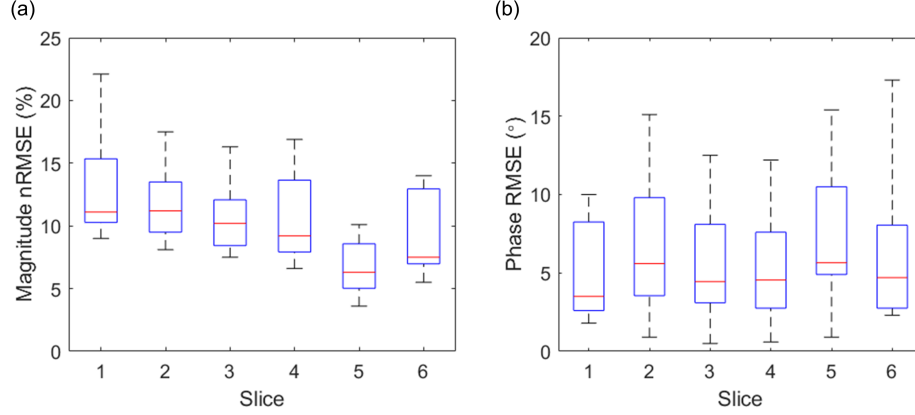


Figure 2.5: Magnitude nRMSE (panel a) and phase RMSE (panel b) across all design positions for all six slice-selective MRPs. For magnitude nRMSE, slice 1 had the largest range (9.0%-22.1%), and slice 5 the least (3.6%-10.1%). Slice 1 had the largest mean magnitude nRMSE across positions (12.7%, $\sigma = 3.7$), and slice 5 the least (6.3%, $\sigma = 2.0$). For phase RMSE, slice 6 had the largest range (2.3°-17.3°), and slice 1 the least (1.8°-10.0°). Slice 5 had the largest mean phase RMSE across positions ($5.6^\circ, \sigma = 4.3$), and slice 4 the least ($3.7^\circ, \sigma = 3.3$).

Considering all six slices, the magnitude nRMSE and phase RMSE variation across the different motion types included as design positions are shown in Figure 2.6 (panel a) and (panel b) respectively. Averaging magnitude nRMSE across slices for each motion type reported roll rotations with the largest mean magnitude nRMSE overall (14.1%, $\sigma = 2.2$), and yaw rotations the least (7.8%, $\sigma = 2.0$). For phase RMSE, pitch rotations had the largest mean error across slices ($8.7^\circ, \sigma = 3.8$), and superior-inferior translations the least ($1.1^\circ, \sigma = 0.7$).

Figure 2.7 compares magnitude nRMSE (panel a) and phase RMSE (panel b), across all 52 off-centre positions for all 6 slices, including the centred positions for magnitude. The green and blue shaded regions show the MRPs improvement over the ref-pulses in magnitude and phase respectively. The MRPs showed

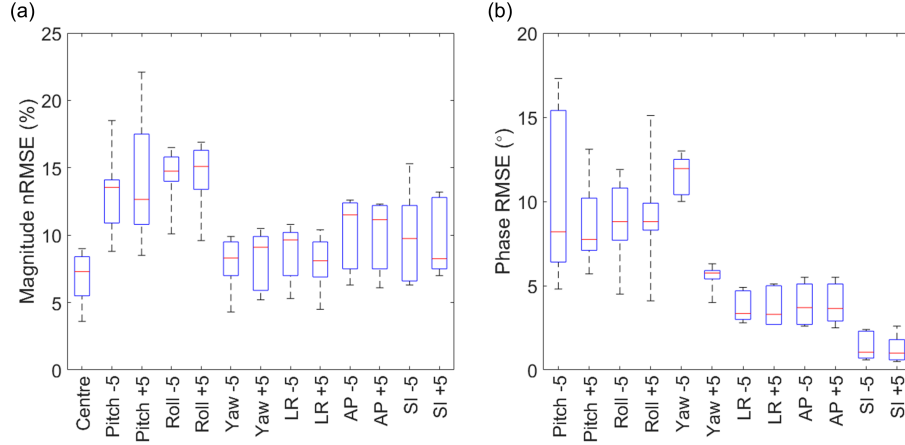


Figure 2.6: Magnitude nRMSE (panel a) and phase RMSE (panel b) for each motion type included in the MRP design, across all slice-selective MRPs. Pitch, roll and yaw rotations ($^{\circ}$) and left-right (LR), anterior-posterior (AP) and superior-inferior (SI) translations (mm). For magnitude nRMSE, overall, roll rotations had the largest nRMSE averaged (mean) across positions (14.1%, $\sigma = 2.2$), and the centred positions the smallest (6.9% $\sigma = 1.8$). For overall phase RMSE, pitch rotations had the largest mean RMSE across positions (8.7°, $\sigma = 3.8$), and superior-inferior translations the smallest (1.1°, $\sigma = 0.7$).

improved magnitude nRMSE in 251/318 positions (79%), by a mean of 3.6% ($\sigma = 3.3$), reducing mean nRMSE from 12.2% ($\sigma = 4.7$) to 8.6% ($\sigma = 2.9$). The mean nRMSE was degraded in the remaining 21% of positions by 3.3% ($\sigma = 1.9$), from 6.6% ($\sigma = 2.3$) to 9.9% ($\sigma = 2.9$).

The MRP improved phase RMSE in 225/312 positions (72%) by a mean of 1.4° ($\sigma = 1.6$) across positions, reducing mean RMSE from 4.9° ($\sigma = 3.5$) to 3.6° ($\sigma = 2.6$). The mean RMSE across the remaining 28% of positions was degraded by 1.0° ($\sigma = 1.2$), from 3.8° ($\sigma = 2.8$) to 4.7° ($\sigma = 3.6$). It can be seen from Figure 2.7 that in general the largest ref-pulse magnitude and phase errors were rotations, particularly pitch and roll in magnitude evaluations and pitch, roll and yaw for phase evaluations.

Table 2.1 shows the number of positions improved or degraded by the MRP for magnitude evaluations, and the mean improvement/degradation in magni-

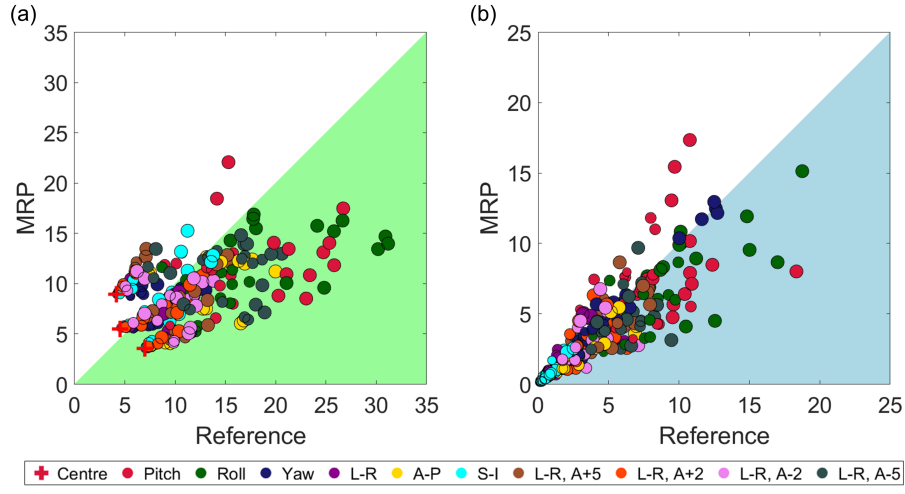


Figure 2.7: (panel a) Magnitude nRMSE (%) and (panel b) phase RMSE (deg) of motion-robust pulses (MRPs) vs reference pulses over all evaluated positions, for all slices. Green and blue regions show positions improved by the MRP and marker size represents the extent of the displacement, either 1, 2 or 5 mm/deg. Considering all slices, the MRPs improved magnitude nRMSE in 251/318 (79%) positions, by an average of 3.6% ($\sigma = 3.3$), and improved phase RMSE in 225/312 (72%) evaluations by an average of 1.4° ($\sigma = 1.6$).

Slice	Magnitude					
	Positions Improved	Positions Degraded	Mean Improvement (%)	σ	Mean Degradation (%)	σ
1	2	51	1.9	0.9	4.1	1.2
2	52	1	3.3	3.2	0.1	0
3	53	0	3.2	2.3	0	0
4	52	1	1.5	1.3	0.04	0
5	53	0	6.1	3.1	0	0
6	39	14	4.1	4.4	0.5	0.3

Table 2.1: The number of magnitude evaluations (positions) improved/degraded by the MRPs and the mean improvement/degradation. The MRPs showed impressive performance for slices 2 to 5, improving all or all but one positions. The MRP performed poorly for slice 1.

tude nRMSE. The MRPs improved all positions, including the centred position in two slices (slices 3 and 5), with the penultimate superior slice (slice 5) seeing the largest mean improvement in nRMSE of 6.1% ($\sigma = 3.1$), averaged across all improved positions. The inferior-most slice (slice 1) was the least improved for magnitude, with 51/53 positions degraded by the MRPs by a mean nRMSE of 4.1% ($\sigma = 4.4$). If the inferior-most slice is removed from consideration, only 6% of magnitude evaluations are degraded, increasing mean nRMSE by 0.5% ($\sigma = 0.3$), from 6.0% ($\sigma = 1.7$) to 6.5% ($\sigma = 1.5$).

Table 2.2 shows the number of positions improved or degraded by the MRP for phase evaluations, and the mean improvement/degradation in phase RMSE. One of the middle slices (slice 4) saw the most positions improved (46/53), and the superior slices (slices 5 and 6) the least (28/53 and 26/53, respectively). The inferior-most slice (slice 1) phase evaluations were not as dramatically affected as magnitude evaluations. The penultimate inferior slice (slice 2) and the middle slices (slices 3 and 4) saw the most benefit from the MRPs, improving 157/159 (99%) of magnitude evaluations, and 134/156 (86%) of phase evaluations.

Figure 2.8 shows the magnitude/phase excitations for the centre, and most improved off-centre position, with absolute difference profiles between the MRPs

Slice	Phase					
	Positions Improved	Positions Degraded	Mean Improvement ($^{\circ}$)	σ	Mean Degradation ($^{\circ}$)	σ
1	37	15	2.0	2.1	1.0	1.0
2	45	7	0.9	1.0	0.2	0.2
3	43	9	1.7	1.6	0.4	0.6
4	46	6	0.8	0.9	0.5	0.3
5	28	24	1.2	1.3	1.3	1.3
6	26	26	1.7	2.1	1.1	1.5

Table 2.2: The number of phase evaluations (positions) improved/degraded by the MRPs and the mean improvement/degradation. The MRPs showed good performance for the inferior and middle slices (slices 1 to 4). The superior slices (slices 5 and 6) saw more positions degraded than the other slices, and mean degradation was similar to mean improvement.

and reference pulses, for each slice. The difference profiles were calculated as in equations 2.7 and 2.9 in Section 2.2.1. The most improved positions were determined by taking the average (mean) of the difference between the MRPs and ref-pulse’s magnitude and phase profiles for each position. The most improved positions for all slices were a pitch or roll rotation, which generally coincided with the reference pulse position with the largest error. For magnitude, the largest improvement was in the superior-most slice (slice 6), reducing magnitude nRMSE from 31% to 14%. In the inferior-most slice (slice 1) magnitude nRMSE was increased by the MRP from 15% to 22%, however, produced the largest phase RMSE improvement, reducing phase RMSE from 18° to 8° . Phase RMSE was improved in all positions shown in Figure 2.8, except for the penultimate superior slice (slice 5), which increased phase RMSE from 10° to 15° . The MRPs demonstrated the ability to reduce high intensity error regions in magnitude profiles. The apparent random nature of the motion error profiles is due to how they are calculated. They are the profiles of the absolute difference between two spatially varying distributions (one at an off-centre position, and one at the centred position), with a similar mean. Where the motion error profiles show zero error is where the magnitude of the flip-angle at that location is

the target flip-angle, or where the phase at the off-centre position was consistent with the phase at the centred position.

RF pulse lengths for the MRPs ranged from 4.0 ms to 6.4 ms, with a mean of 5.0 ms ($\sigma = 0.8$) across all six slices. The RF pulse lengths for the ref-pulses ranged from 4.0 ms to 7.9 ms, with a mean of 5.5 ms ($\sigma = 1.5$). The MRPs had shorter RF pulse lengths than the reference pulses in slices four of the six slices, and longer in the remaining two slices.

Slice-specific left-tailed paired t-tests with a 5% significance level ($p \leq 0.05$), considering all off-centre positions, showed the MRPs statistically improved magnitude nRMSE evaluations in all slices ($p < 0.001$) except the inferior-most slice ($p = 1$). For phase RMSE, MRPs statistically improved evaluations in first four slices ($p < 0.001$). The p-values for MRP phase RMSE evaluations for the two most superior slices (slices 5 and 6) were $p = 0.438$ and $p = 0.194$, respectively.

2.3.2 Adding Additional Spokes

The effect of adding extra spokes to both the reference pulse and MRP design was investigated. Figure 2.9 shows the magnitude nRMSE and phase RMSE of all 52 off-centre positions for all six slices, and magnitude nRMSEs at the centred positions, for 5-spoke and 3-spoke MRPs. Overall the 5-spoke MRPs showed improved magnitude nRMSE at the centred position and motion-robustness, reducing magnitude nRMSE in 316/318 (99%) of positions from 8.4% ($\sigma = 2.8$) to 5.4% ($\sigma = 2.0$). The two degraded evaluations performed similarly to the 3-spoke MRPs. The 5-spoke MRPs improved 145/312 (46%) of phase evaluations, reducing mean RMSE from 4.4° ($\sigma = 3.4$) to 3.9° ($\sigma = 3.1$). The remaining 167/312 (54%) of evaluations performed similarly to the 3-spoke MRPs, increasing mean RMSE from 3.6° ($\sigma = 2.6$) to 4.6° ($\sigma = 3.4$).

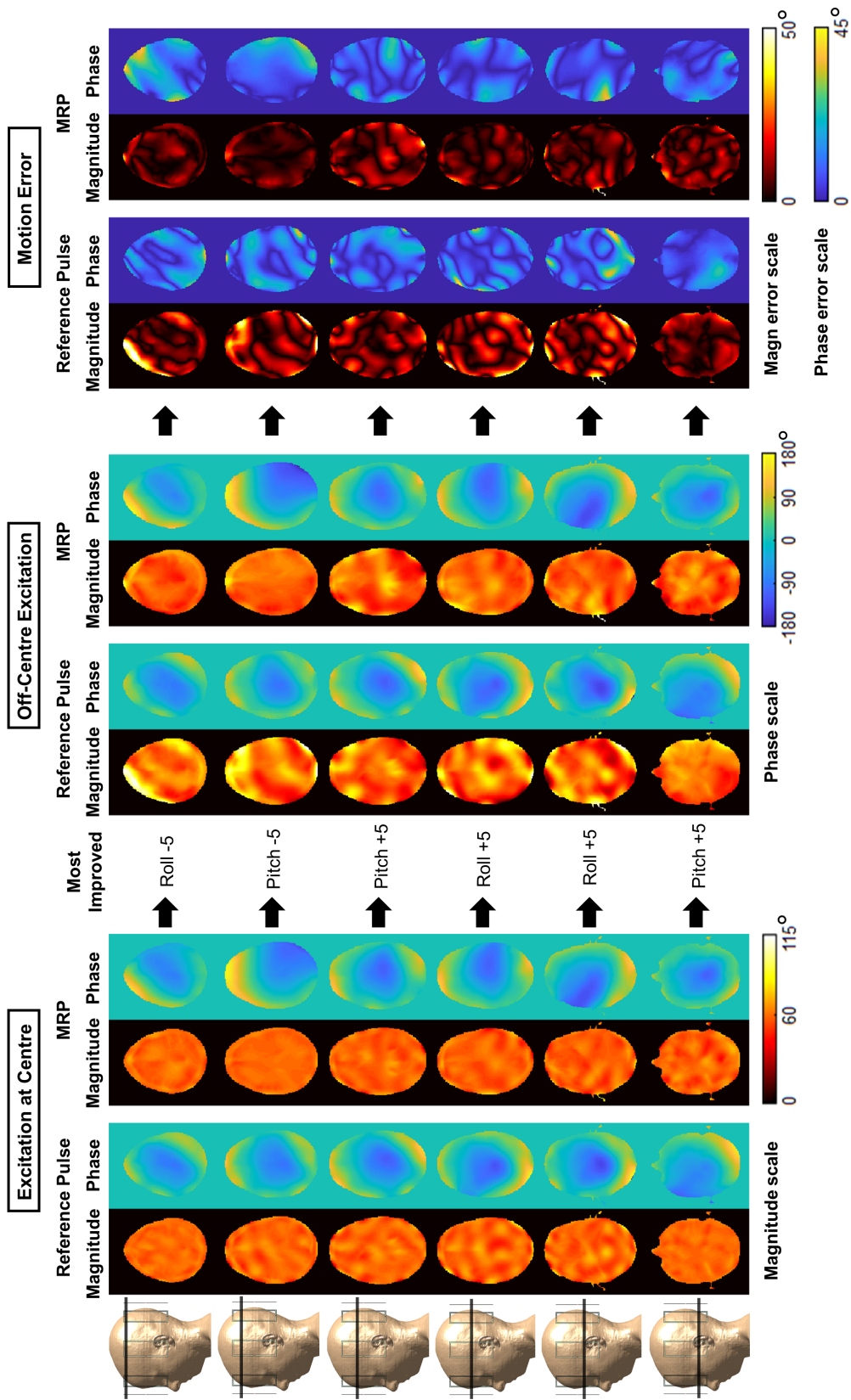


Figure 2.8: Magnitude/phase excitations for the centre, and the positions most improved by the MRPs, with absolute difference profiles between the two designs, for each slice. Roll and pitch rotations were consistently the most improved motion-type (when considering both magnitude and phase), and the MRPs were able to remove almost all high intensity error regions. Where motion error is shown as zero, this is where the pulses achieved the target flip angle (magnitude), or achieved consistent phase with the centred position.

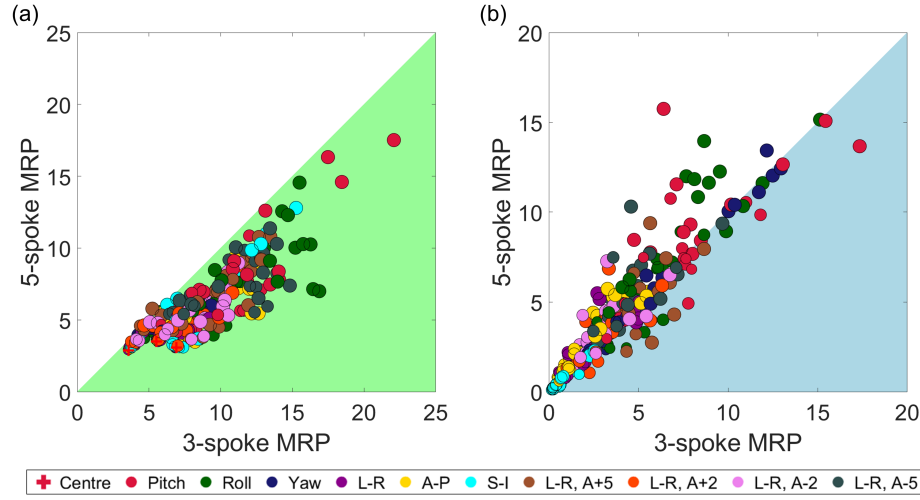


Figure 2.9: (panel a) Magnitude nRMSE and (panel b) phase RMSE evaluations of 5-spoke motion-robust pulses (MRPs) vs 3-spoke MRPs over all evaluated positions, for all slices. Green and blue regions show positions improved by the 5-spoke MRPs and marker size represents the extent of the displacement, either 1, 2 or 5 mm/deg. Considering all slices, the 5-spoke MRPs improved magnitude nRMSE in 316/318 (99%) of positions, reducing mean nRMSE, averaged across positions, from 8.4% ($\sigma = 2.8$) to 5.4% ($\sigma = 2.0$). Phase RMSE was improved in 145/312 (46%) of evaluations, reducing mean RMSE from 4.4° ($\sigma = 3.4$) to 3.9° ($\sigma = 3.1$). The remaining 167/312 (54%) of phase evaluations performed similarly to the 3-spoke MRPs

The RF pulse lengths of the 5-spoke MRP ranged between 7.1 ms and 10.2 ms, and between 4.0 ms and 6.4 ms for the 3-spoke MRPs, across all six slice-selective MRPs. The two extra spokes increased RF pulse lengths by a mean of 71% ($\sigma = 8.3$).

Figure 2.10 shows the magnitude nRMSE and phase RMSE of all 52 off-centre positions for all six slices, and magnitude nRMSEs at the centred positions, for 5-spoke and 3-spoke reference pulses. Similarly to adding spokes to MRPs, more spokes improved reference pulse performance at the centred positions as expected, but also it's motion-robustness in magnitude, reducing mean nRMSE in 274/318 (86%) from 10.7% ($\sigma = 4.6$) to 7.2% ($\sigma = 4.5$). Mean nRMSE was increased in the remaining 44/318 (14%) of evaluations, from 12.7%

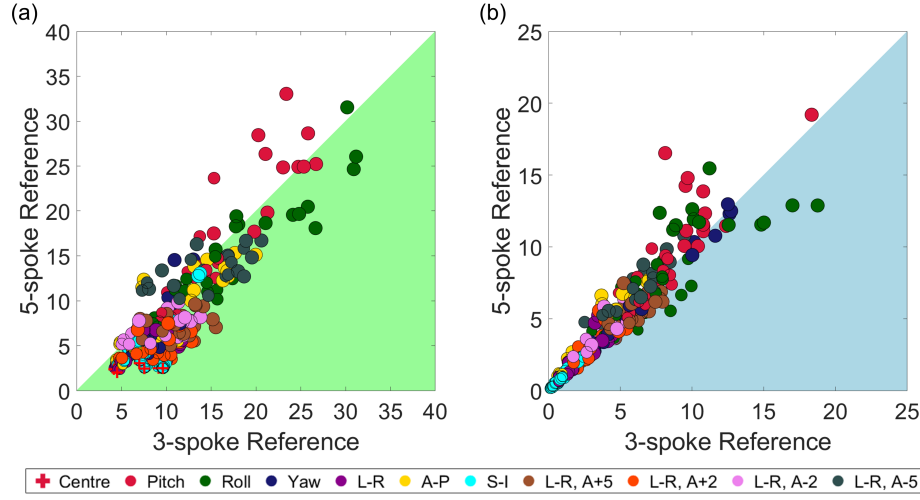


Figure 2.10: (panel a) Magnitude nRMSE and (panel b) phase RMSE evaluations of 5 and 3-spoke reference pulses over all evaluated positions, for all slices. Green and blue regions show positions improved by the 5-spoke reference pulses and marker size represents the extent of the displacement, either 1, 2 or 5 mm/deg. Considering all slices, the 5-spoke reference pulses improved magnitude nRMSE in 274/318 (86%) positions, by an average of 3.5% ($\sigma = 2.0$), and improved phase RMSE in 129/312 (41%) evaluations by an average of 0.6° ($\sigma = 0.9$). The remaining 183/312 (59%) of phase evaluations were degraded, with a mean increase in RMSE of 0.8° ($\sigma = 1.1$).

($\sigma = 6.3$) to 14.7% ($\sigma = 7.3$). The effect on phase was similar to the 5-spoke vs 3-spoke comparison for MRPs (2.9). Phase was improved in 129/312 (41%) of evaluations, reducing mean RMSE from 4.8° ($\sigma = 3.7$) to 4.2° ($\sigma = 3.1$). The remaining 183/312 (59%) of evaluations performed similarly, with the 5-spoke ref-pulses increasing mean RMSE from 4.4° ($\sigma = 3.1$) to 5.2° ($\sigma = 3.7$).

The RF pulse lengths for the 5-spoke ref-pulses were between 7.4 ms and 12.5 ms, and between 4.0 ms and 8.0 ms for the 3-spokes. The two extra spokes increased RF pulse length by an average of 74% ($\sigma = 44.1$).

Figure 2.11 compares the 5-spoke MRPs and 5-spoke ref-pulses. Over all six slices, The MRPs improved 211/318 (66%) magnitude evaluations, reducing mean nRMSE from 10.1% ($\sigma = 5.9$) to 5.8% ($\sigma = 2.3$), averaged across

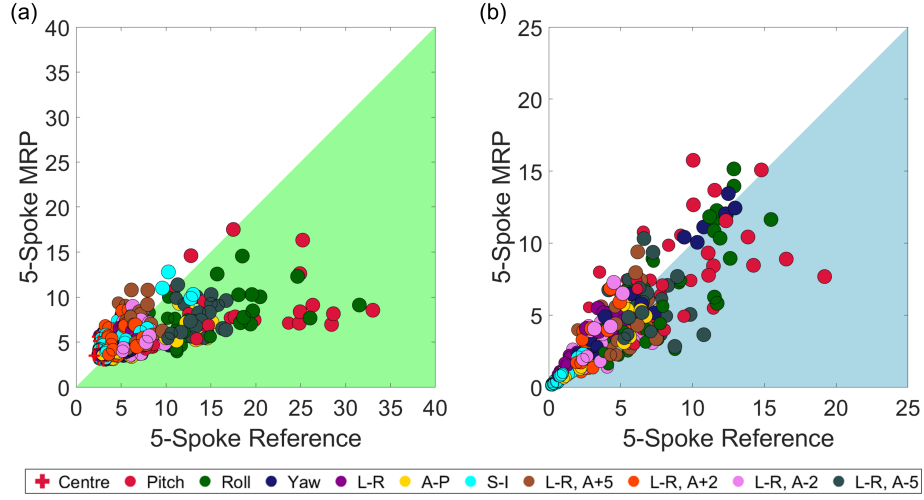


Figure 2.11: (panel a) Magnitude nRMSE and (panel b) phase RMSE evaluations of 5-spoke motion-robust pulses (MRPs) and 5-spoke reference pulses over all evaluated positions, for all slices. Green and blue regions show positions improved by the 5-spoke MRPs and marker size represents the extent of the displacement, either 1, 2 or 5 mm/deg. Considering all slices, the 5-spoke MRPs improved magnitude nRMSE in 211/318 (66%) positions, by an average of 4.3% ($\sigma = 4.5$), and improved phase RMSE in 217/312 (70%) evaluations by an average of 1.4° ($\sigma = 1.6$).

positions. The remaining 34% of positions were degraded but performed similarly to the ref-pulses, increasing mean nRMSE from 4.6% ($\sigma = 2.4$) to 6.2% ($\sigma = 2.4$). For phase, 217/312 (70%) evaluations were improved, reducing mean RMSE from 4.9° ($\sigma = 3.5$) to 3.5° ($\sigma = 2.6$), and increasing mean RMSE in the 30% of positions degraded, from 4.7° ($\sigma = 3.3$) to 5.8° ($\sigma = 3.8$). The MRPs magnitude nRMSEs at the centred positions ranged between 2.9% and 5.6% across slices, and between 2.0% and 3.1% for the ref-pulses. This time only one MRP outperformed the equivalent ref-pulse in the centred position, occurring in the penultimate superior slice (slice 5).

The 5-spoke MRPs had shorter RF pulse lengths compared to the reference pulses for in four of the six slices by up to 18%. In the remaining two slices, MRPs had 3% and 29% longer RF pulse lengths.

2.4 Discussion

This in-silico study demonstrated the initial potential of considering within-scan subject head motion at the pulse design stage as a method for reducing motion-related excitation degradation. Motion-robust spokes pulses demonstrated the ability to maintain more homogeneous magnitude excitations across most off-centre positions compared to conventionally designed spokes pulses.

It was expected that for equal numbers of spokes, the added complexity of improving the flip-angle at multiple positions would mean the MRP could not perform as good as the reference pulse when there is zero motion. For the 3-spoke MRP vs the 3-spoke reference pulse, this was the case for inferior-most and superior-most slices (slices 1 and 6) only. The MRP reported lower magnitude nRMSEs at the centred positions for the remaining four slices. This could be due to the greedy nature of spoke location selection during pulse design, with the additional maps prompting different spoke locations to be selected that could have consequentially led to a better minima of the optimisation. For the 5-spoke MRPs vs the 5-spoke reference pulses, the evaluations at the centred positions were closer to what was expected, with the ref-pulses outperforming the MRPs at the centre for all slices except the penultimate superior slice (slice 5), shown in Figure 2.11.

Considering positions included in the motion-robust design, pitch and roll rotations had the largest mean magnitude nRMSEs and phase RMSEs, calculated across all slices. Pitch and roll rotations also produced the largest reference pulse magnitude and phases errors, but were often the most improved motion type by MRPs in each slice. This can be seen in Figures 2.11 and 2.7. In general, MRPs had a greater effect on high error reference pulse positions compared to lower error positions.

The hardest position to homogenise for the MRPs out of the positions in-

cluded in their design, was the $+5^\circ$ pitch rotation in the inferior-most slice. This could be for two reasons. One is that inferior slices are typically harder to homogenise due to more tissue types and tissue boundaries present within the slice compared to more superior slices. Second, pitch and roll rotations can lead to parts of the slice moving towards the ends of the coil elements, where it is more difficult to homogenise the slice.

The 3-spoke MRPs outperformed the 3-spoke ref-pulses in the majority of magnitude evaluations for all slices, except the inferior-most slice (slice 1), as seen in Table 2.1. Considering magnitude nRMSE, the 3-spoke MRP for the inferior-most slice had the largest range and mean nRMSE across positions and degraded the most evaluation positions. However this was not the case for phase evaluations, where the 3-spoke MRP for the inferior-most slice performed well compared to other slices. Again, this could be due to how spoke locations are selected in the design. The 5-spoke MRPs still outperformed the 5-spoke ref-pulses in the majority of magnitude evaluations (again, excluding the inferior most slice), with average improvement much larger than the average degradation. The 5-spoke and 3-spoke MRP phase evaluations performed well but generally close to the improvement/degradation line. Phase motion sensitivity could be improved by removing phase relaxation from pulse design, however this would have a detrimental effect to the magnitude performance at the centred positions, which would be undesirable for the ref-pulses. When designing pulses for an ideal scenario, where there is no motion, phase relaxation can be very beneficial to flip-angle homogeneity. However, when motion is present, both magnitude and phase of the flip-angle need to be kept consistent to avoid imaging artifacts. Further investigation into the effects of removing phase relaxation from pulse design is needed. While phase relaxation may benefit magnitude homogeneity of MRPs, the detrimental effect to phase may harm overall perfor-

mance.

By adding more spokes to each pulse design, each pulse type saw improvements to magnitude nRMSE motion-robustness. The phase results were less decisive, with each design reporting most evaluations very close to the improvement/degradation line. The 5-spoke MRPs still outperformed the 5-spoke ref-pulses (with the exception of the inferior most slice), however further improvements to the MRP design could be made.

The inclusion of multiple off-centre positions in the MRP design allows for motion-considerate optimisation of the candidate spoke selection during pulse design. This could allow for a better minima than is provided by the current greedy approach to candidate spoke selection. By incorporating a brute-force or quasi brute-force approach to optimising candidate spoke selection, MRP pulse performance could potentially be greatly increased. The effect this would have on the ref-pulse design would be unclear, as only the centred position would be considered when selecting spokes, which could be at great detriment to the pulses motion-sensitivity. The MRP design avoids this unpredictability as the candidate spoke selection is optimised over the centred and off-centre positions. Further investigation into optimising spoke placement was required, and a quasi brute-force candidate spoke selection optimisation is explored in Chapter 3.

As explained in Section 2.2.1, the RF pulse lengths varied across slice-specific pulses because the dwell time was increased to meet the peak RF ($\max B_1^+$) amplitude constraint (30 μ T). The 3-spoke MRPs had a shorter mean RF pulse length (averaged across all slices), compared to the 3-spoke reference pulses, and with less variation. Increasing the number of spokes in the MRP design had a smaller percentage increase in RF pulse length than the reference pulse design, with much less variation across slices. The 5-spoke MRPs also reduced RF pulse length in four out of six slices when compared to the 5-spoke reference

pulses.

Magnitude nRMSE at the centred and off-centre positions could be improved with adding extra spokes, with minor overall effect to the phase evaluations. This introduces a trade off between pulse length and pulse performance. This was to be expected when considering the centred positions only, but it appears to apply to the motion sensitivity of each pulse design method also. Adding extra spokes the MRP design continued to provide improved motion-robustness over the ref-pulses (excluding the inferior most slice). Future work on motion-robust pulse design will focus on improving performance through investigating the effects of removing phase relaxation from pulse design and optimising candidate spoke selection.

2.5 Conclusion

The work presented in this chapter demonstrates the potential of motion-robust excitation pulses as a method of maintaining homogeneous magnitude and phase profiles across the six degrees of freedom of head motion. The motion-robust pulses performed well against conventionally designed reference pulses, and further methods for increasing MRP performance are discussed.

Chapter 3

Non-Phase-Relaxed Motion-Robust Pulses, with Optimisation of Candidate Spoke Selection

3.1 Introduction

Motion-robust spokes pulses (MRPs) have demonstrated in-silico the ability to maintain more homogeneous magnitude profiles in the presence of within-scan patient motion, compared to conventionally designed spokes pulses. However, off-centre phase consistency could be improved.

A magnitude least-squares (MLS) optimisation of RF transmit-channel weightings, by relaxing the uniformity of the phase profile, has been shown to provide improved magnitude profile homogeneity [38]. However, this is performed as-

suming a perfect scenario where no within-scan subject motion is present. Data consistency in the presence of mid-acquisition patient motion requires both magnitude and phase distributions to be consistent across positions. Therefore a phase-relaxed MLS optimisation may not be suitable when designing MRPs.

The selection of spoke placement in k-space can have a drastic effect on the excitation quality of the pulse, and optimising spoke placement has been used before to improve magnitude profile homogeneity [35]. In this work, a quasi-brute force technique for optimising candidate spoke selection was developed to replace the MRPs previously greedy selection of candidate spokes.

Optical motion tracking systems have previously been used as a method for prospective motion correction. In Ref [79], an optical tracker could determine the sample position and rotation in 6 degrees of freedom in real-time with high spatial accuracy. The tracking data that was received could be used to update logical gradient orientations. This approach could have potential application for improving MRP performance, and is investigated in both the MRP and reference pulse designs.

In this work, 5-spoke motion-robust spokes excitation pulses were designed using matrix inversion only, omitting the phase relaxed MLS optimisation used in Chapter 2 (Section 2.2) for MRPs, with the aim of improving off-centre phase profile consistency. The candidate spoke selection was optimised to improve magnitude profile homogeneity by using a quasi-brute-force approach as opposed to the greedy approach used in Chapter 2 (Section 2.2). A more in-depth selection of an appropriate Tikhonov regularisation parameter was also performed, resulting in a Tikhonov parameter of $\beta = 100$ instead of $\beta = 0.1$ used in Chapter 2. While not a direct outcome, $\text{SAR}_{10\text{g-avg}}$ was reported for MRPs and reference pulses. A separate set of MRPs and reference pulses were also designed under real-time gradient updating conditions.

3.2 Methods

The previous approach to designing MRPs was similar to the ref-pulses, including phase relaxed MLS optimisation of RF channel weightings, and a greedy approach to candidate spoke selection. Even though the phase relaxed MLS optimisation improved flip-angle (magnitude) distributions, it was removed from the MRP design to ensure phase consistency across positions. This would have a detrimental effect to the magnitude profiles, however may be countered through optimising the selection of candidate spokes. The phase relaxed MLS optimisation was maintained for the reference pulses as it is commonly used to improve magnitude profile homogeneity, and off-centre phase consistency is not typically considered in conventional spokes pulse design.

Due to the nature of including off-centre positions in the MRP design process, different combinations of spoke locations can be tested to find an optimal solution to reduce error over those off-centre positions. A fully brute force optimisation of the 5×5 k_x - k_y candidate spoke grid (5 m^{-1} spoke separation in k_x, k_y) was computationally intense and time consuming, so a quasi-brute-force approach was used. When each spoke was added, the 10 best performing candidate spokes of the 5×5 candidate grid were evaluated separately. This branching lead to 10,000 pulses for each slice, as the first spoke was always prescribed to be the DC point, $k_x = k_y = 0$. The spoke location combination that produced the lowest magnitude nRMSE, calculated over all design positions, was selected from the 10,000 pulses. This was done separately for each slice, which each had its own set of 10,000 MRPs to select from. This optimisation of spoke locations was not applied to the ref-pulses. The ref-pulses only consider the centred position during their design, so spoke locations would be optimised for this location only which could have detrimental effects to the pulses motion sensitivity. This could artificially boost MRP performance during comparison and so was

avoided. The ref-pulses already performed well at the centred positions due to the benefit of the phase-relaxed MLS optimisation, which was maintained in the ref-pulse design.

Each pulse design included a Tikhonov regularisation term (β) during channel weighting optimisation to control channel-by-channel RF power, as shown in Equation 2.3 in Section 2.2.1. The value of this regularisation can have a large effect on pulse excitation quality and SAR. An l-curve analysis was performed to characterize the trade-off between RF power and magnitude nRMSE (at the centred position) for seven β -values (0.1, 10, 50, 100, 200, 500, 1000) during reference pulse design, and the most appropriate, i.e. with the best trade-off between RF power and magnitude nRMSE, was selected ($\beta = 100$). The MRPs performed best when designed using $\beta = 0.1$.

Although SAR was not a direct outcome of the proposed method, $\text{SAR}_{10\text{g-avg}}$ sensitivity to motion was investigated for each pulse design. The $\text{SAR}_{10\text{g-avg}}$ was evaluated for both the ref-pulses and the MRPs at all 53 positions. Although the MRPs were designed with less regularisation of the RF power, to ensure MRP SAR was not left unchecked, during the optimisation of candidate spoke selection the $\text{SAR}_{10\text{g-avg}}$ was evaluated at the centred position for each of the 10,000 MRPs designed for each slice. The set of MRPs were then filtered for pulses that reported central $\text{SAR}_{10\text{g-avg}}$ (at the centred position) less than or equal to twice the central $\text{SAR}_{10\text{g-avg}}$ of the equivalent slice-selective ref-pulse.

Five-spoke, non-phase relaxed, candidate spoke selection optimised MRPs were designed using the in-silico B_1^+ simulations described in Chapter 2.2.1, for the same 6 axial slices. The MRPs were designed with the same 13 positions:

- Centred case (no motion)
- $\pm 1^\circ$, $\pm 2^\circ$, $\pm 5^\circ$ pitch/roll/yaw rotations
- ± 1 mm, ± 2 mm, ± 5 mm left-right/anterior-posterior/superior-inferior on-

axis translations

- ± 2 mm, ± 5 mm left-right, anterior-posterior off-axis translations

These were compared to standard 3-spoke ref-pulses (with phase relaxation and without candidate spoke selection optimisation). Unless stated otherwise in this section, pulse design parameters were identical to those in Chapter 2.2.1. In Chapter 2.3.2, a 5-spoke MRP was compared against a 5-spoke ref-pulse and continued to show superior motion-robustness. In practice, 3-spoke ref-pulses designed using a phase-relaxed MLS optimisation typically provides suitable flip-angle homogeneity, and so 5-spoke ref-pulses were not investigated further. Optimising over multiple positions increased the complexity of the optimization, and the removal of phase relaxation further reduced pulse performance for magnitude profiles. To accommodate these added complexities, and while maintaining similar magnitude nRMSE to the reference pulses at the centred position, the MRPs used two additional spokes.

Actual 10-g averaged local SAR ($\text{SAR}_{10\text{g-avg}}$) was calculated for the centre and the 52 off-centre positions for all slice-selective MRPs and reference pulses, similar to Section 2.2.1. Central SAR refers to $\text{SAR}_{10\text{g-avg}}$ evaluated at the centred position, and max SAR is the maximum $\text{SAR}_{10\text{g-avg}}$ across all head positions.

Real-time gradient updating is a prospective motion correction technique typically used at lower field strengths ($\sim 3\text{T}$). A set of MRPs and ref-pulses were investigated with real-time gradient updating applied. This was done by replicating the gradient grid of the centred position over all off-centre positions, so the gradients experienced zero motion and only the B_1^+ varied across positions. For MRPs, this required re-optimisation of candidate spoke selections, and so a second gradient-updated set of 10,000 MRPs were designed for each slice, and the pulses reporting the lowest magnitude nRMSEs were selected.

3.3 Results

Non Phase Relaxed Candidate Spoke Optimised MRPs

The trade-off between the RF energy and magnitude nRMSE at the centred position for the six slice-selective reference pulses designed with different Tikhonov regularisation terms (β) are shown in Figure 3.1. Of the seven investigated regularisation terms ($\beta = 0.1, 10, 50, 100, 200, 500, 1000$), the $\beta = 100$ pulses demonstrated a good trade-off between the RF and magnitude nRMSE at the centred position across all slices, and was selected as the regularisation term for the reference pulse design. The “jagged” nature of the curves is the result of the greedy approach to candidate spoke selection during pulse design. The greedy approach adds the most locally optimal candidate spoke during each iteration, which does not guarantee a globally optimal solution compared to a brute-force optimisation over all candidate spoke combinations. Changing the regularisation term prompts a different selection of candidate spokes. This meant that pulses designed with different β -values could be closer or further away from their respective global optimal candidate spoke combinations, which caused the jagged nature of the curves in Figure 3.1. A full brute-force optimisation of the candidate spoke locations would be computationally intense.

The magnitude and phase excitation profiles at the centred position for the $\beta = 100$ ref-pulses are shown in Figure 3.2. Magnitude nRMSE at the centred position ranged between 6.4% and 14.7% across slices.

The magnitude and phase design profiles for the non-phase-relaxed, candidate-spoke-optimised MRPs are shown in Figures 3.3 and 3.4 respectively. The magnitude nRMSEs at the centred positions ranged between 4.3% and 5.5%. Figure 3.5 shows the magnitude nRMSEs (panel a) and phase RMSEs (panel b) across the MRP design positions shown in Figures 3.3 and 3.4. Magnitude nRMSE ranged from 4.2% to 12.0% across all slices and positions. The inferior-most

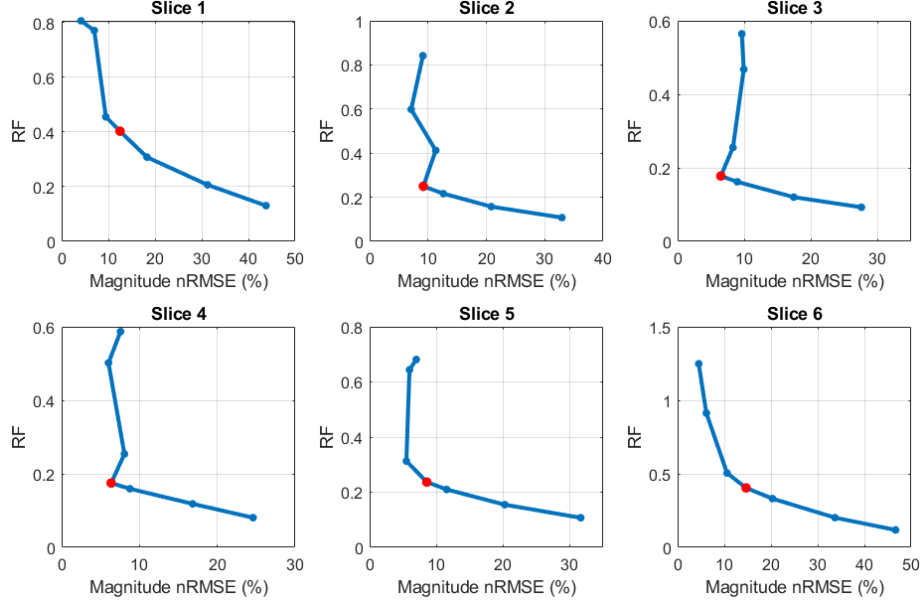


Figure 3.1: The RF vs magnitude nRMSE at the centred position for slice-selective reference pulses designed using different Tikhonov regularisation terms ($\beta = 0.1, 10, 50, 100, 200, 500, 1000$), plotted from left to right respectively. The $\beta = 100$ pulse, shown in red, presented a good trade-off between the RF and magnitude nRMSE at the centred position, and was selected as the regularisation term for reference pulse design.

slice (slice 1) had the largest mean nRMSE (averaged across all design positions), of 8.3% ($\sigma = 2.1$), and one of the middle slices (slice 4) the least (6.4%, $\sigma = 1.8$). The slice-specific ranges in magnitude nRMSE were similar across slices. The centred positions had the lowest nRMSEs except in the middle slices (slices 3 and 4), where a superior-inferior translation showed slightly less error. Off-centre phase RMSE ranged from 0.4° to 10.5° . The penultimate inferior slice (slice 2) had the largest mean RMSE across positions (5.0° , $\sigma = 3.1$), and the penultimate superior slice (slice 5) the least (3.7° , $\sigma = 2.6$). Again there was little variation in the range of phase RMSEs across different slices.

Figure 3.6 shows magnitude nRMSE (panel a) and phase RMSE (panel b) across the positions used in the MRPs design, considering all slices. Taking

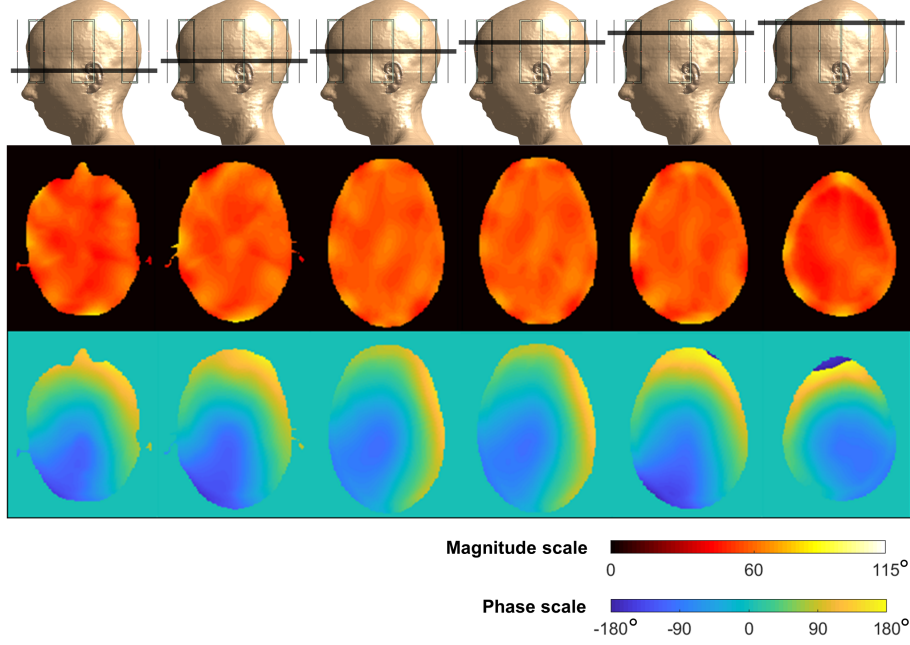


Figure 3.2: The magnitude and phase excitations at the centred positions for the 3-spoke reference pulse ($\beta = 100$) for slices 1 to 6 (left to right). The magnitude nRMSEs at the centred positions for slices 1 to 6 were 12.5%, 9.2%, 6.5%, 6.4%, 8.6%, and 14.7% respectively.

the mean of magnitude nRMSEs of each motion type across positions, pitch rotations reported the largest error (10.2%, $\sigma = 0.9$), and yaw rotations the least (5.8%, $\sigma = 0.7$). The mean magnitude nRMSE across the centred positions was 4.8% ($\sigma = 0.4$). For motion-specific mean phase RMSE across slices, yaw rotations had the largest mean error (6.8°, $\sigma = 3.3$), and superior-inferior translations the least (1.1°, $\sigma = 0.6$). For the design positions, all three rotations produced larger mean phase RMSE across slices compared to translations.

Figure 3.7 demonstrates MRP performance against the ref-pulse in the 53 magnitude nRMSE evaluations (panel a), and the 52 off-centre phase RMSE evaluations (panel b), for all slices. The MRPs improve magnitude nRMSE in 100% of positions, across all slices, reducing mean nRMSE from 11.0% ($\sigma = 3.5$)

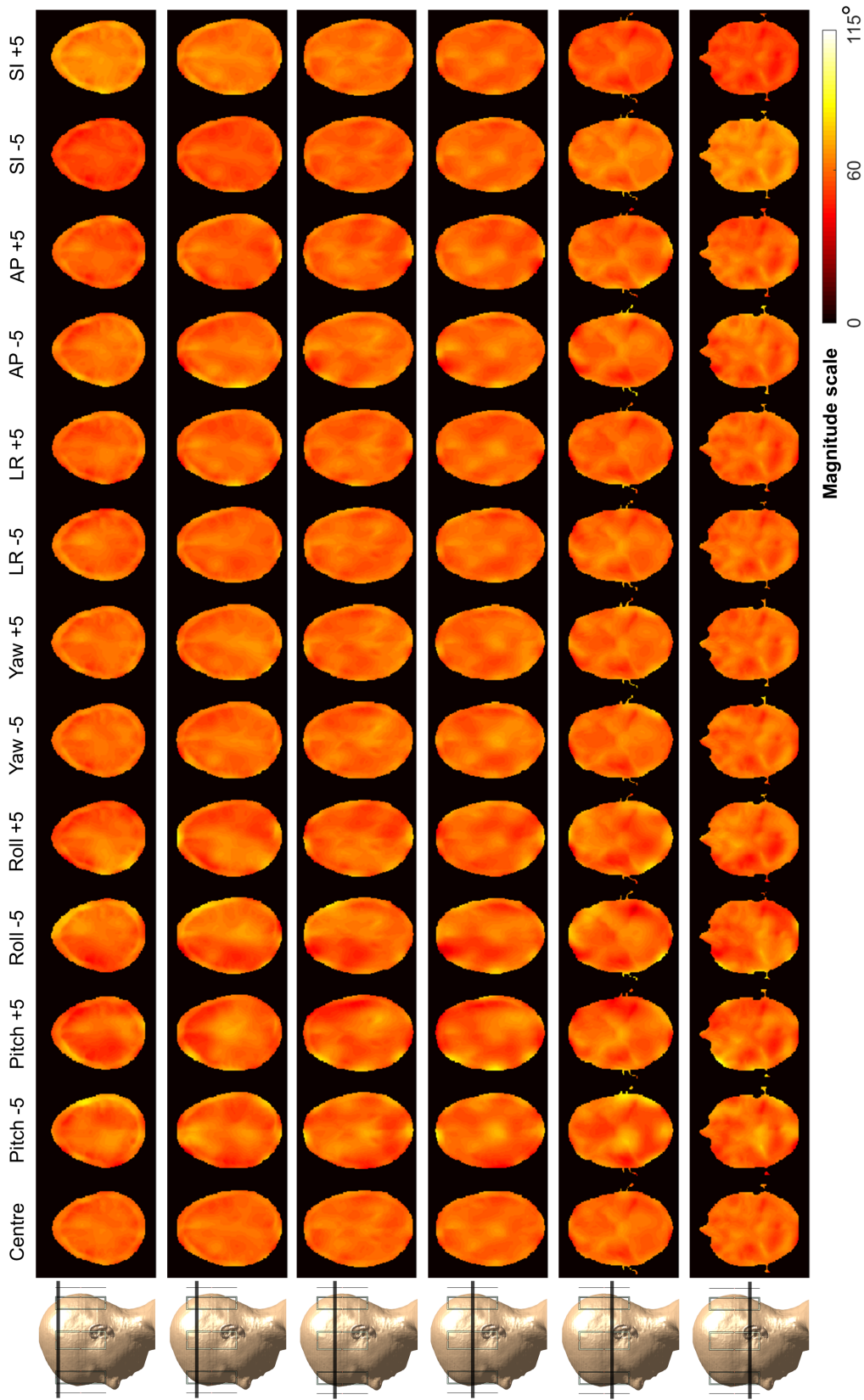


Figure 3.3: The magnitude excitations centred and 12 off-centre positions used in pulse design for the 5-spoke MRP, for slices 1 to 6 (bottom to top). The magnitude nRMSEs at the centred positions for slices 1 to 6 were 5.5%, 5.3%, 4.6%, 4.3%, 4.5%, and 4.6% respectively.

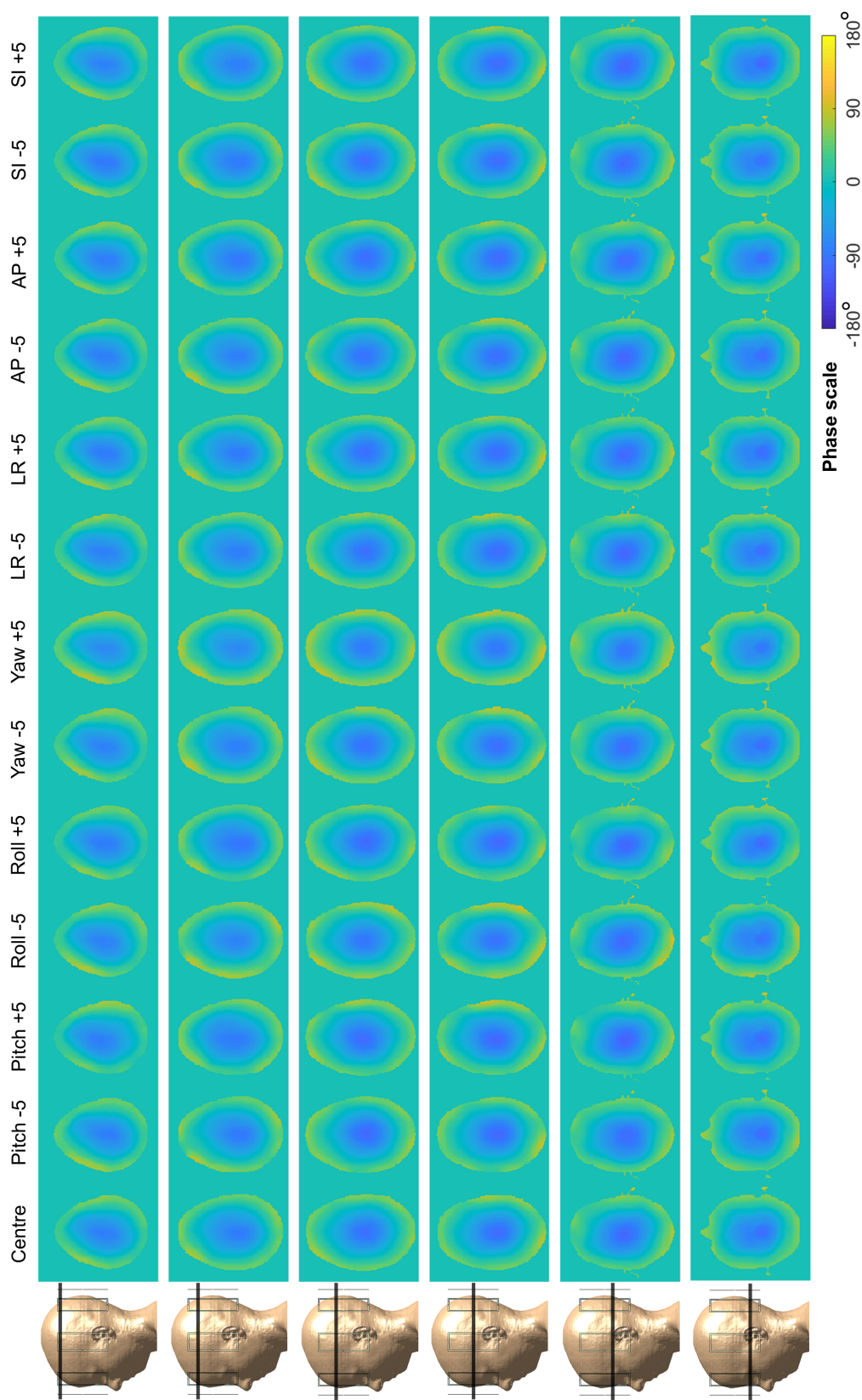


Figure 3.4: The phase excitations centred and 12 off-centre positions used in pulse design for the 5-spoke MRP, for slices 1 to 6 (bottom to top).

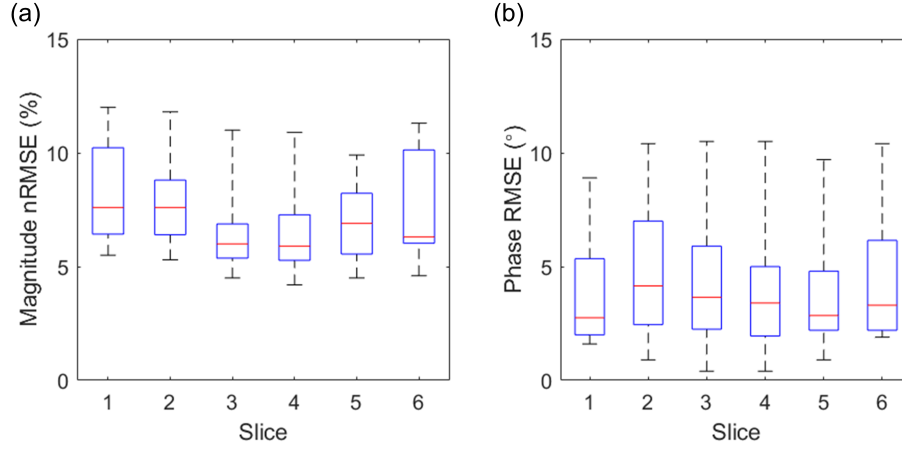


Figure 3.5: Magnitude nRMSE (panel a) and phase RMSE (panel b) across all design positions for all six slice-selective MRPs. For magnitude nRMSE, slices 4 and 6 had the largest range (4.2% - 10.9% and 4.6% - 11.3%, respectively), and slice 5 the least (4.5% - 9.9%). Slice 1 had the largest mean magnitude nRMSE across positions (8.3%, $\sigma = 2.1$), and slice 4 the least (6.4%, $\sigma = 1.8$). For phase RMSE, slice 4 had the largest range (0.4° - 10.5°), and slice 1 the least (1.6° - 8.9°). Slice 2 had the largest mean phase RMSE across positions (5.0°, $\sigma = 3.1$), and slice 5 the least (3.7°, $\sigma = 2.6$).

to 6.2% ($\sigma = 1.5$), averaged across positions. For phase RMSE, 250/312 (80%) of positions were improved, reducing mean RMSE from 5.0° ($\sigma = 3.7$) to 2.7° ($\sigma = 2.0$). The remaining 20% of positions were degraded, but performed similarly, increasing mean RMSE from 2.0° ($\sigma = 1.6$) to 2.8° ($\sigma = 2.0$). The positions that produced the largest errors in phase were rotations for both pulses. Pitch/roll rotations and superior-inferior translations produced the largest magnitude nRMSEs.

Table 3.1 presents the slice-specific number of positions improved/degraded and mean improvement for magnitude evaluations. The MRPs improved magnitude nRMSE at all positions, including at the centred positions, for all slices. The superior-most slice (slice 6) saw the largest improvement in mean nRMSE (averaged across positions), reducing mean nRMSE from 15.6% ($\sigma = 1.8$) to 6.1% ($\sigma = 1.7$); and one of the middle slices (slice 3) the lowest, reducing mean

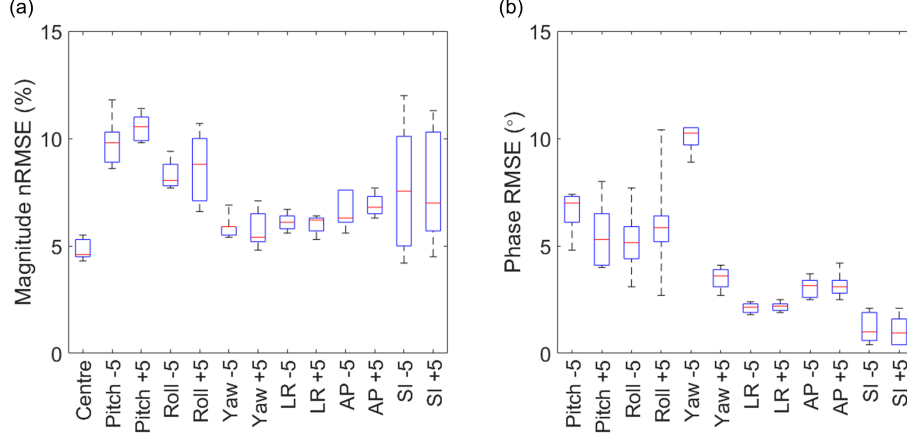


Figure 3.6: Magnitude nRMSE (panel a) and phase RMSE (panel b) for each motion type included in the MRP design, across all six slice-selective MRPs. Pitch, roll and yaw rotations ($^{\circ}$) and left-right (LR), anterior-posterior (AP) and superior-inferior (SI) translations (mm). For magnitude nRMSE, overall, pitch rotations had the largest nRMSE averaged (mean) across positions (10.2%, $\sigma = 0.9$), and the centred positions the smallest (4.8%, $\sigma = 0.4$). For overall phase RMSE, yaw rotations had the largest mean RMSE across positions (6.8°, $\sigma = 3.3$), and superior-inferior translations the smallest (1.1°, $\sigma = 0.6$).

nRMSE from 7.9% ($\sigma = 1.7$) to 5.8% ($\sigma = 1.3$).

Table 3.2 presents the slice-specific number of positions improved/degraded and mean improvement/degradation for phase evaluations. The centred positions are not included as there is no associated error at these positions. The MRPs performed well in phase evaluations, improving the vast majority for all slices. The penultimate superior slice (slice 5) saw the most positions improved, 48/52 (92%), reducing mean RMSE (averaged across positions) from 4.9° ($\sigma = 4.2$) to 2.4° ($\sigma = 2.0$). Mean RMSE was increased in the remaining 4 positions, from 3.8° ($\sigma = 1.4$) to 5.3° ($\sigma = 2.0$). The penultimate inferior slice (slice 2) was the least improved slice, with 36/52 (69%) positions improved, reducing mean RMSE from 5.5° ($\sigma = 4.0$) to 3.2° ($\sigma = 2.5$). Although slice 2 had the most positions degraded, the mean degradation was the lowest, increasing RMSE from 2.4° ($\sigma = 1.8$) to 3.1° ($\sigma = 2.3$).

Magnitude				
Slice	Positions Improved	Positions Degraded	Mean Improvement (%)	σ
1	53	0	6.5	1.5
2	53	0	3.8	0.9
3	53	0	2.1	1.1
4	53	0	2.3	0.9
5	53	0	4.5	1.8
6	53	0	9.5	1.3

Table 3.1: The number of magnitude evaluations (positions) improved/degraded by the MRPs and the mean reduction/increase in magnitude nRMSE (%). The MRPs improved all positions for every slice, including the centred positions

Phase						
Slice	Positions Improved	Positions Degraded	Mean Improvement ($^{\circ}$)	σ	Mean Degradation ($^{\circ}$)	σ
1	41	11	2.5	2.4	0.8	1.0
2	36	16	2.3	2.1	0.6	0.8
3	41	11	2.0	2.5	0.8	1.3
4	43	9	2.1	2.6	0.8	1.3
5	48	4	2.5	3.0	1.5	1.5
6	41	11	2.0	1.9	0.8	0.6

Table 3.2: The number of phase evaluations (positions) improved/degraded by the MRPs and the mean reduction/increase in phase RMSE ($^{\circ}$). The MRPs improved the majority of positions for every slice. Slice 5 saw the most positions improved, and slice 2 the least.

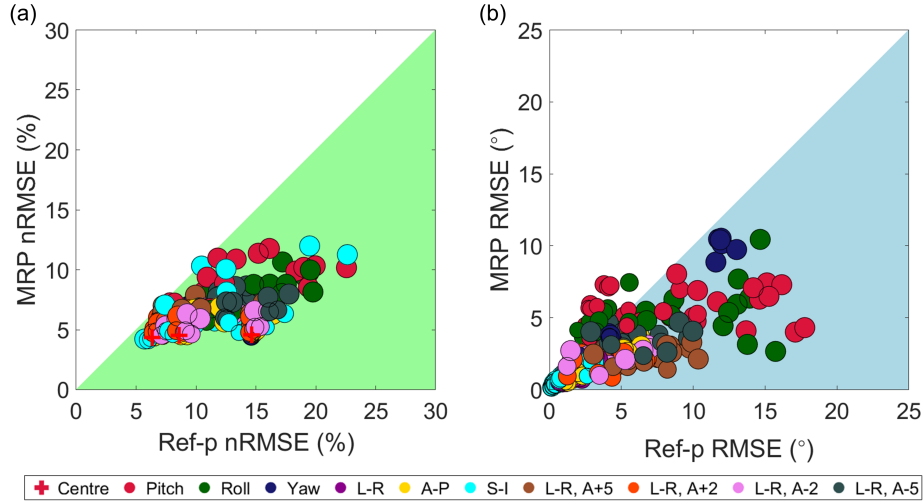


Figure 3.7: (panel a) Magnitude nRMSE (%) and (panel b) phase RMSE (°) of motion-robust pulses (MRPs) vs reference pulses over all evaluated positions, for all slices. Green and blue regions show positions improved by the MRPs and marker size represents the extent of the displacement, either 1, 2 or 5 mm/°. The MRPs improved 100% and 80% of magnitude and phase evaluations, respectively.

The most and least improved slices were determined by averaging the magnitude and phase errors over all evaluated positions for each pulse. Considering both magnitude and phase, the superior-most slice (slice 6) was the most improved by the MRP design, and one of the middle slices (slice 4) the least. The 53 magnitude and 52 phase evaluations for the most improved slice (panel a, panel b), and the least improved slice (panel c, panel d) are shown in Figure 3.8. Even for the least improved slice, the MRP performs well against the ref-pulse, improving all magnitude and 43/52 (83%) of phase evaluations. The number of positions improved/degraded, and the average improvement/degradation for each of these slices is shown in Tables 3.1 and 3.2.

The magnitude and phase excitations for the positions most improved by the MRPs are shown in Figure 3.9. The MRPs were able to reduce areas of high intensity error and maintain more homogeneous magnitude excitations and more

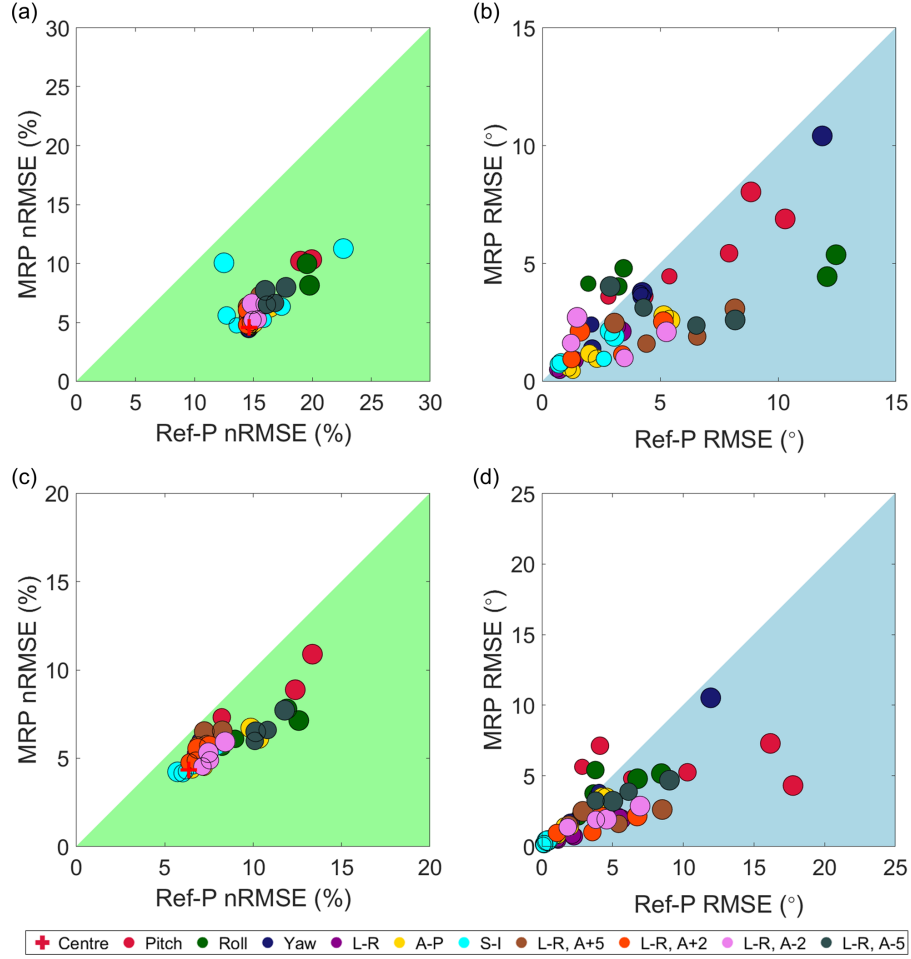


Figure 3.8: The 53 magnitude nRMSE (a, c) and 52 phase RMSE (b, d) evaluations for the slices most (a, b) and least (c, d) improved by the MRP, respectively. The MRP improved 100% of magnitude evaluations in both cases, by an average of 9.5% ($\sigma = 1.3$) for the most improved slice, and 2.3% ($\sigma = 0.9$) for the least improved slice. For the most improved slice, the MRP improved phase in 41/52 (79%) positions by an average of 2° ($\sigma = 1.9$) and degraded 11/52 (21%) by an average of 0.8° ($\sigma = 0.6$). For the least improved slice, phase was improved in 43/52 (83%) positions by an average of 2.1° ($\sigma = 2.6$) and degraded 9/52 (17%) positions by an average of 0.8° ($\sigma = 1.3$).

consistent phase excitations. The MRPs reduced ref-pulse magnitude nRMSE in all slices, with the largest reduction of 11.7% (from 19.8% to 8.1%) occurring in the superior-most slice (slice 6). The smallest reduction in magnitude nRMSE occurred in one of the middle slices (slice 3), reducing error from 11.8% to 11.0%. MRPs also reduced ref-pulse phase RMSE in all slices, with the largest reduction of 13.5° (from 17.8° to 4.3°) in one of the middle slices (slice 4). The smallest reduction in phase RMSE occurred in the penultimate inferior slice (slice 2), reducing phase RMSE from 13.1° to 7.7° .

The magnitude and phase excitations for the positions least improved by the MRPs are shown in Figure 3.10. Here, the worst MRP performance is shown, however the MRPs were still able to reduce areas of high intensity error and maintain better homogeneity in magnitude excitations (lower magnitude profile nRMSE) compared to ref-pulses. The MRPs also showed more consistent phase excitations in the two superior-most slices (slices 5 and 6) and one of the middle slices (slice 4). The MRPs degraded phase RMSE in the remaining three slices but by a maximum of 0.2° .

Slice-specific left-tailed paired t-tests with a 5% significance level ($p \leq 0.05$), that considered all off-centre positions, showed the MRPs statistically improved all magnitude and phase evaluations against the ref-pulses, for each slice. For both the magnitude and phase evaluations, all slice-specific MRPs p -values were $p < 0.001$, even for the least improved slice.

Figure 3.11 (panel a) shows the central and maximum off-centre $\text{SAR}_{10\text{g-avg}}$ respectively, for all slice-specific MRPs and ref-pulses. Figure 3.11 (panel b) shows a violin plot of the off-centre $\text{SAR}_{10\text{g-avg}}$ relative to the central $\text{SAR}_{10\text{g-avg}}$ for the MRPs and ref-pulses, considering all slices. The MRPs reduced central and maximum $\text{SAR}_{10\text{g-avg}}$ in the two middle slices and the penultimate superior slice (slices 3, 4, and 5) by an average of 4.9 W/kg ($\sigma = 4.2$) and 6.0 W/kg

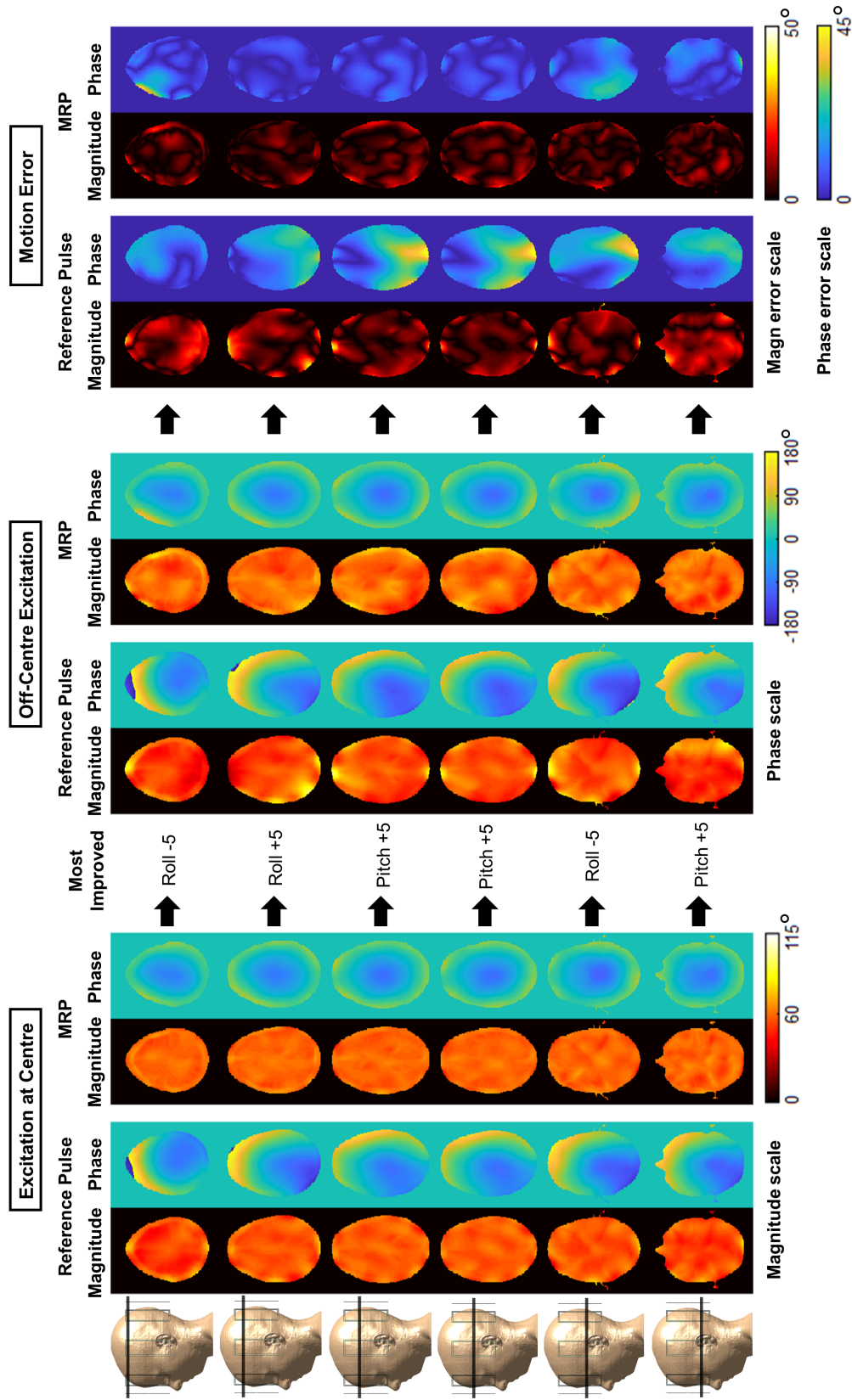


Figure 3.9: The magnitude and phase excitations at the centred positions, most improved off-centre excitations, and difference profiles. For slices 1 to 6, the MRPs reduced ref-pulse magnitude nRMSE from 19.4% to 9.8%, 16.2% to 8.8%, 11.8% to 11.0%, 13.4% to 10.9%, 17.5% to 8.8%, and 19.8% to 8.1% respectively. For phase, the MRPs reduced ref-pulse RMSE from 13.7° to 4.1°, 13.1° to 7.7°, 17.1° to 4.0°, 17.8° to 4.3°, 15.7° to 2.7°, and 12.1° to 4.4°, for slices 1 to 6 respectively. Where motion error is shown as zero, this is where the pulses achieved the target flip angle (magnitude), or achieved consistent phase with the centred position.

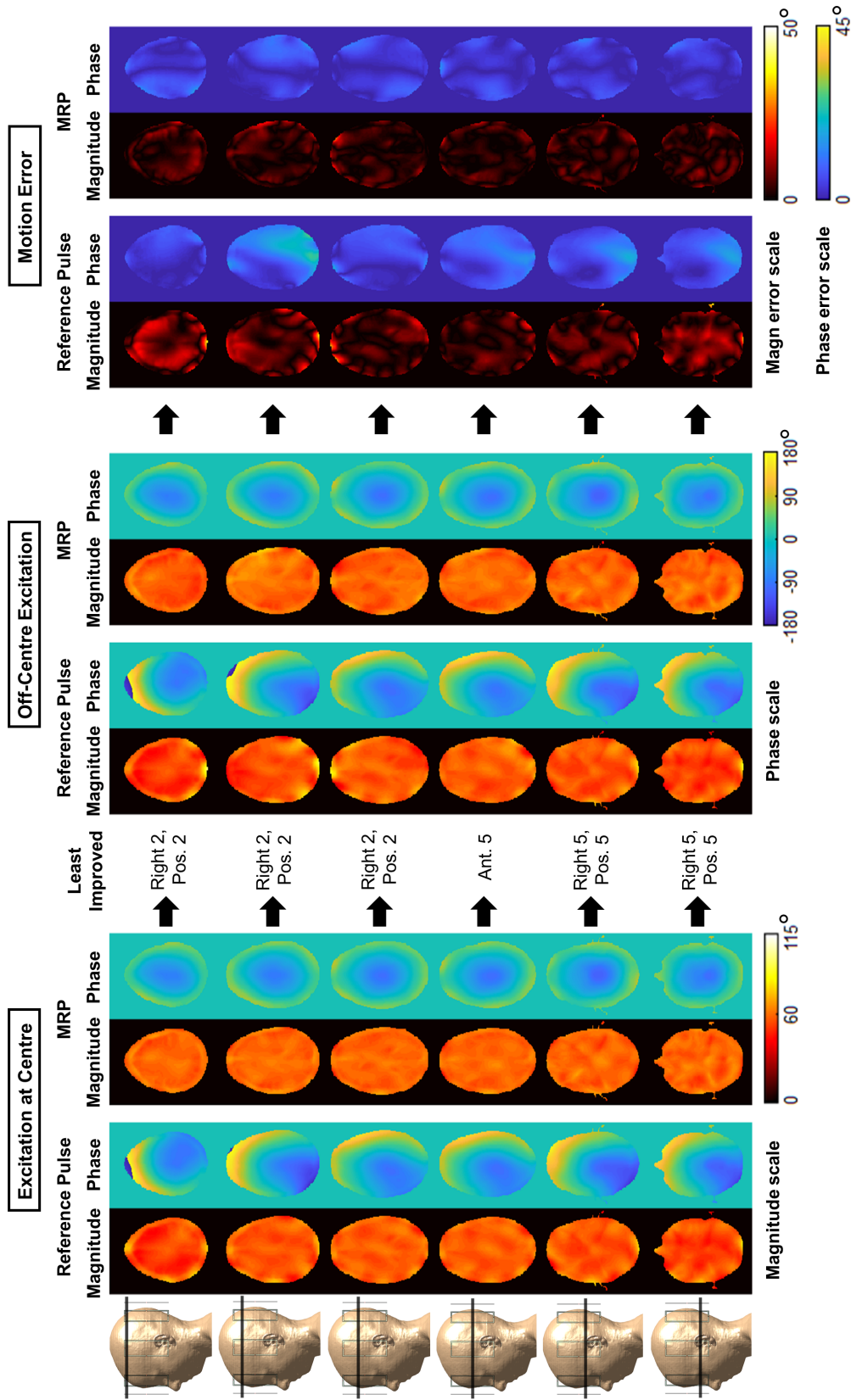


Figure 3.10: The magnitude and phase excitations at the centred positions, least improved off-centre excitations, and difference profiles. For slices 1 to 6, the MRPs reduced ref-pulse magnitude nRMSE from 10.5% to 10.3%, 8.0% to 5.9%, 7.5% to 6.1%, 5.7% to 4.2%, 7.4% to 7.1%, and 12.5% to 10.1% respectively. For phase, the MRPs reduced ref-pulse RMSE in slices 3, 5, and 6, from 1.9° to 1.7°, 1.0° to 0.9°, 3.1° to 1.9°, respectively. Phase RMSE was degraded in slices 1, 2, and 4, from 1.4° to 1.6°, 0.8° to 0.9°, and 1.4° to 1.6°, for slices 1 to 6 respectively.

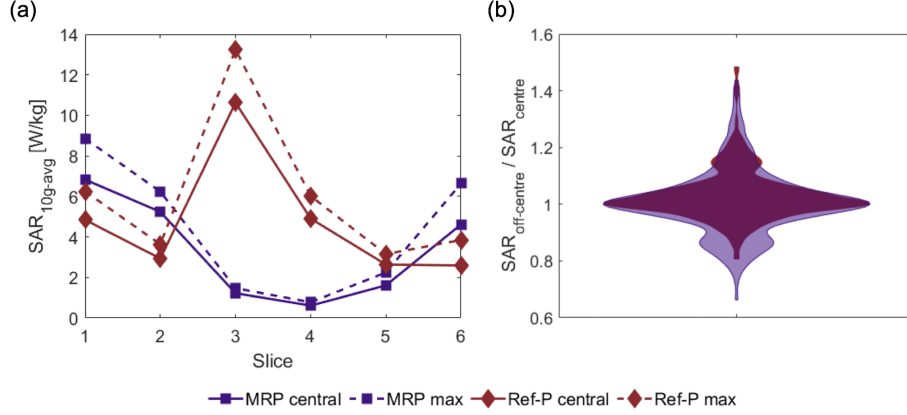


Figure 3.11: (panel a) The central $SAR_{10g-avg}$ and maximum off-centre $SAR_{10g-avg}$ for all slice specific MRPs and reference pulses (Ref-Ps). (panel b) A violin plot of the relative $SAR_{10g-avg}$ between off-centre positions and the centre. The MRPs reduced central and maximum $SAR_{10g-avg}$ in 3/6 slices by an average of 4.9 W/kg ($\sigma = 4.2$) and 6.0 W/kg ($\sigma = 5.5$) respectively. The MRPs increased central and maximum $SAR_{10g-avg}$ in 3/6 slices by an average of 2.1 W/kg ($\sigma = 0.2$) and 2.7 W/kg ($\sigma = 0.1$) respectively.

($\sigma = 5.5$) respectively. The MRPs increased central and maximum $SAR_{10g-avg}$ in the remaining three slices by an average of 2.1 W/kg ($\sigma = 0.2$) and 2.7 W/kg ($\sigma = 0.1$) respectively. The difference between the central and maximum off-centre $SAR_{10g-avg}$ was small, with an average difference of 1.3 W/kg ($\sigma = 0.7$) for the ref-pulses, and 1.0 W/kg ($\sigma = 0.8$) for the MRPs.

By using two extra spokes, the MRPs had longer RF pulse lengths than the ref-pulses. The average MRP pulse length, over the six slice-selective MRPs was 10 ms ($\sigma = 1.2$), and 4 ms ($\sigma < 0.001$) for the ref-pulses. This introduces a trade off between motion-robustness and RF pulse length.

Adding Real-Time Gradient Updating

Figure 3.12 (panel a, panel b) show the magnitude and phase evaluations respectively, of the ref-pulses with real-time gradient updating (GU-Ref-Ps), against the ref-pulses with no updating (Ref-Ps). For magnitude evaluations, the GU-

Ref-Ps improved 123/318 (39%) of positions, reducing mean nRMSE (averaged across positions), from 12.0% ($\sigma = 3.5$) to 10.9% ($\sigma = 3.3$). Mean nRMSE was degraded in 153/318 (48%) positions from 9.9% ($\sigma = 3.1$) to 10.3% ($\sigma = 3.0$). For phase evaluations, The GU-Ref-Ps improved 205/312 (66%) of positions reducing mean RMSE from 5.3° ($\sigma = 3.8$) to 2.1° ($\sigma = 1.3$); and increasing mean RMSE from 3.6° ($\sigma = 2.5$) to 4.3° ($\sigma = 2.8$) in the remaining 71/312 (23%) of positions. The remaining 13% of magnitude and 11% of phase evaluations consisted of the centred positions (magnitude only) and S-I translations, which were not affected by updating gradients.

Figure 3.12 (panel c, panel d) shows magnitude and phase evaluations respectively, for the MRPs (no gradient updating) against the GU-Ref-Ps. For magnitude evaluations, the MRPs maintained strong performance and improved nRMSE in 309/318 (97%) of evaluations, reducing mean nRMSE (averaged across positions) from 10.6% ($\sigma = 3.2$) to 6.1% ($\sigma = 1.4$). The remaining 9/318 (3%) of evaluations were degraded, increasing mean nRMSE from 7.6% ($\sigma = 1.5$) to 9.1% ($\sigma = 1.7$). For phase evaluations, the MRPs performed poorly against the GU-Ref-P's, improving 106/312 (34%) of evaluations, reducing mean RMSE from 3.3° ($\sigma = 2.8$) to 2.6° ($\sigma = 2.2$). The remaining 206/312 (66%) of evaluations performed similarly, but were degraded. Averaged across degraded positions, mean RMSE was increased from 2.0° ($\sigma = 1.3$) to 2.9° ($\sigma = 2.1$).

The magnitude and phase evaluations for the gradient updated MRPs (GU-MRPs) against the GU-Ref-Ps are shown in Figure 3.12 (panel e, panel f), respectively. The GU-MRPs improved 100% of magnitude evaluations, reducing mean nRMSE (averaged across positions) from 10.5% ($\sigma = 3.2$) to 5.3% ($\sigma = 1.4$). For phase, the GU-MRPs improved 175/312 (56%) positions, reducing mean RMSE from 2.7° ($\sigma = 2.4$) to 2.1° ($\sigma = 2.1$); and increasing mean RMSE in the remaining 44% of evaluations, from 2.2° ($\sigma = 1.3$) to 2.6° ($\sigma = 1.7$).

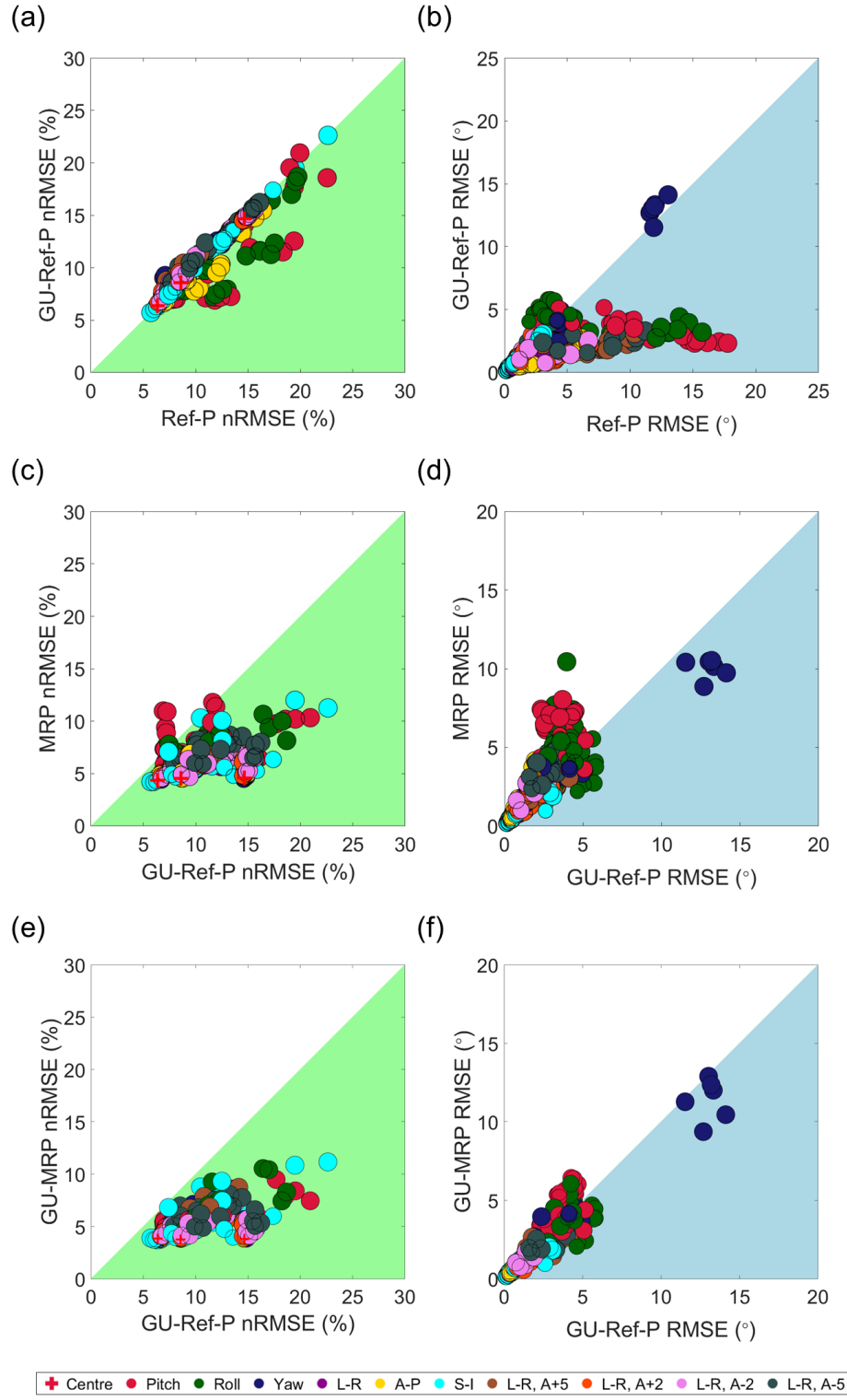


Figure 3.12: The magnitude and phase evaluations of the gradient updated Ref-Ps (GU-Ref-Ps) vs the Ref-Ps (a, b), the MRPs vs the GU-Ref-Ps (c, d), and the GU-MRPs vs the GU-Ref-Ps (e, f), over all positions for all slices (318 magnitude, 312 phase).

3.4 Discussion

This work aimed to improve the previously presented motion-robust excitation pulses (Chapter 2) by removing the phase relaxed MLS optimisation and applying a quasi brute-force optimisation to candidate spoke selection. All six slice-selective MRPs showed impressive performance in maintaining homogeneous magnitude and consistent phase across off-centre positions. Where previously MRPs struggled to improve off-centre positions in the inferior-most slice (shown in Chapter 2), the new MRP design showed drastically improved performance, when evaluated over the same positions.

As expected, larger displacements yielded larger motion error. Furthermore, roll and pitch rotations and superior-inferior translations generally yielded larger magnitude error compared to other motion types. However, superior-inferior motion showed relatively small phase error, with rotations causing the largest phase errors. Consequently, the benefit of using MRPs was larger for larger displacements and pitch and roll rotations.

When selecting spoke locations, combinations that minimised magnitude error, phase error, or an average of both, were investigated. When selecting for minimal phase RMSE, the degradation in the magnitude profiles was much higher, compared to the degradation in phase distributions when selecting for magnitude nRMSE. Removing phase relaxation for MRP design mitigated the degradation in phase considerably. Therefore, the spoke locations that minimized magnitude error were chosen, even though this leads to the benefit of MRPs being generally higher for magnitude profiles than the phase distributions.

When designing the reference pulses, a greedy approach was used compared to the quasi brute-force solution utilised for MRP design. A similar quasi brute force approach was also tried for the reference pulses. While it improved the

magnitude error at the centred position (phase error was irrelevant as phase relaxation was active), it empirically led to unpredictable, and sometimes considerable, increases in the pulse’s motion sensitivity, and therefore was not pursued further.

Varying the RF power regularisation affected reference pulse magnitude homogeneity performance. The non-monotonic behaviour across β -values is attributed to variations in spoke locations across pulses due to the greedy spoke selection algorithm. MRP spoke locations were filtered considering reference pulse central $\text{SAR}_{10\text{g-avg}}$. The β -value used for the reference pulse influences its $\text{SAR}_{10\text{g-avg}}$, and therefore, it affects MRP spoke locations. Considering the added level of complexity for optimising over multiple patient position, overly constraining the RF power could lead to poor MRP performance. Instead, central $\text{SAR}_{10\text{g-avg}}$ was constrained by filtering MRP spoke location combinations by a tolerance of twice the central $\text{SAR}_{10\text{g-avg}}$ of the equivalent reference pulse. Central $\text{SAR}_{10\text{g-avg}}$ for each slice is shown in Figure 3.11. To prevent a secondary regularization, the Tikhonov regularization parameter β was kept at the lower value ($\beta = 0.1$) and unchanged across MRP pulses. Despite using a lesser β , MRPs reported lower $\text{SAR}_{10\text{g-avg}}$ in three of the six slices, and lower maximum off-centre $\text{SAR}_{10\text{g-avg}}$ in the same slices. In the remaining three slices, central and maximum $\text{SAR}_{10\text{g-avg}}$ were larger for MRPs, with MRP central $\text{SAR}_{10\text{g-avg}}$ never exceeding 1.8 times the equivalent ref-pulse central $\text{SAR}_{10\text{g-avg}}$ (shown in Figure 3.11). Although MRP candidate spoke selection was constrained by central ref-pulse $\text{SAR}_{10\text{g-avg}}$, the maximum off-centre $\text{SAR}_{10\text{g-avg}}$ for all MRPs never exceeded 1.7 times the equivalent maximum ref-pulse $\text{SAR}_{10\text{g-avg}}$. Normalising each pulse in time could have yielded different results, however the design constraint here was maximum B_1^+ amplitude. Pulses could have been normalised to the same duration [84], although two additional spokes were ex-

plicitly added to the MRPs to account for added pulse design complexities, and it was undesirable to further constrain the pulses.

A set of ref-pulses and MRPs were designed assuming real-time gradient updating was available through an optimal motion tracking system such as in Ref [79]. The gradient updated ref-pulses (GU-Ref-Ps) showed far superior phase consistency to those with no gradient updating, however magnitude performance was similar. Although the GU-Ref-Ps degraded the majority of magnitude evaluations, the mean increase in nRMSE was far smaller than the mean reduction in nRMSE in the improved positions. Considering both magnitude and phase evaluations, the GU-Ref-P is determined as a superior pulse to the standard Ref-Ps when motion is considered. The excitations at the centred positions were unaffected. The GU-Ref-Ps were then compared to the standard, non-gradient updated MRPs. While the MRPs maintained far superior magnitude excitations, the much stronger phase consistency of the GU-Ref-Ps meant they outperformed the MRPs in the majority of phase evaluations. The same real-time gradient updating consideration was then applied to the MRP design (GU-MRPs), which also saw improvements in magnitude and phase as a result. The GU-MRPs were compared to the GU-Ref-Ps and improved every magnitude evaluation. The GU-MRPs also now outperformed the GU-Ref-Ps in the majority of phase evaluations, however overall phase performance remained similar between the two pulse designs. Considering both magnitude and phase evaluations, it is clear that the GU-MRPs outperformed the GU-Ref-Ps, and so even if using a motion tracking camera for real-time gradient updating, excitation quality in the presence of within-scan subject motion can still be greatly improved with the use of the MRP approach to pulse design. However, optical motion tracking within a pTx coil presents a set of hardware challenges that have yet to be overcome in the literature. For this reason, real-time gradient

updating was not carried forward in further investigations of the MRP design.

A non-phase-relaxed 3-spoke MRP with candidate spoke selection optimisation was designed and evaluated against the 3-spoke reference pulse. The MRP performed well in phase evaluations, but sufficiently poorly in magnitude evaluations to discard the pulse. This is because the candidate spoke selection optimisation was not sufficient enough to counteract the removal of the phase-relaxed MLS optimisation, due to the lower number of spokes. If an RF pulse length shorter than the 5-spoke MRPs from this chapter is critical, then the 3-spoke MRPs with phase relaxation and greedy candidate spoke selection (from Chapter 2) should be chosen over a 3-spoke MRP designed using the approach in this chapter.

There are two main discrepancies between the simulated data used in this work, and typical experimental (in-vivo) data. One is that pulses in this work were designed under the assumption of a homogeneous B_0 field in order not to overshadow the benefits and pitfalls of using MRPs for rigid head motion. Secondly, it was assumed there were no off-resonance effects. However, it has previously been shown by Grissom *et al.* in Ref [35], measured off-resonance maps can be used during pulse design to reduce excitation error for pTx pulses, which has potential to benefit the MRP design also. Nevertheless, for in-vivo scanning there will be B_0 effects which would need to be accounted for, and further investigation into how B_0 inhomogeneity, and off-resonance effects would impact the design is needed and discussed in Chapter 6.2. It was also assumed that the accepted power into the coil was consistent during simulation, which may not be the case in experiment. Further work to better understand the effects of this is also needed.

This method needs B_1^+ -maps acquired at multiple head positions, which would not be feasible in clinical practice. However, recent work has shown

promising results in estimating off-centre B_1^+ -maps using deep learning in less than 20 ms [1]. This work forms the basis of the next chapter of this thesis (Chapter 4). Alternatively, a representative library of pre-designed MRPs can be built and the best matching pulse (to the current patients head shape and size) can be used, similar to the approach in Ref [85]. Universal pulses, designed over multiple participants (in the lack of motion), have already been investigated [86]. A third approach could extend the work done on universal pulses to include multiple motion states and design a single motion-robust universal pulse.

3.5 Conclusion

The results presented demonstrate in-silico that motion-robust excitation pulses can be used as a method for maintaining highly homogeneous flip-angle magnitude profiles and consistent phase in the presence of patient head motion. If motion is expected during imaging, for example in cohorts who cannot or may forget to keep still, such as Parkinson’s, dementia/Alzheimer’s, or paediatric imaging, then motion-robust pulses may have potential for reducing motion-artifacts and increasing image quality. Further work to improve the practicality of the design, by finding a solution to the necessity for many input B_1^+ -maps, is required to make these motion-robust excitation pulses more feasible.

Chapter 4

Motion-Robust pTx

Excitation Pulse Design

Using Estimated B_1^+ -maps

Predicted Using Deep

Learning

4.1 Introduction

The work presented in this thesis so far has demonstrated the potential of motion-robust excitation pulses (MRPs) for mitigating within-scan motion-induced magnitude inhomogeneity and phase inconsistency. However, in order to optimise channel weightings to consider multiple patient positions, the de-

sign requires many input B_1^+ -maps. These would need to be collected at the start of a scanning session, using B_1^+ -mapping sequences with the subject at many different positions. This would increase scan times and could be difficult to achieve with certain cohorts such as children or dementia patients, greatly limiting the practicality of the current MRP design.

Recent work has shown that by using deep learning, motion resolved B_1^+ -maps can be estimated in a pTx coil [1]. Plumley *et al.* performed in-silico field simulations of the centred position and 32 off-centre positions for four realistic body models from the Virtual Population (Dizzy, Billy, Duke and Ella), within a generic 8-channel pTx coil using Sim4Life (Zurich MedTech, Zurich, CH) [44, 80]. Then a system of conditional generative adversarial networks [87] were trained to predict pTx B_1^+ -maps at off-centre subject positions from the B_1^+ -map at the centred position, suitable for use in real-time RF pulse redesign. They found the error in the predicted B_1^+ -maps was lower than the motion-affected B_1^+ in 99% of magnitude evaluations, and 67% of phase evaluations. The worst-case flip-angle nRMSE due to motion was reduced by 59% using pulses that were redesigned using the the predicted B_1^+ -maps. The prediction error across the networks trained for magnitude in the right-posterior translations, considering all four body models, was $4.5\% \pm 1.5\%$ (mean \pm SD) of the ground truth B_1^+ magnitude. The results presented by Plumley *et al.* showed potential for addressing the need for multiple B_1^+ -maps in the motion-robust pulse (MRP) design. It would also allow for any number of positions to be included in the design of the MRPs, which could allow for increased motion-robustness. Varying the number of input B_1^+ -maps is investigated in this chapter.

Real-time pulse redesign using predicted B_1^+ -maps can be an effective method for reducing motion-related magnitude and phase inhomogeneity [76]. With the combination of motion tracking to understand current patient co-ordinates, a

B_1^+ -map could be estimated at the current patient position for real-time pulse redesign. Alternatively, a library of estimated B_1^+ -maps at different positions could be populated throughout the scan, and motion tracking information used to select the most appropriate B_1^+ -map for the current patient position. MRPs consider multiple positions during initial pulse design, providing a more “plug and play” approach, and can be performed with standard scanner computer hardware without the need for additional computational resources for real-time pulse redesign. For MRP application in-vivo, like other prospective motion correction techniques, motion tracking would be required to adjust the slice orientation/position as well as adapt the gradient waveforms for signal acquisition [79, 88, 89].

In this work, motion-robust pTx spokes excitation pulses were designed using estimated off-centre B_1^+ -maps from Ref [1], and a similar approach to Chapter 3.2. All slice-specific off-centre B_1^+ -maps were previously estimated from a single acquired (simulated) B_1^+ -map of the equivalent slice. The MRPs were compared to conventionally designed spokes pulses, and excitation quality was compared. To investigate how the number of input B_1^+ -maps affected the MRP design, three sets of six slice-selective MRPs were designed, the first using all 23 available positions, the second using 18, and the third using 10. All three sets were evaluated over all 23 positions.

4.2 Methods

The centred and twenty two estimated off-centre B_1^+ -maps for six axial slices of the “Billie” body model were provided by Plumley *et al.* [1]. The B_1^+ -map simulation set-up used by Plumley *et al.* in Ref [1] was identical to that described in Chapter 2.2.1. Simulations of the B_1^+ -maps at different head positions were performed using Sim4Life. The same generic 8-channel pTx coil was used (8

loops, 40 mm width, 110 mm height, 230 mm inner diameter and 3 mm microstrip width), and different head positions were achieved by displacing the coil relative to the head models. This ensured the voxelisation of the head did not vary across different positions. The off-centre ground truth maps (simulated in Sim4Life, not estimated using the deep learning network), were also provided for each position. The B_1^+ -maps were simulated at a resolution of 122x151 voxels but were interpolated to a resolution of 256x256 voxels. The slice locations and off-centre head positions are shown in Figure 4.1, and included larger magnitude movements, up to 20 mm translations and 15° rotations, compared to the 5 mm translations and 5° rotations investigated in Chapters 2 and 3.2. The simulated head positions were:

- Centred location (no motion)
- 2 mm, 5 mm, 10 mm, 20 mm on-axis translations towards right
- 2 mm, 5 mm, 10 mm on-axis translations towards posterior
- off-axis translation towards right 2 mm, 5 mm, 10 mm, 20 mm, and posterior 2 mm, 5 mm, 10 mm
- 5°, 10°, 15° clockwise yaw rotations (about the centre of the head)

In this work, when discussing off-axis translations, shifts in the right direction are grouped under the posterior shift. For example, a 10 mm posterior off-axis translation refers to a 10 mm on-axis posterior shift, and then 2/5/10/20 mm shifts in the right axis.

During B_1^+ -map estimation, phase wrapping can introduce artificial phase boundaries, which was responsible for most of the phase-prediction error in Ref [1]. To prevent this, Plumley *et al.* introduced random spatially invariant phase offsets to pairs of input B_1^+ -maps during training, in order to artificially move the phase wrapping boundaries and reduce the coherence of these

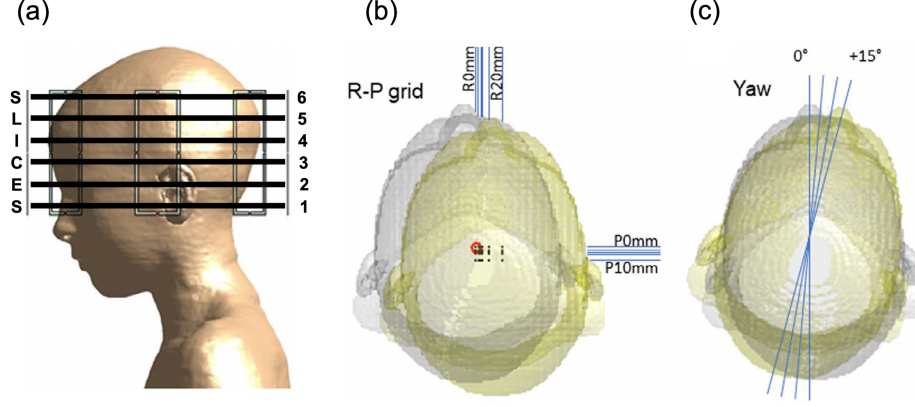


Figure 4.1: (panel a) The 6 slice locations and (panel b, panel c) 23 head positions of predicted and ground-truth B_1^+ -maps of the “Billie” body model provided by Plumley *et al.* for MRP design and evaluation. Positions included on and off-axis translations in the right and posterior directions, and three yaw rotations. Three sets of six slice-selective MRPs were designed by optimising pTx channel weightings over different combinations of positions shown in (panel b) and (panel c) for each slice shown in (panel a).

boundaries across the training data. However, this approach was not suitable for the MRP design, as it introduced inconsistent phase distributions at the centred position associated with each off-centre position. The MRPs aim to maintain a consistent phase profile across all design positions, and so cannot have off-centre specific phase distributions at the centred position. Therefore, the network training process was run without introducing the spatially invariant phase off-sets. This introduced “cracking” in the predicted B_1^+ -maps which corresponded to non-smooth phase boundaries, which were produced because it is difficult for the deep learning method to predict phase boundaries accurately. These B_1^+ -maps were then used as inputs for pulse design. The non-smooth phase boundaries in the input B_1^+ -maps produced relatively large errors in the excitation, although only affected a small number of voxels, and had only a minor effect on MRP performance. The nature of the phase boundaries were different across B_1^+ -maps, and were well homogenized with other voxels by the

l_2 -norm cost function during MRP pulse design. The reference pulses were unaffected because only ground-truth B_1^+ -maps at the centred positions are used in their design. Therefore, due to the nature of the design requirements of the MRPs, the phase of the predicted complex B_1^+ -maps provided by Plumley *et al.* for this work differed slightly from those in Ref [1], however the magnitude was unaffected.

Previous work on MRPs (Chapters 2 and 3.2) considered motion up to 5° and 5 mm. Here displacements up to 15° and 20 mm are tested. It was postulated that these positions could dominate the optimisation and reduce overall pulse performance. To investigate how the input B_1^+ -map selection affected the design, three sets of six slice-selective MRPs were designed, each using the simulated B_1^+ -map at the centred position, and different numbers of estimated B_1^+ -maps. The first set of MRPs ($\text{MRPs}_{\text{set-1}}$), included motion up to maximums of $15^\circ/20$ mm, and all 23 positions as inputs. The MRPs for set 2 ($\text{MRPs}_{\text{set-2}}$) included fewer positions (18 input positions), up to smaller maximum displacements of $10^\circ/10$ mm:

- Centred case (no motion)
- 2 mm, 5 mm, 10 mm right on-axis translations
- 2 mm, 5 mm, 10 mm posterior on-axis translations
- 2 mm, 5 mm, 10 mm right, 2 mm, 5 mm, 10 mm posterior off-axis translations
- 5° , 10° clockwise yaw rotations (about the centre of the head)

MRPs for set 3 ($\text{MRPs}_{\text{set-3}}$) included fewer positions again (10 input positions), up to smaller maximums of $5^\circ/5$ mm:

- Centred case (no motion)

- 2 mm, 5 mm, right on-axis translations
- 2 mm, 5 mm, posterior on-axis translations
- 2 mm, 5 mm, right, 2 mm, 5 mm, posterior off-axis translations
- 5° , clockwise yaw rotations (about the centre of the head)

All sets of MRPs included the ground truth B_1^+ -map at the centred position, and all off-centre positions were the estimated B_1^+ -maps.

MRPs were designed in the small-tip-angle regime using an adapted spatial domain method, and optimised channel weightings via matrix inversion. The phase relaxed magnitude least squares (MLS) optimisation was omitted from the design and candidate spoke selection was optimised to improve magnitude performance, similar to MRPs designed in Chapter 3.2. Pulses were designed in the patient frame, and motion was represented by shifting the gradient fields to match each off-centre position. In the previous MRP design (Chapter 3.2), the top ten spokes locations were tested as each spoke was added, however for this experiment, only the top 5 locations were evaluated. This was because of the higher resolution of the estimated B_1^+ -maps (256x256 voxels) than the previously used B_1^+ -maps (122x151 voxels), and including many more positions in the design (here 23 for set 1). During pulse design the Fourier encoding matrix is multiplied with each RF channel specific B_1^+ -map, as shown in Equation 2.2 (Chapter 2, Section 2.2.1). Increasing the resolution and the number of B_1^+ -maps made the pulse design process more computationally intense and increased computation time, therefore the number of pulses designed was reduced from 10,000 for each slice, to 625. Although $\text{MRPs}_{\text{set-2}}$ and $\text{MRPs}_{\text{set-3}}$ included less positions and could have evaluated more candidate spokes, the number was kept consistent across sets of MRPs so the effect of the number of input B_1^+ -maps could be better determined.

Six equivalent slice-selective 3-spoke reference pulses were designed using only the simulated ground truth B_1^+ -map at the centred position, optimising channel weightings via matrix inversion and phase relaxed MLS, with no spoke placement optimisation. To be consistent with reference pulse design in Chapter 3.2, the Tikhonov regularisation term (β) was kept at 100. Similarly, the MRP used $\beta = 0.1$ and filtered the slice-specific set of 625 MRPs with a tolerance of two times the $\text{SAR}_{10\text{g-avg}}$ of the equivalent slice ref-pulse, at the centred positions. For both reference pulses and MRPs, pulse design parameters were: 60° target flip-angle, 1.5 mm slice thickness, 30 μT peak RF amplitude, 4 μs dwell time, time-bandwidth (TBW) product 4, 80 mT/m maximum gradient amplitude, 200 mT/m/ms maximum gradient slew rate. There was no constraint on pulse length, and MRP and ref-pulse lengths were reported.

Pulses were evaluated using simulated ground truth B_1^+ -maps, and pulse performance was tested similarly to Chapter 3.2. Quantitative and qualitative analysis was performed for magnitude nRMSE and phase RMSE of excitations profiles, the number of positions improved/degraded by the MRPs, and their mean improvement/degradation. Statistical testing in the form of a left-tailed paired t-test, with a 5% significance level ($p \leq 0.05$), was performed for magnitude and phase excitations separately, to determine if the MRPs improvement was statistically significant, on a slice-by-slice basis. All three sets of 6 slice-selective MRPs were evaluated over all 23 simulated ground truth positions, up to the maximums of 20 mm right on-axis, 20 mm right 10 mm posterior off-axis, and 15° yaw rotation. Actual 10-g averaged local SAR ($\text{SAR}_{10\text{g-avg}}$) was calculated for the centre and the 19 off-centre on/off-axis translations in the right-posterior grid, for all three sets of MRPs and the six reference pulses. Yaw SAR data was not included as it was not available from Ref [1]. $\text{SAR}_{10\text{g-avg}}$ sensitivity to motion was investigated for each pulse design and central SAR,

maximum off-centre SAR and the distribution of off-centre $\text{SAR}_{10\text{g-avg}}$ relative to the centre, were compared between designs over all slices.

4.3 Results

4.3.1 $\text{MRP}_{\text{set-1}}$: 23 Design Positions

The slice-wise and position-wise variation in magnitude nRMSE and phase RMSE for the six slice-selective reference pulses, are shown in Figure 4.2. Considering slice-wise magnitude evaluations (Figure 4.2, panel a), ref-pulse nRMSE ranged from 4.1% to 50%, across all positions and slices, with the maximum error occurring at the 15° yaw rotation in one of the middle slices (slice 4). The largest mean nRMSE, averaged across all positions, was 15.2% ($\sigma = 8.3$) for one of the middle slices (slice 3), and the smallest was 10.4% ($\sigma = 3.9$) in the penultimate inferior slice (slice 2).

For slice-wise phase evaluations (Figure 4.2, panel b), ref-pulse RMSE ranged from 0.6° to 71.7° across all positions and slices, with the largest error also occurring at the 15° yaw rotation in slice 4. The largest mean RMSE, averaged across positions was 11.0° ($\sigma = 17.7$) for one of the middle slices (slice 4), and the smallest was 6.3° ($\sigma = 7.2$) in the penultimate inferior slice (slice 2). The ref-pulse for the superior-most slice (slice 6) also had mean RMSE of 6.3° , but had larger variation across positions ($\sigma = 9.7$). Comparing the ranges and interquartile ranges, it is clear there are some positions producing much larger error than most others.

Considering position-wise magnitude error (Figure 4.2, panel c), yaw rotations produced the largest mean nRMSE (29.0%, $\sigma = 13.0$), averaged across all slices, followed by posterior 10 mm off-axis translations (12.3%, $\sigma = 3.5$), posterior 5 mm off-axis translations (10.2%, $\sigma = 3.4$), posterior 2 mm off-axis

translations (9.4%, $\sigma = 3.4$), right on-axis translations (9.2%, $\sigma = 3.4$), posterior on-axis translations (7.7%, $\sigma = 2.0$), then the centres (6.3%, $\sigma = 1.6$).

Considering position-wise phase error (Figure 4.2, panel d), the same trend in error across motion-types was observed. Yaw rotations had the largest mean RMSE across slices (36.3° , $\sigma = 20.8$), followed by posterior 10 mm off-axis translations (5.8° , $\sigma = 2.0$), posterior 5 mm off-axis translations (4.4° , $\sigma = 2.5$), posterior 2 mm off-axis translations (4.1° , $\sigma = 2.6$), right on-axis translations (4.1° , $\sigma = 2.5$), posterior translations (2.7° , $\sigma = 1.9$). Overall, yaw rotations produced the largest errors and are responsible for the large slice-wise ranges in magnitude and phase.

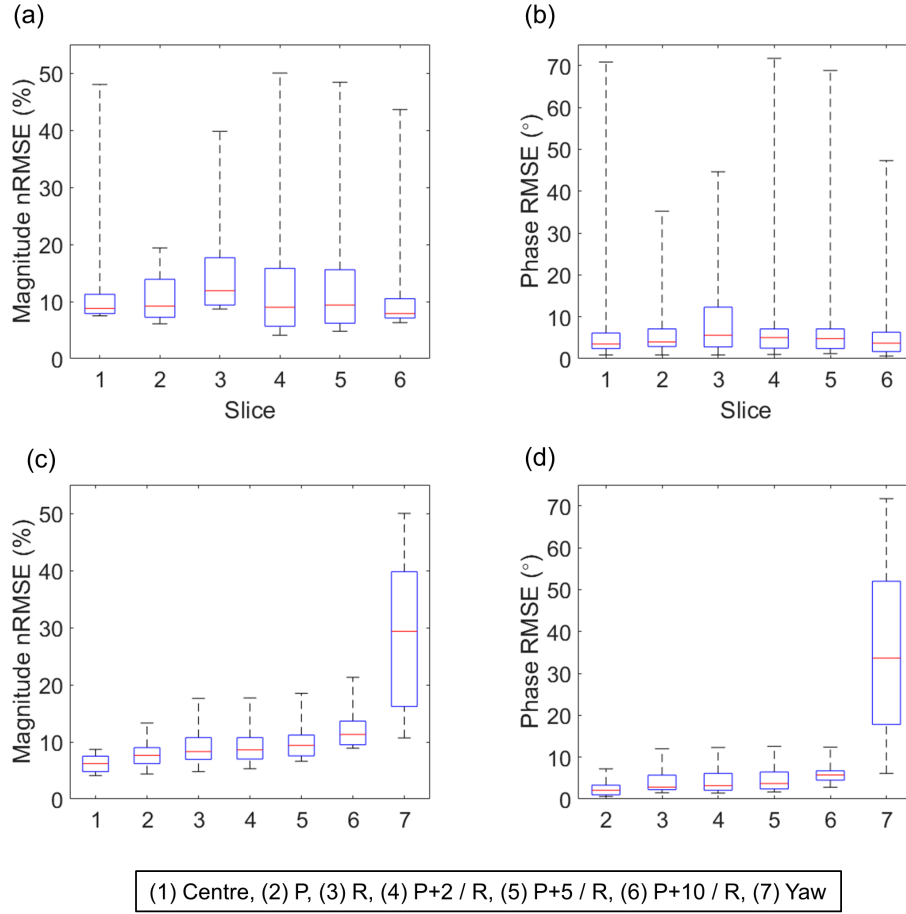


Figure 4.2: Slice-wise magnitude nRMSE (panel a) and phase RMSE (panel b) across all 23 evaluated positions for the six slice-selective reference pulses. Variation in magnitude nRMSE (panel c) and phase RMSE (panel d) is shown for the different motion types (across all slices) including the centre, on-axis posterior translations (P), on-axis right translations (R), 2 mm posterior off-axis (P+2 / R), 5 mm posterior off-axis (P+5 / R), 10 mm posterior off-axis (P+10 / R), and yaw rotations (Yaw). The centred position is not shown in (panel d) because it is the reference for other positions.

Similarly to Figure 4.2, Figure 4.3(panel a, panel b) shows slice-specific MRP magnitude and phase profile errors respectively, over all positions. For $\text{MRPs}_{\text{set-1}}$, all 23 positions were included in the design. Magnitude nRMSE ranged from 4.9% to 18.6% across all design positions and slices, with the maximum error occurring at the 15° yaw rotation in the penultimate inferior slice (slice 2). The largest mean magnitude nRMSE, averaged across all positions for each slice, was 9.5% ($\sigma = 2.4$) for the penultimate inferior slice. The superior-most slice had the smallest mean magnitude nRMSE of 6.9% ($\sigma = 2.1$). Phase RMSE ranged from 0.6° to 18.2° , across all design positions and slices, with the maximum phase error also occurring at the 15° yaw rotation in the penultimate inferior slice (slice 2). The largest mean phase RMSE across positions was 5.7° ($\sigma = 4.3$) for penultimate inferior slice (slice 2), and the smallest was 3.8° ($\sigma = 2.8$) for the superior-most slice (slice 6). These values were similar to the ref-pulse values for slice 2, shown in Figure 4.2(panel a, panel b).

Figure 4.3(panel c, panel d) shows magnitude and phase errors respectively for each motion-type, over all slices. Yaw rotations reported the largest mean magnitude profile nRMSE (11.7%, $\sigma = 2.5$), averaged across all slices, followed by posterior 10 mm off-axis (8.6%, $\sigma = 1.8$), posterior 2 mm off-axis (8.0%, $\sigma = 1.7$), posterior 5 mm off-axis (7.7%, $\sigma = 1.8$), right on-axis (8.4%, $\sigma = 1.7$), posterior on-axis (7.2%, $\sigma = 1.0$). The on-axis posterior translations reported a lower mean nRMSE across slices than the centred positions (7.5%, $\sigma = 1.0$). For mean phase profile RMSE, again yaw rotations had the largest error (11.4° , $\sigma = 3.2$), followed by posterior 10 mm off-axis (4.7° , $\sigma = 1.9$), posterior 5 mm off-axis (3.8° , $\sigma = 1.9$), posterior 2 mm off-axis (3.6° , $\sigma = 1.9$), right on-axis (3.6° , $\sigma = 1.8$) and posterior on-axis (1.9° , $\sigma = 1.1$).

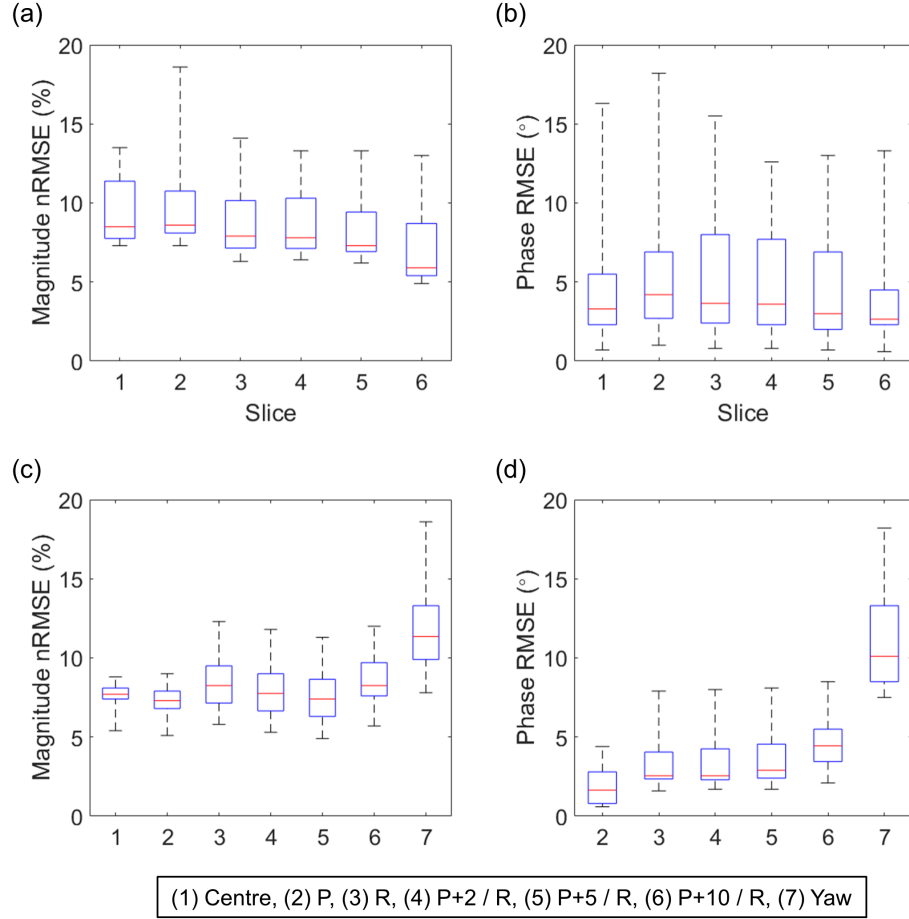


Figure 4.3: Slice-wise magnitude nRMSE (panel a) and phase RMSE (panel b) across all 23 evaluated positions for the six slice-selective MRPs included in set 1 (all 23 positions included in design). Variation in magnitude nRMSE (panel c) and phase RMSE (panel d) is shown for the different motion types (across all slices) including the centre, on-axis posterior translations (P), on-axis right translations (R), 2 mm posterior off-axis (P+2 / R), 5 mm posterior off-axis (P+5 / R), 10 mm posterior off-axis (P+10 / R), and yaw rotations (Yaw). The centred position is not shown in (panel d) because it is the reference for other positions.

The 138 magnitude nRMSE evaluations, considering all slices, are displayed in Figure 4.4 (panel a). It is immediately clear that rotations in yaw (5° , 10° , and 15°) produced the largest errors for the reference pulses. These were the positions that were improved the most by the MRP design, with large reductions in magnitude nRMSE and phase RMSE. Considering all slices, the MRPs improved 106/138 (77%) magnitude evaluations, with a mean reduction in nRMSE of 5.3% ($\sigma = 7.8$), from 13.0% ($\sigma = 8.8$) to 8.5% ($\sigma = 2.4$). The remaining 23% of positions were degraded, with a mean increase in nRMSE of 1.4% ($\sigma = 1.1$), from 6.7% ($\sigma = 1.7$) to 8.1% ($\sigma = 1.3$). The MRPs reduced the largest reference pulse magnitude nRMSE from 50% to 13%. MRPs magnitude profile nRMSE at the centred positions ranged from 5.4% to 8.8%, and a mean of 7.5% ($\sigma = 1.0$) across slices. For reference pulses, magnitude nRMSE at the centred position ranged between 4.1% and 8.7%. The MRPs reported lower magnitude nRMSE than reference pulses at the centred position in three slices.

The 132 phase RMSE evaluations (centre omitted for phase), considering all slices, are displayed in Figure 4.4 (panel b). MRPs improved 94/132 (71%) evaluations, with a mean reduction in RMSE of 5.9° ($\sigma = 12.8$), from 10.7° ($\sigma = 15.7$) to 4.8° ($\sigma = 3.7$). The remaining 29% saw a mean increase in RMSE of 0.8° ($\sigma = 1.2$), from 3.5° ($\sigma = 2.0$) to 4.3° ($\sigma = 2.7$). The MRPs reduced the largest reference pulse phase RMSE from 72° to 13° . The mean improvement in magnitude nRMSE and phase RMSE were almost four-fold and five-fold greater than the mean degradation, however the standard deviation of improvement was much larger. This is due to some positions (yaw) seeing much larger improvement than other motion types.

The slice-specific number of positions improved or degraded and mean improvement or degradation is shown in Table 4.1 for magnitude evaluations, and Table 4.2 for phase evaluations. For every slice, the MRPs improved more po-

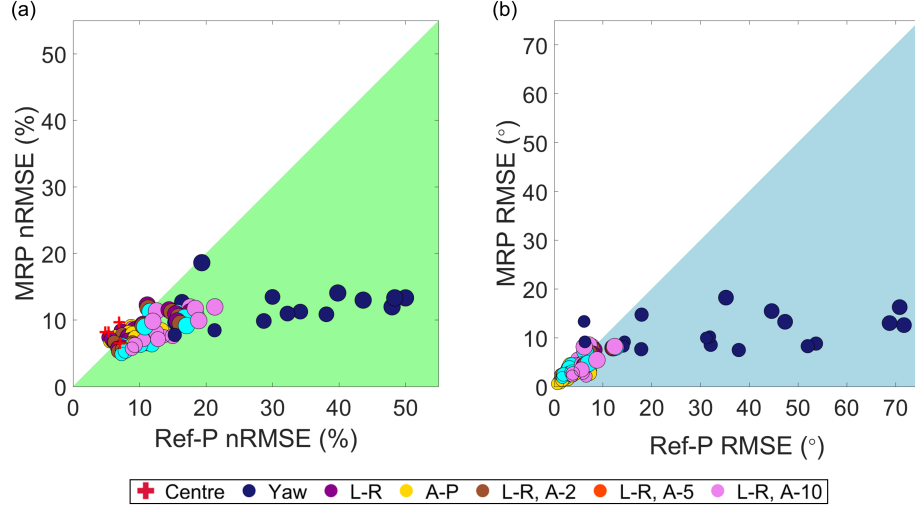


Figure 4.4: (panel a) Magnitude nRMSE (%) and (panel b) phase RMSE (°) of $\text{MRPs}_{\text{set-1}}$ (23 design positions) vs reference pulses (Ref-Ps) including all 23 magnitude and 22 phase evaluations, for each of the six slices. Green and blue regions show positions improved by the MRP and marker size represents the extent of the displacement, up to 20 mm right, 10 mm posterior, 15° rotation and 20 mm right 10 mm posterior off-axis

sitions than they degraded. For magnitude evaluations, the MRPs improved all positions (including the centre) for one of the middle slices (slice 3) and the superior-most slice (slice 6), reducing mean nRMSE across positions from 15.2% ($\sigma = 8.5$) to 8.6% ($\sigma = 2.1$) and 11.0% ($\sigma = 8.5$) to 6.9% ($\sigma = 2.1$), respectively. The remaining four slices all improved 15/23 (65%) of evaluations and degraded 8/23 (35%). One of the middle slices (slice 4) had the largest mean increase in nRMSE for degraded positions, increasing error from 5.3% ($\sigma = 0.8$) to 7.3% ($\sigma = 0.5$); but a much larger mean reduction in nRMSE for improved positions, reducing error from 16.2% ($\sigma = 11.5$) to 9.2% ($\sigma = 2.1$). Although magnitude nRMSE was degraded at 35% of positions in four of the slices, the mean improvement in 65% of evaluations was up to 7-fold higher than the mean degradation.

Slice	Magnitude					
	Positions Improved	Positions Degraded	Mean Improvement (%)	σ	Mean Degradation (%)	σ
1	15	8	4.0	9.8	0.5	0.3
2	15	8	2.3	1.6	1.6	0.9
3	23	0	6.6	6.9	0	0
4	15	8	7.0	9.8	2.1	1.2
5	15	8	7.6	9.1	1.5	1.1
6	23	0	4.1	6.9	0	0

Table 4.1: The number of magnitude evaluations (positions) improved/degraded by $\text{MRPs}_{\text{set-1}}$ (all 23 positions included in design) and the mean reduction/increase in magnitude nRMSE (%). The slice 3 and slice 6 MRPs reduced magnitude nRMSE in all positions (including the centre).

Slice	Phase					
	Positions Improved	Positions Degraded	Mean Improvement ($^{\circ}$)	σ	Mean Degradation ($^{\circ}$)	σ
1	16	6	6.1	14.9	0.5	0.4
2	12	10	2.0	4.8	1.1	2.2
3	20	2	4.6	7.7	0.6	0.1
4	15	7	9.3	18.3	0.7	0.5
5	16	6	8.7	17.0	0.6	0.8
6	15	7	4.1	8.6	0.9	0.9

Table 4.2: The number of phase evaluations (positions) improved/degraded by $\text{MRPs}_{\text{set-1}}$ (all 23 positions included in the design) and the mean reduction/increase in phase RMSE ($^{\circ}$). The MRPs improved the most positions in slice 3, and the least in slice 2. The slice 2 MRP improved 12/22 positions, however its mean improvement was 82% greater than its mean degradation.

For phase evaluations, one of the middle slices (slice 3) saw the most positions improved (20/22), and the penultimate inferior slice (slice 2) saw the least (12/22). Again, even though slice 2 had the most degraded positions, the mean reduction in RMSE from 8.4° ($\sigma = 9.4$) to 6.3° ($\sigma = 5.1$), was 1.8-fold larger than the mean increase in RMSE. One of the middle slices (slices 4) and the penultimate superior slice (slice 5) reported large standard deviations ($\sigma = 12.2$ and $\sigma = 11.5$, respectively), indicating some positions saw much larger improvement than others. This was also seen in Figure 4.4, for 10° and 20° yaw rotations.

Figure 4.5 shows the centred and off-centre excitations, with difference profiles showing the absolute difference between the off-centre and centred position excitations, for the position most improved by $\text{MRPs}_{\text{set-1}}$, for each slice. The 15° yaw rotation was the most improved position in every slice, with MRPs reducing magnitude nRMSE at this position by up to 36.7%, from 50.0% to 13.3% in one of the middle slices (slice 4). The MRPs reduced phase RMSE by up to 59.1° , from 71.7° to 12.6° in one of the middle slices (also slice 4). The MRPs were able to reduce very large errors in both magnitude and phase evaluations and maintain far better quality excitations for the large rotations, although the penultimate inferior slice (slice 2) MRP experienced an area of large error near the left ear.

Considering magnitude nRMSE, MRPs improved performance significantly in all slices ($p \leq 0.05$) except in the inferior-most slice (slice 1), which performed similarly to the reference pulses ($p = 0.08$). For phase RMSE, MRPs improved performance significantly in all slices ($p \leq 0.05$), except in the penultimate inferior slice (slice 2) which performed similarly to the reference pulses ($p = 0.25$). As Table 4.2 shows, the MRP for the penultimate inferior slice (slice 2) still improved the majority of phase evaluations, with a larger mean reduction in RMSE than mean increase. Looking at Figure 4.4, there were no wildly degraded phase positions, all increases in phase RMSE were relatively small, especially compared to the reductions in phase RMSE.

The slice-specific reference RF pulse lengths were all 4.0 ms. MRP pulse lengths varied across slices due to a scaling of the dwell time to satisfy a maximum B_1^+ constraint. MRP pulse lengths ranged between 7.1 ms and 10.4 ms across slices. The percentage increase in pulse length between MRPs and reference pulses, averaged across all slices, was 105%.

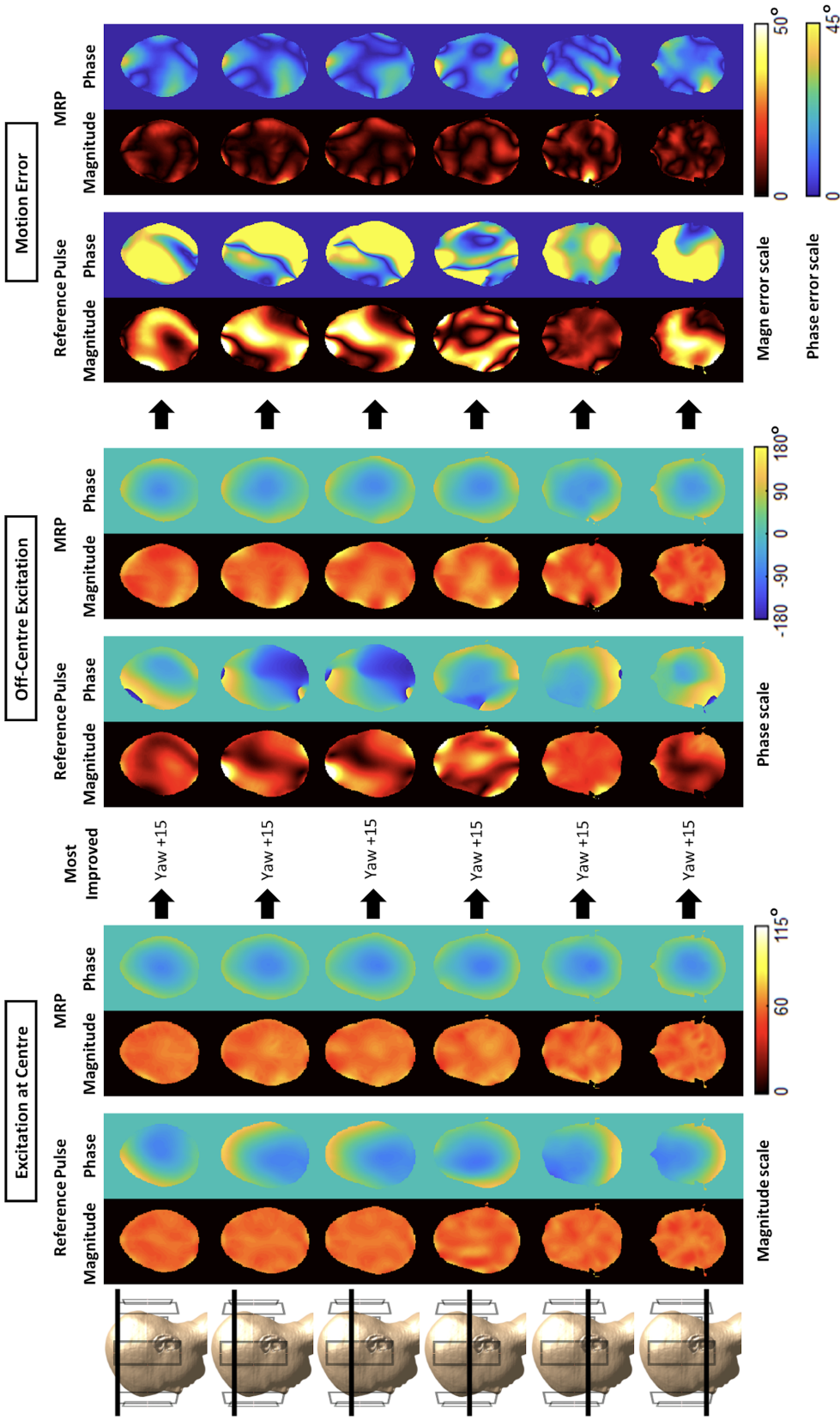


Figure 4.5: The magnitude and phase excitations at the centred positions, most improved off-centre excitations, and difference profiles. For slices 1 to 6, $\text{MRP}_{\text{set-1}}$ reduced ref-pulse magnitude nRMSE from 48.0% to 12.0%, 19.4% to 18.6%, 39.8% to 14.0%, 50.0% to 13.3%, 48.4% to 13.3%, and 43.6% to 13.0% respectively. For phase, the MRPs reduced ref-pulse RMSE from 70.8° to 16.3°, 35.2° to 18.2°, 44.6° to 15.5°, 71.7° to 12.6°, 68.8° to 13.0°, and 47.3° to 13.3°, for slices 1 to 6 respectively. The +15° yaw rotation was the most improved position for all slices. Where motion error is shown as zero, this is where the pulses achieved the target flip angle (magnitude), or achieved consistent phase with the centred position.

4.3.2 MRP_{set-2}: 18 Design Positions

Identical analysis to MRP_{set-1} were performed to the subsequent sets of MRPs. Slice-wise and position-wise variation across all magnitude nRMSE and phase RMSE evaluations for MRP_{set-1} (18 design positions) are shown in Figure 4.6. Slice-specific MRP magnitude and phase profile errors, over all positions, are shown in Figure 4.6(panel a, panel b) respectively. Magnitude nRMSE ranged from 4.7% to 25.4% across all design positions and slices, with the maximum error occurring at the 15° yaw rotation in the penultimate inferior slice (slice 2). The largest mean magnitude nRMSE, averaged across all positions for each slice, was 9.8% ($\sigma = 4.2$) for the penultimate inferior slice. The superior-most slice had the smallest mean magnitude nRMSE of 6.8% ($\sigma = 1.9$). Phase RMSE ranged from 0.7° to 24.2°, across all design positions and slices, with the maximum phase error also occurring at the 15° yaw rotation in the penultimate superior slice (slice 5). The largest mean phase RMSE across positions was 6.1° ($\sigma = 4.1$) for the penultimate inferior slice (slice 2), and the smallest was 4.4° ($\sigma = 3.6$) for the inferior-most slice (slice 1). The superior-most slice (slice 6) reported the same mean phase RMSE as the inferior-most slice but with larger variation in error across positions.

Figure 4.6(panel c, panel d) show magnitude nRMSE and phase RMSE variation across motion types. Averaged across all slices, yaw rotations had the largest mean nRMSE (13%, $\sigma = 4.6$), followed by posterior 10 mm off-axis translations (8.7%, $\sigma = 2.4$), right on-axis (8.4%, $\sigma = 2.6$), posterior 2 mm off-axis (7.8%, $\sigma = 2.6$), posterior 5 mm off-axis (7.5%, $\sigma = 2.5$), posterior on-axis (6.6%, $\sigma = 1.0$), then the centres (6.7%, $\sigma = 0.9$). The non-linearity in MRPs error across motion types, i.e. why posterior 2 mm off-axis reports larger mean error than posterior 5 mm off-axis, is discussed in Section 4.4. For mean phase RMSE, yaw rotations reported largest mean RMSE across slices (13.1°,

$\sigma = 4.7$), followed by posterior 10 mm off-axis (5.5° , $\sigma = 2.1$), posterior 5 mm off-axis (4.2° , $\sigma = 2.4$), posterior 2 mm off-axis (3.8° , $\sigma = 2.4$) and right on-axis (3.8° , $\sigma = 2.3$), then posterior on-axis (2.2° , $\sigma = 1.4$).

Figure 4.7 shows all magnitude nRMSE (panel a) and phase RMSE (panel b) evaluations over all slices for the MRPs against the ref-pulses. The MRPs improved 116/138 (84%) of magnitude evaluations, with a mean reduction in nRMSE of 4.7% ($\sigma = 6.9$), from 13.1% ($\sigma = 9.1$) to 8.5% ($\sigma = 3.1$). The remaining 16% of positions were degraded, with a mean increase in nRMSE of 1.2% ($\sigma = 1.3$), from 7.3% ($\sigma = 3.6$) to 8.6% ($\sigma = 4.3$). Mean magnitude nRMSE reduction/improvement for the 84% of positions was approximately 3-fold greater than the mean increase/degradation in nRMSE. MRP magnitude nRMSE at the centred positions ranged between 5.4% and 7.9% and reported lower error than the reference pulses in the inferior-most slice (slice 1), one of the middle slices (slice 3), and the superior-most slice (slice 6), similar to $\text{MRPs}_{\text{set-1}}$. For phase RMSE, the MRPs improved 86/132 (65%) of positions, with a mean reduction in RMSE of 5.7° ($\sigma = 12.4$), from 11.2° ($\sigma = 16.3$) to 5.5° ($\sigma = 4.8$). The remaining 35% of positions were degraded, with a mean increase in RMSE of 0.8° ($\sigma = 1.2$), from 4.0° ($\sigma = 2.2$) to 4.8° ($\sigma = 2.9$). The mean RMSE reduction for 65% of positions improved was about 6-fold greater than the mean increase in RMSE in the 35% of positions degraded. The MRPs reduced the largest reference pulse magnitude nRMSE (50%) and phase RMSE (72°), to 18.0% and 13.7° , respectively.

The number of positions improved or degraded and mean improvement or degradation over positions, for slice-specific MRP magnitude and phase evaluations, are shown in Tables 4.3 and 4.4 respectively. Again, at no point did the MRPs degrade more positions than they improved for magnitude evaluations. The MRPs improved all positions (including the centre) in one of the

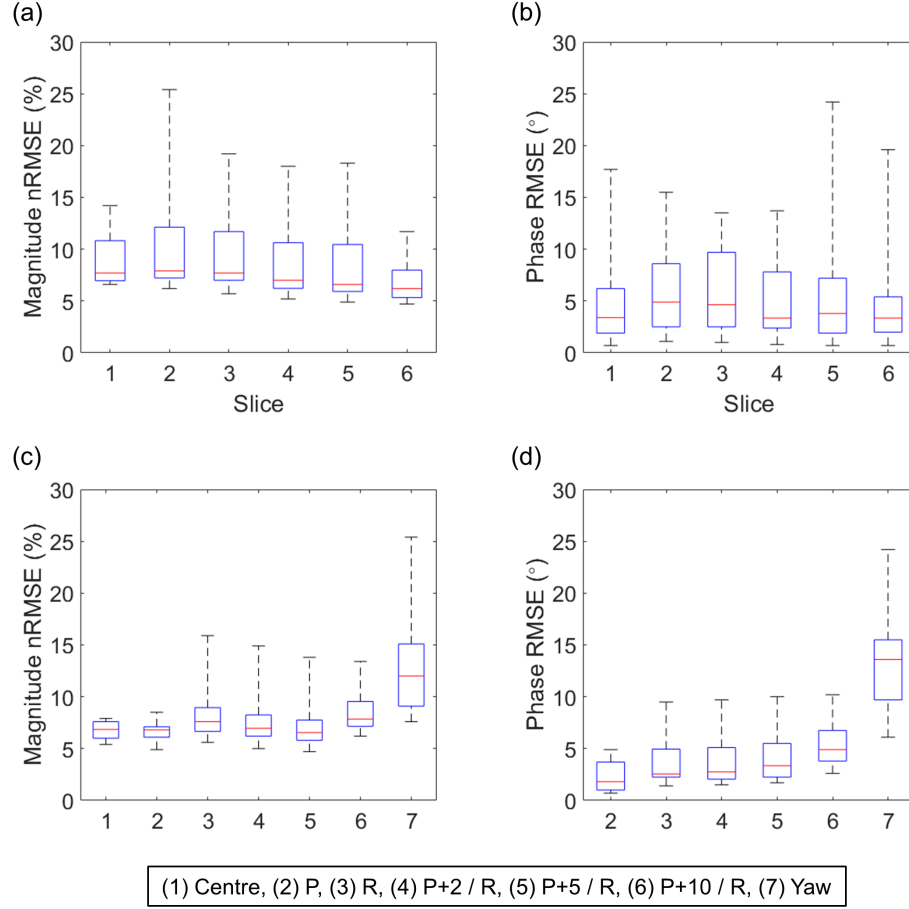


Figure 4.6: Slice-wise magnitude nRMSE (panel a) and phase RMSE (panel b) across all 23 evaluated positions for the six slice-selective MRPs in set 2 (18 design positions). Variation in magnitude nRMSE (panel c) and phase RMSE (panel d) is shown for the different motion types (across all slices) including the centre, on-axis posterior translations (P), on-axis right translations (R), 2 mm posterior off-axis (P+2 / R), 5 mm posterior off-axis (P+5 / R), 10 mm posterior off-axis (P+10 / R), and yaw rotations (Yaw). The centred position is not shown in (panel d) because it is the reference for other positions.

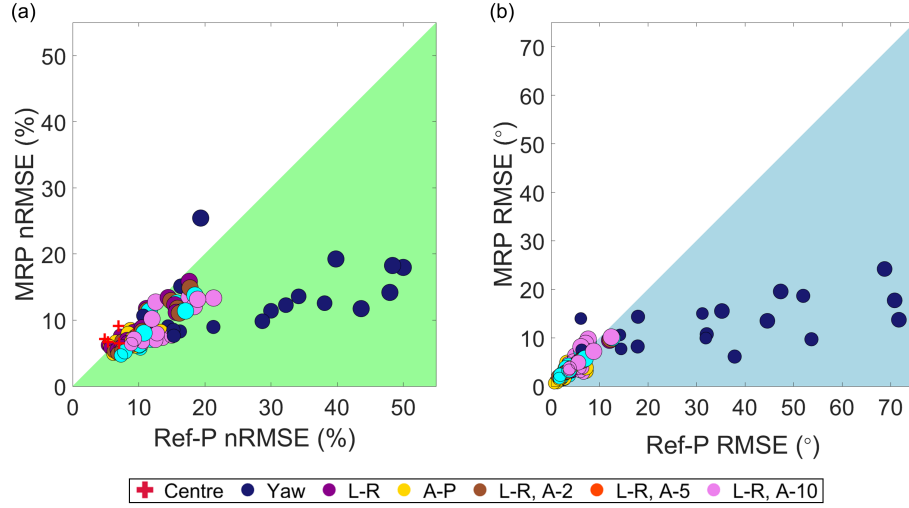


Figure 4.7: (panel a) Magnitude nRMSE (%) and (panel b) phase RMSE (°) of MRPs_{set-2} (18 design positions) vs reference pulses (Ref-Ps) including all 23 magnitude and 22 phase evaluations, for each of the six slices. Green and blue regions show positions improved by the MRP and marker size represents the extent of the displacement, up to 20 mm right, 10 mm posterior, 15° rotation and 20 mm right 10 mm posterior off-axis

middle slices (slice 3) and the superior-most slice (slice 6), reducing nRMSE from 15.2% ($\sigma = 8.5$) to 9.3% ($\sigma = 3.7$), and 11.0% ($\sigma = 8.5$) to 6.8% ($\sigma = 1.9$), respectively. The penultimate inferior slice (slice 2) had the most positions degraded by the MRP (8/23), increasing mean nRMSE (averaged across degraded positions) from 8.7% ($\sigma = 4.5$) to 10.4% ($\sigma = 6.2$); however the majority of positions were improved, with a larger mean reduction in nRMSE, from 11.4% ($\sigma = 3.5$) to 9.4% ($\sigma = 3.1$).

For phase evaluations, one of the middle slices (slice 3) had the most positions improved by the MRP (18/22), reducing mean RMSE from 10.7° ($\sigma = 10.9$) to 6.6° ($\sigma = 3.5$). The remaining 4 degraded positions performed similarly to the equivalent reference pulse, increasing mean RMSE (averaged across degraded positions) from 1.7° ($\sigma = 0.6$) to 2.0° ($\sigma = 0.6$). The penultimate inferior slice (slice 2) was the most degraded slice for phase, where RMSE increased in 14/22

Slice	Magnitude					
	Positions Improved	Positions Degraded	Mean Improvement (%)	σ	Mean Degradation (%)	σ
1	20	3	3.5	8.2	0.3	0.2
2	15	8	1.9	1.3	1.7	1.9
3	23	0	5.9	6.0	0	0
4	17	6	6.1	8.1	1.6	0.8
5	18	5	5.9	7.4	0.7	0.6
6	23	0	4.2	7.1	0	0

Table 4.3: The number of magnitude evaluations (positions) improved/degraded by $\text{MRPs}_{\text{set-2}}$ (18 design positions) and the mean reduction/increase in magnitude nRMSE (%). The slice 3 and slice 6 MRPs reduced magnitude nRMSE in all positions (including the centre), similar to $\text{MRPs}_{\text{set-1}}$.

Slice	Phase					
	Positions Improved	Positions Degraded	Mean Improvement ($^{\circ}$)	σ	Mean Degradation ($^{\circ}$)	σ
1	15	7	6.6	15.2	0.6	0.4
2	8	14	3.2	6.8	1.5	1.9
3	18	4	4.1	8.3	0.3	0.1
4	13	9	10.7	19.0	0.6	0.6
5	17	5	6.4	13.0	0.8	0.8
6	15	7	3.0	7.3	0.4	0.4

Table 4.4: The number of phase evaluations (positions) improved/degraded by $\text{MRPs}_{\text{set-2}}$ (18 design positions) and the mean reduction/increase in phase RMSE ($^{\circ}$). The MRPs improved the most positions in slice 3, and the least in slice 2. The slice 2 MRP improved 8/22 positions, however its mean improvement was 113% greater than its mean degradation.

(64%) of positions, from a mean RMSE of 4.8° ($\sigma = 2.1$) to 6.3° ($\sigma = 3.3$). The remaining positions were improved, reducing mean RMSE from 8.9° ($\sigma = 11.9$) to 5.7° ($\sigma = 5.7$). The penultimate inferior slice was the only slice where the MRP degraded more positions than it improved.

Figure 4.8 shows the excitations at the centred and off-centre positions, with difference profiles showing the absolute difference between the off-centre and centred position excitations, for the position most improved by $\text{MRPs}_{\text{set-2}}$, for each slice. Similar to $\text{MRPs}_{\text{set-1}}$, the 15° yaw rotation was the most improved position in every slice, with MRPs reducing nRMSE at this position by up to

33.8% from 48% to 14.2% in the inferior-most slice (slice 1). The penultimate inferior slice (slice 2) reported an increase in magnitude nRMSE from 19.4% to 25.4%. This is likely due to the fact that the most improved position was determined by the mean of the magnitude and phase profile error, and referring back to Table 4.4, most phase evaluations in slice 2 were degraded, which could have dominated the selection of the most improved position in this slice.

The MRPs reduced phase RMSE by up to 58° , from 71.7° to 13.7° in one of the middle slices (slice 4). $\text{MRPs}_{\text{set-2}}$ were able to reduce very large errors in both magnitude and phase evaluations, however did not perform as well as $\text{MRPs}_{\text{set-1}}$. This was expected, as the largest displacements were included in $\text{MRPs}_{\text{set-1}}$ design, but not for $\text{MRPs}_{\text{set-2}}$, however were included in testing. Even though the 15° positions were not included in $\text{MRPs}_{\text{set-2}}$ design, they were still the most improved positions by the MRPs. This shows MRPs are capable of also improving positions outside of those used in the design.

Considering magnitude nRMSE, MRPs improved performance significantly in all slices ($p \leq 0.05$), except for the penultimate inferior slice (slice 2) which performed similarly, with $p = 0.09$. Considering phase RMSE, MRPs improved performance significantly in the middle and superior slices (slices 3 to 6), with $p \leq 0.05$, and similarly in the inferior slices (slices 1 and 2), with $p = 0.07$ and $p = 0.42$, respectively.

The slice-specific reference RF pulse lengths were all 4.0 ms. MRP pulse lengths ranged between 7.1 ms and 11.1 ms. The percentage increase in pulse length between MRPs and reference pulses, averaged across all slices, was 108%, comparable to $\text{MRPs}_{\text{set-1}}$.

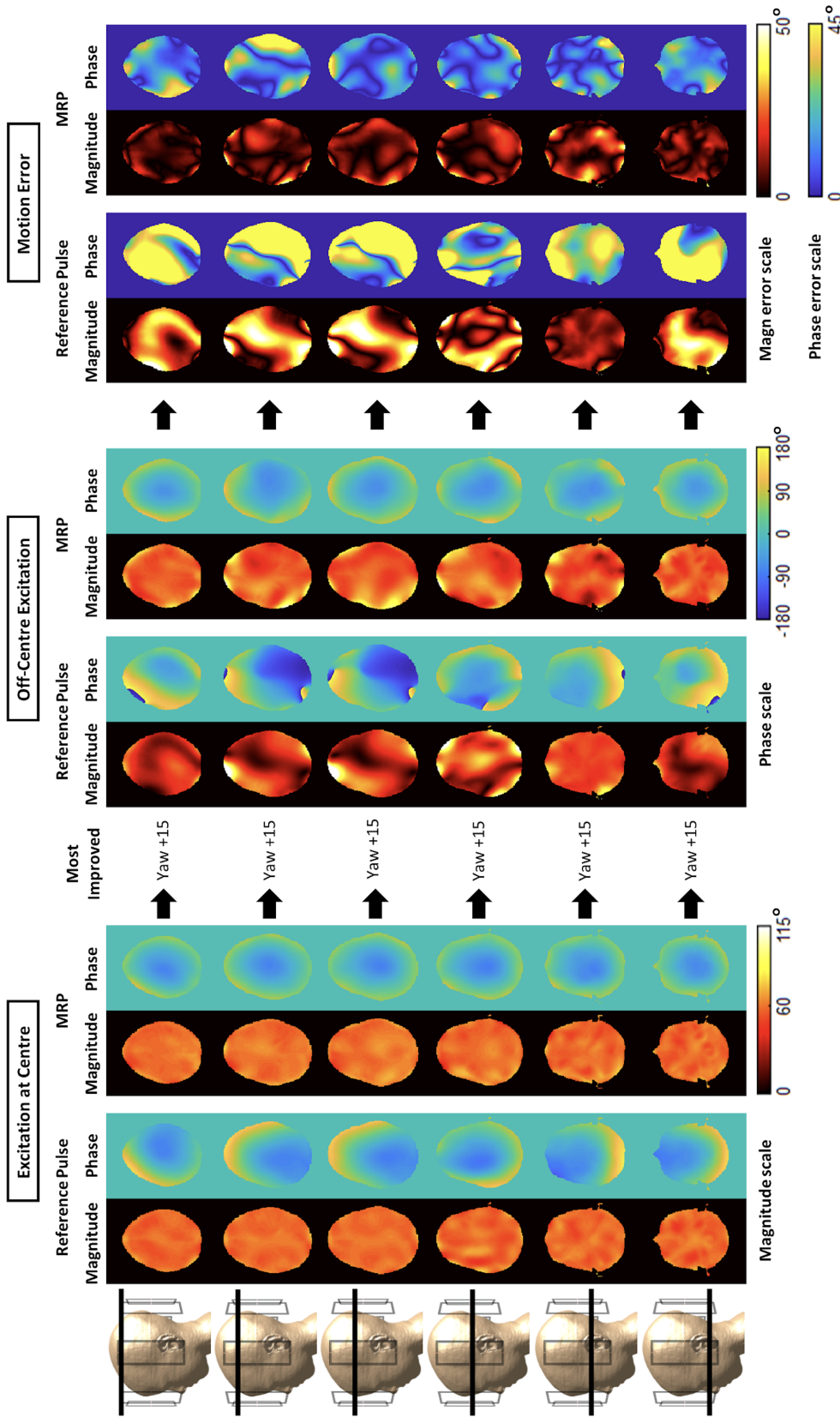


Figure 4.8: The magnitude and phase excitations at the centred positions, most improved off-centre excitations, and absolute difference profiles. For slices 1 to 6, $\text{MRP}_{\text{set-2}}$ reduced ref-pulse magnitude nRMSE from 48.0% to 19.2%, 50.0% to 18.0%, 48.4% to 18.3%, 43.6% to 11.7% for slices 1 and 3 to 6 respectively. Slice 2 reported an increase in magnitude nRMSE from 19.4% to 25.4%. For phase, the MRPs reduced ref-pulse RMSE from 70.8° to 17.7°, 35.2° to 15.5°, 44.6° to 13.5°, 71.7° to 13.7°, 68.8° to 24.2° and 47.3° to 19.6° for slices 1 to 6 respectively. The +15° yaw rotation was the most improved position for all slices, despite not being included in the $\text{MRP}_{\text{set-2}}$ design. Where motion error is shown as zero, this is where the pulses achieved the target flip angle (magnitude), or achieved consistent phase with the centred position.

4.3.3 MRPs_{set-3}: 10 Design Positions

The slice-wise and motion-wise magnitude nRMSE and phase RMSE variation across the design positions for MRPs_{set-3} (10 design positions), are shown in Figure 4.9. Slice-specific MRP magnitude and phase profile errors, over all positions, are shown in Figure 4.9(panel a, panel b) respectively. Magnitude nRMSE ranged from 4.1% and 30.1% across slices and design positions, with the maximum magnitude profile nRMSE occurring at the 15° yaw rotation in the penultimate inferior slice (slice 2). The largest mean nRMSE, averaged across all positions, was 10.6% ($\sigma = 5.9$) for one of the middle slices (slice 3). The smallest mean nRMSE was 7.6% ($\sigma = 4.3$), reported for the superior-most slice (slice 6).

Phase RMSE ranged from 0.8° to 29.8°, with the maximum phase profile RMSE also occurring at the 15° yaw rotation, but in penultimate superior slice (slice 5). The largest mean RMSE, averaged across all positions, was 6.3° ($\sigma = 4.6$) for the penultimate inferior slice (slice 2), and the smallest was 4.6° ($\sigma = 4.2$) for the inferior-most slice (slice 1).

Figure 4.9(panel c, panel d) shows the magnitude nRMSE and phase RMSE variations of the different motion types across all slices, respectively. Similar to MRPs_{set-1} and MRPs_{set-2}, yaw rotations had the largest mean profile nRMSE (16.8%, $\sigma = 7.7$). Followed by posterior 10 mm off-axis translations (10.3%, $\sigma = 3.5$), right on-axis (8.1%, $\sigma = 3.5$), posterior 5 mm off-axis (7.9%, $\sigma = 3.6$), posterior 2 mm off-axis (7.8%, $\sigma = 3.6$), posterior on-axis (6.1%, $\sigma = 1.4$), and the centres (5.5%, $\sigma = 0.7$). The trend in mean phase RMSE across motion types was different to mean magnitude nRMSE, yaw rotations had the largest mean RMSE (13.9°, $\sigma = 7.4$), then posterior 10 mm off-axis (5.3°, $\sigma = 2.0$), posterior 5 mm off-axis (4.3°, $\sigma = 2.2$), posterior 2 mm off-axis (3.9°, $\sigma = 2.2$) and right on-axis (3.9°, $\sigma = 2.1$), then posterior on-axis (2.2°, $\sigma = 1.3$).

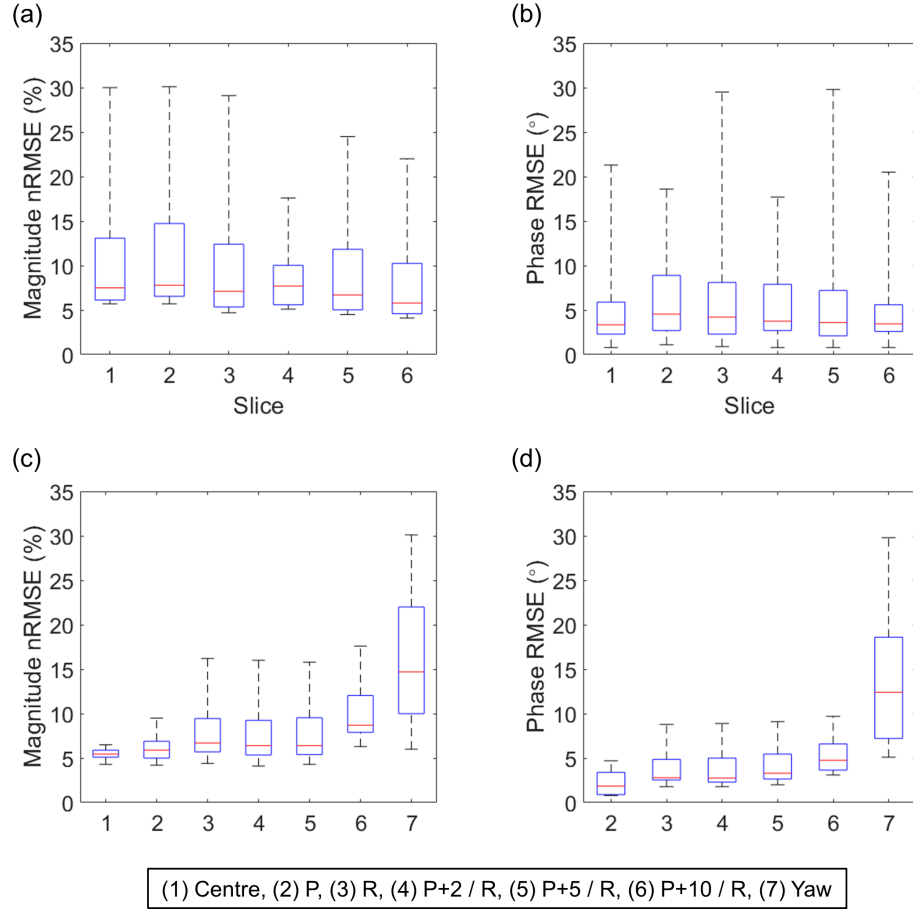


Figure 4.9: Slice-wise magnitude nRMSE (panel a) and phase RMSE (panel b) across all 23 evaluated positions for the six slice-selective MRPs in set 3 (10 design positions). Variation in magnitude nRMSE (panel c) and phase RMSE (panel d) is shown for the different motion types (across all slices) including the centre, on-axis posterior translations (P), on-axis right translations (R), 2 mm posterior off-axis (P+2 / R), 5 mm posterior off-axis (P+5 / R), 10 mm posterior off-axis (P+10 / R), and yaw rotations (Yaw). The centred position is not shown in (panel d) because it is the reference for other positions.

Figure 4.10 shows all 138 magnitude nRMSE (panel a) and 132 phase RMSE (panel b) evaluations considering all slice-selective MRPs and ref-pulses. For magnitude nRMSE, the MRPs improved 110/138 (80%) of evaluations, with a mean reduction in nRMSE of 4.2% ($\sigma = 5.6$), from 12.9% ($\sigma = 9.4$) to 8.7% ($\sigma = 5.0$). The MRP increased nRMSE in the remaining 20% of positions by a mean of 1.5% ($\sigma = 2.2$), from 9.6% ($\sigma = 4.2$) to 11.0% ($\sigma = 5.8$). Mean magnitude nRMSE reduction/improvement for the 80% of positions was approximately 2-fold greater than the mean increase/degradation in nRMSE. MRP magnitude nRMSE at the centred position ranged between 4.3% and 6.5% and reported lower error than the reference pulses in the inferior-most and superior-most slices (slices 1 and 6), and one of the middle slices (slice 3). This was similar to $\text{MRPs}_{\text{set-1}}$ and $\text{MRPs}_{\text{set-2}}$. For phase RMSE, the MRPs improved 78/132 (59%) of positions, with a mean reduction in RMSE of 6.2° ($\sigma = 12.3$), from 12.1° ($\sigma = 16.9$) to 5.9° ($\sigma = 5.8$). The remaining 41% of positions were degraded, with MRPs increasing RMSE by a mean of 0.8° ($\sigma = 1.2$), from 3.7° ($\sigma = 2.1$) to 4.5° ($\sigma = 2.8$). The mean RMSE reduction/improvement in 59% of positions was approximately 7-fold greater than the mean RMSE increase/degradation in the 41% of positions improved. The MRPs reduced the largest reference pulse magnitude nRMSE (50%) and phase RMSE (72°), to 13.9% and 17.7° , respectively.

Slice-specific MRP number of positions improved/degraded and mean improvement/degradation in magnitude nRMSE and phase RMSE evaluations are shown in Table 4.5 and Table 4.6, respectively. Similar to the $\text{MRPs}_{\text{set-1}}$ and $\text{MRPs}_{\text{set-2}}$, at no point did the MRPs degrade more magnitude evaluations than they improved. This time the MRPs only improved all positions (including the centre) in one of the middle slices (slice 3), reducing mean nRMSE (averaged across positions) from 15.2% ($\sigma = 8.5$) to 9.4% ($\sigma = 6.0$). Similar to previous

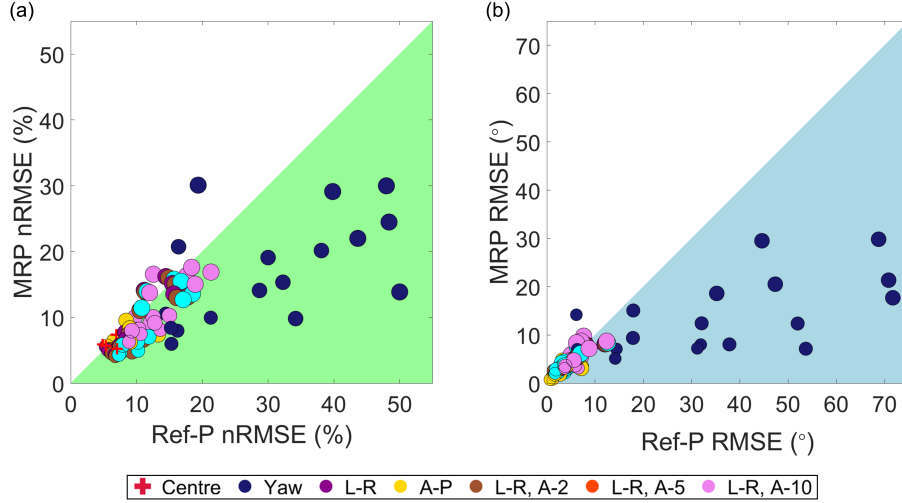


Figure 4.10: (panel a) Magnitude nRMSE (%) and (panel b) phase RMSE ($^{\circ}$) of $\text{MRPs}_{\text{set-3}}$ (10 design positions) vs reference pulses (Ref-Ps) including all 23 magnitude and 22 phase evaluations, for each of the six slices. Green and blue regions show positions improved by the MRP and marker size represents the extent of the displacement, up to 20 mm right, 10 mm posterior, 15° rotation and 20 mm right 10 mm posterior off-axis

MRP sets, the penultimate inferior slice (slice 2) had the most degraded magnitude evaluations (11/23, 48%), increasing mean nRMSE from 11.6% ($\sigma = 4.7$) to 13.6% ($\sigma = 7.2$). The majority of slice 2 magnitude profiles were still improved (12/23, 52%), reducing mean nRMSE from 9.3% ($\sigma = 3.1$) to 7.8% ($\sigma = 2.9$).

For phase evaluations, similar to previous MRP sets, the MRP for one of the middle slices (slice 3) improved the most positions (19/22, 86%), reducing mean RMSE of from 10.3° ($\sigma = 10.8$) to 6.4° ($\sigma = 6.2$). The remaining 14% of positions performed similarly to the equivalent reference pulse, with the MRP increasing mean phase RMSE from 1.6° ($\sigma = 0.6$) to 1.7° ($\sigma = 0.6$). The MRPs for the penultimate inferior slice (slice 2) and the superior-most slice (slice 6) degraded more positions than they improved, however degraded positions still performed similarly to the equivalent reference pulses. For the penultimate inferior slice, the MRP increased RMSE in 15/22 (68%) from 4.7° ($\sigma = 2.1$)

Slice	Magnitude					
	Positions Improved	Positions Degraded	Mean Improvement (%)	σ	Mean Degradation (%)	σ
1	18	5	3.0	4.4	2.4	1.4
2	12	11	1.5	1.0	1.9	3.2
3	23	0	5.7	3.3	0	0
4	17	6	5.1	9.9	0.6	0.5
5	21	2	4.3	5.6	0.3	0.0
6	19	4	4.3	5.3	0.9	0.6

Table 4.5: The number of magnitude evaluations (positions) improved/degraded by $\text{MRPs}_{\text{set-3}}$ (10 design positions) and the mean reduction/increase in magnitude nRMSE (%). The slice 3 MRP reduced magnitude nRMSE in all positions (including the centre). $\text{MRPs}_{\text{set-3}}$ did not improve all magnitude evaluations in the superior-most slice (slice 6) like in $\text{MRPs}_{\text{set-1}}$ and $\text{MRPs}_{\text{set-2}}$.

to 6.0° ($\sigma = 3.5$); and reduced RMSE in 7/22 (32%) from 9.8° ($\sigma = 12.5$) to 6.8° ($\sigma = 6.9$). For the superior-most slice, the MRP increased RMSE in 12/22 (55%) from 2.4° ($\sigma = 1.5$) to 2.9° ($\sigma = 1.5$); and reduced RMSE in 10/22 (45%) from 11.1° ($\sigma = 13.4$) to 6.9° ($\sigma = 5.1$). For both slices, the reduction in error in improved evaluations was larger than the increase in error in degraded evaluations.

Figure 4.11 shows the excitations at the centred and off-centre positions, with difference profiles showing the absolute difference between the off-centre and centred position excitations, for the position most improved by $\text{MRPs}_{\text{set-3}}$, for each slice. Similar to MRP_1 and MRP_2 , the 15° yaw rotation was the most improved position in every slice, except for one of the middle slices (slice 3) (10° yaw rotation). MRPs reduced nRMSE at these positions by up to 36.1%, from 50% to 13.9% in one of the middle slices (slice 4). The penultimate inferior slice (slice 2) reported an increase in magnitude nRMSE from 19.4% to 30.1%. Referring back to Table 4.6, most phase evaluations for the penultimate inferior slice were degraded, which could have again dominated the selection of the most improved position in this slice. The MRPs reduced phase RMSE by up to 54° , from 71.7° to 17.7° in one of the middle slices (slice 4). $\text{MRPs}_{\text{set-3}}$ were able to

Slice	Phase					
	Positions Improved	Positions Degraded	Mean Improvement ($^{\circ}$)	σ	Mean Degradation ($^{\circ}$)	σ
1	15	7	6.2	14.2	0.5	0.3
2	7	15	3.0	6.1	1.4	2.0
3	19	3	3.8	5.3	0.1	0.1
4	12	10	11.4	19.4	0.7	0.5
5	15	7	7.8	14.1	0.9	0.8
6	10	12	4.1	8.3	0.5	0.4

Table 4.6: The number of phase evaluations (positions) improved/degraded by $\text{MRPs}_{\text{set-3}}$ (10 design positions) and the mean reduction/increase in phase RMSE ($^{\circ}$). The MRPs improved the most positions in one of the middle slices (slice 3), and the least in the penultimate inferior slice (slice 2). The slice 2 MRP improved 7/22 positions, however its mean improvement was 114% greater than its mean degradation. This was the most degraded slice for all phase evaluations of all sets of MRPs.

reduce very large errors in both magnitude and phase evaluations, however did not perform as well as the previous two sets of MRPs. Even though neither the 15° or 10° yaw rotation were included in the $\text{MRP}_{\text{set-3}}$ pulse design, they were the most improved positions by the MRPs.

Considering magnitude nRMSE, MRPs improved performance significantly in all slices with $p \leq 0.05$, except for the penultimate inferior slice (slice 2), where $p = 0.60$. Considering phase RMSE, MRPs improved performance significantly in the middle and superior slices (slices 3 to 6) with $p \leq 0.05$, and similarly in the inferior slices (slices 1 and 2), with $p = 0.06$ and $p = 0.49$, respectively.

MRP pulse lengths ranged between 7.1 ms and 11.2 ms across slices. The percentage increase in pulse length between MRPs and reference pulses, averaged across all slices, was 111%. This is comparable to the other two sets of MRPs ($\text{MRP}_{\text{set-1}}$ and $\text{MRP}_{\text{set-2}}$).

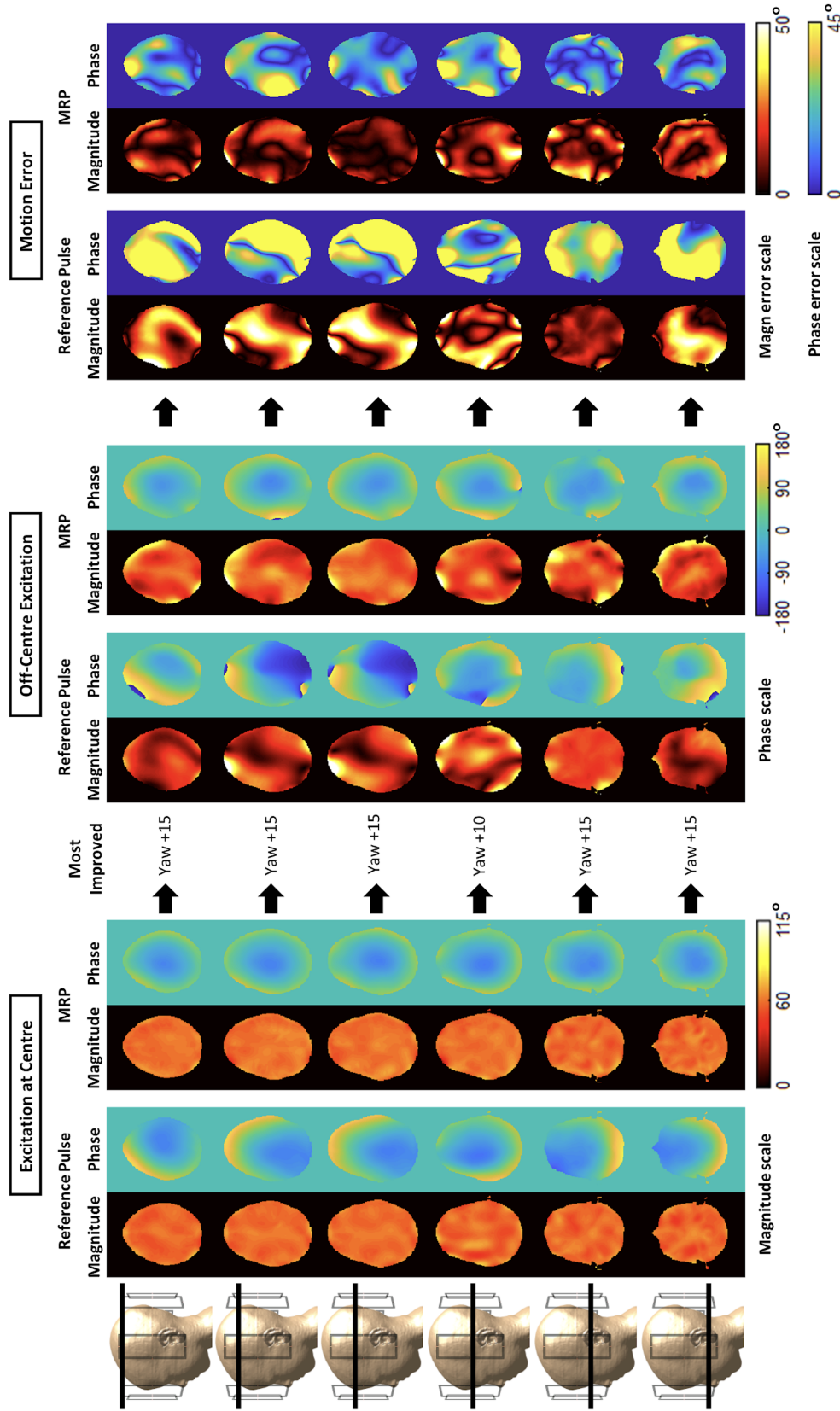


Figure 4.11: The magnitude and phase excitations at the centred and off-centre positions, most improved off-centre excitations, and absolute difference profiles. For slices 1 to 6, $\text{MRP}_{\text{set-2}}$ reduced ref-pulse magnitude nRMSE from 48.0% to 30.0%, 38.1% to 20.2%, 50.0% to 13.9%, 48.4% to 24.5%, 43.6% to 22.0% for slices 1 and 3 to 6 respectively. Slice 2 reported an increase in magnitude nRMSE from 19.4% to 30.1%. For phase, the MRPs reduced ref-pulse RMSE from 70.8° to 21.3°, 35.2° to 18.6°, 32.1° to 12.4°, 71.7° to 17.7°, 68.8° to 29.8° and 47.3° to 20.5° for slices 1 to 6 respectively. The +15° and +10° yaw rotations were the most improved positions, despite not being included in the $\text{MRP}_{\text{set-3}}$ design. Where motion error is shown as zero, this is where the pulses achieved the target flip angle (magnitude), or achieved consistent phase with the centred position.

4.3.4 SAR

Figure 4.12 shows the central $\text{SAR}_{10\text{g-avg}}$ (at the centred position), maximum recorded $\text{SAR}_{10\text{g-avg}}$, and off-centre $\text{SAR}_{10\text{g-avg}}$ relative to each pulse-types central $\text{SAR}_{10\text{g-avg}}$, for $\text{MRPs}_{\text{set-1}}$ (panel a), $\text{MRPs}_{\text{set-2}}$ (panel b) and $\text{MRPs}_{\text{set-3}}$ (panel c) against the reference pulses. For $\text{MRPs}_{\text{set-1}}$ (all 23 positions included in the design), MRP central $\text{SAR}_{10\text{g-avg}}$ and maximum $\text{SAR}_{10\text{g-avg}}$ were lower than ref-pulse $\text{SAR}_{10\text{g-avg}}$ in 5/6 slices. The MRPs reduced central $\text{SAR}_{10\text{g-avg}}$ by a mean of 1.1 W/kg ($\sigma = 1.0$) across slices, and increased central $\text{SAR}_{10\text{g-avg}}$ by 0.29 W/kg in the penultimate inferior slice (slice 2). However, relative to other slices, MRP central $\text{SAR}_{10\text{g-avg}}$ in the penultimate inferior slice was small. The MRPs also reduced maximum $\text{SAR}_{10\text{g-avg}}$ for the same 5 slices, by an average of 1.8 W/kg ($\sigma = 0.9$) and increased maximum $\text{SAR}_{10\text{g-avg}}$ in the penultimate inferior slice by 0.32 W/kg. Again, MRP maximum $\text{SAR}_{10\text{g-avg}}$ for this slice was small relative to other slices. Considering the ratio of off-centre $\text{SAR}_{10\text{g-avg}}$ relative to the centre for all slices, for ref-pulses 70/114 (61%) of positions were above 1 with a mean relative $\text{SAR}_{10\text{g-avg}}$ of 1.4 ($\sigma = 0.4$), averaged over these 70 positions. For the MRPs, 31/114 (27%) of positions were above 1, with a mean relative $\text{SAR}_{10\text{g-avg}}$ of 1.2 ($\sigma = 0.2$). All remaining positions had relative $\text{SAR}_{10\text{g-avg}} \leq 1$.

For $\text{MRPs}_{\text{set-2}}$ (18 design positions) the MRPs reduced central $\text{SAR}_{10\text{g-avg}}$ in two slices, one of the middle slices (slice 4) and the penultimate superior slice (slice 5) by up to 1.36 W/kg. The MRPs increased central $\text{SAR}_{10\text{g-avg}}$ in the other four slices. In two slices (slices 2 and 3), the MRPs performed similarly to the equivalent reference pulses, increasing SAR by up to 0.18 W/kg. The increase in central $\text{SAR}_{10\text{g-avg}}$ by MRPs was larger in the inferior-most and superior-most slices (slices 1 and 6), by up to 4.71 W/kg. Although the increase in central $\text{SAR}_{10\text{g-avg}}$ in the inferior-most and superior-most slices was large,

it did not exceed the 2-fold tolerance allowed during MRP candidate spoke selection. The MRPs reduced maximum $\text{SAR}_{10\text{g-avg}}$ in half of the slices, the inferior-most slice (slice 1), one of the middle slices (slice 4), and the penultimate superior slice (slice 5), by up to 2.06 W/kg. Maximum $\text{SAR}_{10\text{g-avg}}$ was increased in the other half of slices. Two of these slices performed similarly to the equivalent reference pulses, increasing maximum $\text{SAR}_{10\text{g-avg}}$ by up to 0.40 W/kg. The superior-most slice (slice 6) experienced a larger increase in maximum $\text{SAR}_{10\text{g-avg}}$ of 4.44 W/kg. Considering relative $\text{SAR}_{10\text{g-avg}}$, 39/114 (34%) of positions for $\text{MRPs}_{\text{set-2}}$ were above 1, with a mean relative $\text{SAR}_{10\text{g-avg}}$ of 1.3 ($\sigma = 0.3$). All remaining positions had relative $\text{SAR}_{10\text{g-avg}} \leq 1$.

For $\text{MRPs}_{\text{set-3}}$ (10 design positions) the MRPs reduced central $\text{SAR}_{10\text{g-avg}}$ in the two inferior slices (slices 1 and 2) by up to 0.72 W/kg, and increased central $\text{SAR}_{10\text{g-avg}}$ in the remaining four slices by up to 3.50 W/kg (occurring at superior-most slice). Again the MRPs did not exceed the 2-fold central $\text{SAR}_{10\text{g-avg}}$ tolerance. MRPs reduced maximum off-centre $\text{SAR}_{10\text{g-avg}}$ in the inferior slices and one of the middle slices (slices 1, 2 and 4) by up to 3.67 W/kg, and increased maximum $\text{SAR}_{10\text{g-avg}}$ in the remaining slices by up to 3.23 W/kg (again occurring at the superior-most slice). Considering relative $\text{SAR}_{10\text{g-avg}}$, 18/114 (16%) of positions were above 1 (the least of all MRP sets) with a mean relative $\text{SAR}_{10\text{g-avg}}$ of 1.1 ($\sigma = 0.2$). All remaining positions had relative $\text{SAR}_{10\text{g-avg}} \leq 1$.

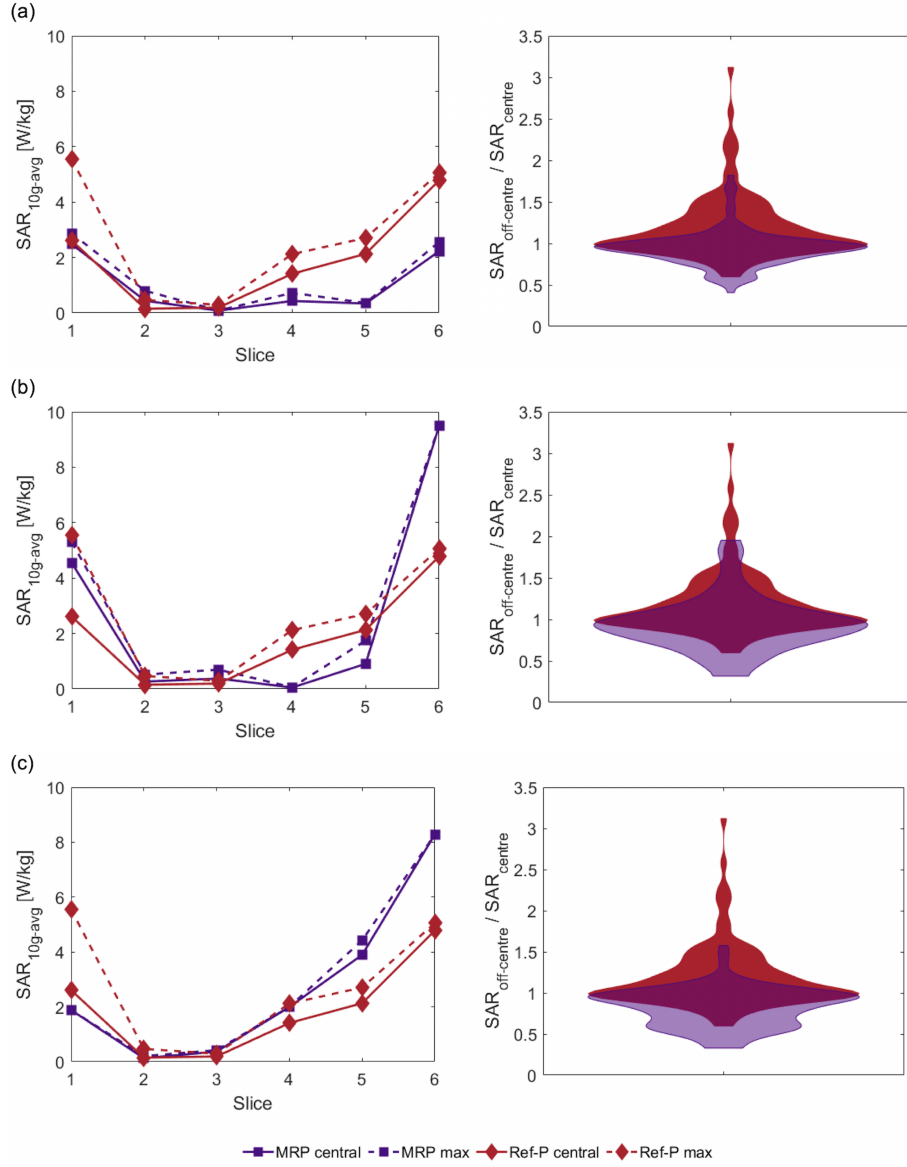


Figure 4.12: The central SAR_{10g-avg} (at the centred position), maximum off-centre SAR_{10g-avg}, and distribution of off-centre SAR_{10g-avg} relative to the central SAR_{10g-avg}, for MRP_{set-1} (panel a), MRP_{set-2} (panel b), MRP_{set-3} (panel c), and the six slice-selective reference pulses. The maximum central SAR_{10g-avg} (across all MRP sets) was 4.8 W/kg for reference pulses, and 9.5 W/kg for MRPs, both occurring at the superior-most slice (slice 6). For maximum SAR_{10g-avg}, the maximum value for reference pulses was 5.6 W/kg for the inferior-most slice (slice 1), and 9.5 W/kg for MRPs in the superior-most slice.

4.4 Discussion

It was shown in previous Chapters (2, 3), that designing motion robust RF pulses (MRPs) by optimising over multiple head positions can maintain better RF excitation quality in the presence of motion than conventional pulses. This study demonstrated that MRPs, designed using estimated off-centre B_1^+ -maps, can still maintain highly homogeneous off-centre magnitude profiles and more consistent phase than conventionally designed reference pulses. Different sets of MRPs were designed using different input B_1^+ -maps, and it was found that using all available positions in the design performed best overall. The MRP design was tested at displacements as large as $15^\circ/20$ mm and showed greatly superior magnitude homogeneity and phase consistency compared to conventionally designed reference pulses.

Previously, the practicality of the MRP design was limited by the requirement of many input B_1^+ -maps, each from a different patient position. However, by using the predicted B_1^+ -maps from the deep learning network developed by Plumley *et al.*, off-centre B_1^+ -maps could be estimated from only the B_1^+ -map at the centred position, collected at the start of scanning as normal. This would greatly reduce the complexity of implementing MRPs in-vivo [1]. This also allows MRPs to be designed using any number of desired input positions, and only the B_1^+ -map at the centred position would be required to do so. How the number of input B_1^+ -maps affected the motion-robustness of the pulses, and how it may degrade the quality of the excitation at the centred positions to the benefit of off-centre excitation, was investigated.

Three sets of six slice-selective MRPs were designed, each including a different number of positions in the design. $\text{MRPs}_{\text{set-1}}$ included all twenty three positions in the design, $\text{MRPs}_{\text{set-2}}$ had eighteen design positions (omitting the 15° yaw rotation, 20 mm left-right and off-axis translations), and $\text{MRPs}_{\text{set-3}}$

had ten design positions (further omitting the 10° yaw rotation, and 10 degree on/off-axis translations). Considering the number of magnitude and phase evaluations improved over all slices, $\text{MRPs}_{\text{set-2}}$ improved the most (202/270, 75%), then $\text{MRPs}_{\text{set-1}}$ (200/270, 74%), then $\text{MRPs}_{\text{set-3}}$ (188/270, 70%). Of the three MRP sets, when evaluated over all positions, $\text{MRPs}_{\text{set-3}}$ performed worse than the other two sets. $\text{MRPs}_{\text{set-2}}$ improved more magnitude evaluations and less phase valuations compared to set 1, however $\text{MRPs}_{\text{set-1}}$ had larger mean improvements in magnitude and phase. All three MRP sets improved the majority of magnitude nRMSE and phase RMSE evaluations, with mean reductions in nRMSE and RMSE greater than the mean increases. Yaw rotations up to 15° were evaluated, and consistently produced the largest ref-pulse errors compared to the other motion types. The MRPs were able to reduce the errors at this position to values consistent with other positions. Typically it was then the off-axis translations producing the largest errors, and left-right on-axis translations were generally worse than on-axis posterior translations. This was consistent across MRP sets. Considering slice-specific $\text{MRPs}_{\text{set-1}}$, at no point did any MRP degraded more positions than it improved in magnitude and phase evaluations.

For $\text{MRPs}_{\text{set-2}}$, the posterior 2 mm off-axis translations reported lower mean magnitude error (averaged across slices) compared to the posterior 5 mm off-axis translations. This non-monotonous dependence of magnitude error on extent of off-centre displacement for MRPs could be due to propagation of the estimation error of B_1^+ -maps through the pulse design algorithm. When B_1^+ -maps were estimated by Plumley *et al.*, smaller displacements yielded larger estimation errors than motion induced errors [1]. This is because the motion-induced errors were smaller than the estimation noise-floor. A similar minimum level of estimation error likely contributed to the non-monotonous error variation here. This is supported by the monotonous increase of error with extent of displacement

in Chapter 3. The non-monotonous error behaviour could also be due to the pseudo brute-force optimisation of candidate spoke selection for MRPs, which may have found better performing k-space trajectories for different MRPs.

Considering the close results between total number of positions improved for $\text{MRPs}_{\text{set-1}}$ and $\text{MRPs}_{\text{set-2}}$, the fact that $\text{MRPs}_{\text{set-1}}$ improved more positions than they degraded in every slice, and superior statistical testing, $\text{MRPs}_{\text{set-1}}$ (all 23 positions included in design) could be determined as the superior set for profile quality when considering motion.

$\text{MRPs}_{\text{set-1}}$ and $\text{MRPs}_{\text{set-2}}$ performed similarly well. $\text{MRPs}_{\text{set-1}}$ improved more positions than they degraded in every slice, and had superior p -levels during statistical testing. However, $\text{MRPs}_{\text{set-1}}$ reported the largest mean profile nRMSE at the centred position, averaged across all slices, increasing mean nRMSE by 12% compared to $\text{MRPs}_{\text{set-2}}$, and 36% compared to $\text{MRPs}_{\text{set-3}}$. This was to be expected considering that as more off-centre positions are added to the design, the less the centred position is weighted. Artificially weighting the centred position could be explored, however this would come at the detriment to off-centre profile homogeneity. Deciding how to trade off magnitude profile homogeneity at the centred position for off-centre homogeneity requires some scan-specific considerations, such as, if large subject motion is expected during a scan.

In general, MRPs struggled against the reference pulses consistently for the penultimate inferior slice (slice 2). This is due to two reasons; for the reference pulses, maximum error in magnitude and phase was much lower in this slice compared to other slices; and conversely, the MRPs reported the largest magnitude and phase errors for this slice compared to other slices. This could be attributed to better candidate spoke selection by the greedy algorithm for this slice during reference pulse design, and a worse minimum found during

candidate spoke selection optimisation during MRP design.

Considering all slices, more magnitude evaluations were improved than phase evaluations, across all sets of MRPs. This is likely due to optimising candidate spoke selection to reduce magnitude nRMSE, which was done to counteract any reduction in magnitude performance caused by the removal of phase relaxation during pulse design. The removal of phase relaxation was necessary to improve consistency in phase profiles across positions, which can produce image artefacts if not accounted for.

For $\text{MRPs}_{\text{set-1}}$ in the penultimate inferior slice (slice 2), no candidate spoke locations produced a central $\text{SAR}_{10\text{g-avg}}$ (at the centred position) within a 2-fold tolerance of the equivalent reference pulse. This was because central $\text{SAR}_{10\text{g-avg}}$ was very small in this slice for both MRPs and reference pulses, and so the tolerance was increased to 3-fold for this case, and the subsequent MRP central $\text{SAR}_{10\text{g-avg}}$ was still very small relative to other slices. Overall $\text{MRPs}_{\text{set-1}}$ performed best against other sets, with generally smaller maximum $\text{SAR}_{10\text{g-avg}}$ values. The variation in $\text{SAR}_{10\text{g-avg}}$ across off-centre positions was less for MRPs than reference pulses.

It would have been desirable to investigate MRPs in a more comprehensive grid of simulated positions, however the positions used in this work were the only B_1^+ -maps available at the time of the experiment. Future work with more simulated positions in the positive and negative directions of each motion type would provide a more comprehensive insight into MRP performance. However, the results presented provide a good basis for understanding how effective and practical using deep learning to predict off-centre B_1^+ -maps to design motion-robust excitation pulses can be.

MRP performance could be further improved by extending the optimisation of the spoke location placement by using a brute force approach and evaluating

all candidate spokes when each spoke it added. This would be computationally intense but there are certain approaches that would make this more practical. For example, a library of pre-designed, fully spoke placement optimised MRPs could be built for a broad range of head sizes/shapes. Then the B_1^+ -map collected for the centred position at the start of a scan could be matched to the most appropriate centred position B_1^+ -map in the library, and the associated motion-robust pulse would be selected. Alternatively in Ref [86], RF pulses are optimised over many different heads (centred position only) to create a universal pulse, providing a “plug and play” approach to pulse design. The design of universal pulses could be extended to include off-centre positions for each of the heads, resulting in a motion-robust universal pulse. Again, the pulses could apply a brute force approach to spoke placement optimisation, allowing for improved pulse performance.

While MRPs perform well under in-silico evaluation, it is desirable to test them in-vivo using scanner-collected B_1^+ -maps. This is the focus of the next and final experimental chapter of this thesis.

In this chapter, MRPs continued to provide increased excitation quality in the presence of head motion, when designed using deep learning estimated B_1^+ -maps. By using estimated maps, this allowed many pulses to be optimised over many input positions, without practicality issues. This provided justification for the freedom to use as many input B_1^+ -maps in the MRP design as desired, and this flexibility is utilised in the next chapter of this thesis.

4.5 Conclusion

The results presented demonstrate that motion-robust excitation pulses can still maintain highly homogeneous flip-angle profiles, and consistent phase, when designed with estimated B_1^+ -maps using deep learning. This offers a viable solution to the motion-robust designs necessity for multiple input B_1^+ -maps, greatly improving the practicality of the design, and allowing larger flexibility in choice of input B_1^+ -maps/positions.

Chapter 5

Motion-Robust pTx

Excitation Pulse Design

Using In-Vivo B_1^+ -maps

Collected at 7T

5.1 Introduction

Thus far, motion-robust pTx excitation spokes pulses have demonstrated superior performance in maintaining excitation quality in the presence of within-scan head motion, when compared to standard/conventional spokes pulses. In an in-silico setting, MRPs are able to maintain more homogeneous flip-angle profiles, and more consistent phase distributions, across many simulated head positions. This is done by considering multiple motion states during initial pulse design, concatenating centred and off-centre B_1^+ -maps and optimising RF

channel weights over all included positions. The nature of the design presented issues with its practicality, requiring B_1^+ acquisitions for multiple head orientations before pulses could be designed. However, a solution was presented by designing MRPs using B_1^+ -maps estimated from a deep learning network designed by Plumley *et al.*, where the only required input was the centred B_1^+ -map [1]. When designed using estimated off-centre B_1^+ , MRPs continued to improve, maintaining magnitude homogeneity and phase consistency across multiple positions. This removed the impracticality of having to collect many off-centre B_1^+ -maps for MRP design, providing freedom to use numerous input positions. Based on this, the MRPs designed in this chapter utilised the B_1^+ -maps from the centred and all off-centre positions, as inputs for pulse design. Although off-centre B_1^+ -maps estimated using deep learning would most likely be suitable to use in this chapter, they were not available and so the off-centre B_1^+ -maps were measured.

While MRP performance was viable in an in-silico setting, it was desirable to test MRPs in an in-vivo setting. This chapter presents a pseudo in-vivo investigation of the MRPs by designing and evaluating pulses using B_1^+ -maps collected in-vivo in a pTx coil at 7T.

5.2 Methods

5.2.1 B_1 Data Collection

The B_1^+ -maps used in this work were a subset of those collected in Ref [81]. The subset of B_1^+ -maps used were collected from one participant at ten different head orientations within an 8-32-channel pTx/Rx coil (Nova Medical, MA, USA) within a Siemens 7 Tesla Magnetom scanner (Siemens Healthcare, Erlangen, Germany), using the scanner’s in-built B_1^+ mapping method, a pre-saturation

based turboFLASH protocol [90]. The inner dimensions of the Rx coil were 205 mm anterior-posterior by 185 mm left-right.

The participant was asked to move their head to a random location and the B_1^+ distribution was collected, as well as a small flip-angle gradient echo (GRE) image. This was repeated for ten different positions. Data was exported to XNAT, an open source imaging informatics platform for managing and sharing imaging and related data [91], and processed using MATLAB (MathWorks, Inc., Natick, MA).

AFNI’s “3dvolreg” function, which estimates spatial deviations between images, was used to acquire estimated motion parameters between the off-centre and centred GRE images [92, 93]. Image registration between off-centre positions and the centre position was performed using linear 3D interpolation of the B_1^+ , with the motion parameters acquired from AFNI. The position-specific B_1^+ -maps were masked using equivalent position-specific GRE profiles within MATLAB’s “ginput” function, which allows manual selection of co-ordinates in an image, and was used to manually bound the data to remove noise outside of the head. A periphery of 1 voxel was also masked out to remove noise missed by the manual bounding method. The result was a masked B_1^+ data set that included the skull, suitable for pulse design. A second B_1^+ data set, where a further 4 voxels were masked to remove the skull and isolate the brain was created for pulse evaluation purposes, as only the excitation homogeneity within the brain was of interest. This second set of B_1^+ -maps are referred to as the evaluation profiles in the text.

5.2.2 Pulse Design

Five slice-selective 5-spoke MRPs were designed in the small-tip-angle (STA) regime using the same adapted spatial domain method as Chapters 3.2 and

4. The B_1^+ of all 10 scanned positions were concatenated and treated as a single slice. RF channel weightings were optimised over all positions via matrix inversion and the phase relaxed magnitude least-squares (MLS) optimisation was not used in the MRP design. Pulses were designed in the patient frame, replicating positional shifts in the gradient fields using the motion data reported by AFNI. Candidate spoke selection was optimised using the quasi-brute-force approach discussed in chapter 3.2. The 10 best performing candidate spokes were evaluated as each spoke was added, resulting in a set of 10,000 MRPs for each slice. The pulse with the lowest magnitude nRMSE calculated over all 10 design positions (as if a single slice) was selected.

Five equivalent slice-selective 3-spoke reference pulses (ref-pulses) were designed using the B_1^+ -map at the centred position only, matrix inversion with a phase relaxed MLS optimisation, and no candidate spoke optimisation, similar to those designed in Chapters 2, 3.2 and 4. Both the MRPs and the ref-pulses were designed using a Tikhonov parameter $\beta = 0.1$. SAR was not investigated as part of this study, and MRP candidate spokes were not SAR filtered. A maximum B_1^+ amplitude constraint (30 μ T) was applied to each pulse type, which scaled RF pulse lengths by adjusting the dwell time.

Pulse design parameters were consistent with previous chapters: flip-angle, 60° ; slice thickness, 1.5 mm; peak RF amplitude, 30 μ T; dwell time, 4 μ s; time-bandwidth (TBW) product, 4; maximum gradient amplitude, 80 mT/m; maximum gradient slew rate, 200 mT/m/ms

Magnitude nRMSE and phase RMSE were calculated in the evaluation profiles using Equations 2.8 and 2.10, for ref-pulses and MRPs. Magnitude nRMSE was calculated in all positions. Phase RMSE was calculated in only the off-centre positions, as their error is relative to the centred position, and so phase RMSE at the centred position was irrelevant. Across all slices and positions, this re-

sulted in 50 magnitude nRMSE evaluations, and 45 phase RMSE evaluations. Variation in magnitude nRMSE and phase RMSE across positions is reported and magnitude and phase profiles of the most and least improved positions are shown. Statistical analysis in the form of a left-tailed paired t-test with 5% significance level ($p \leq 0.05$) was used to investigate slice-specific MRP performance against the ref-pulses. Other pulse performance metrics included the number of positions improved or degraded for each slice and the mean improvement or degradation in magnitude nRMSE/RMSE.

5.3 Results

The motion parameters between each off-centre position and the centred position (position 1), acquired using AFNI's 3dvolreg function for registration between positions, are reported in Table 5.1. The maximum recorded rotation was -10.4° in yaw, occurring at position 5, and the maximum translation was 12.8 mm in the superior direction at position 9. Shifts in the right, posterior and roll axes were relatively small compared to other motion types.

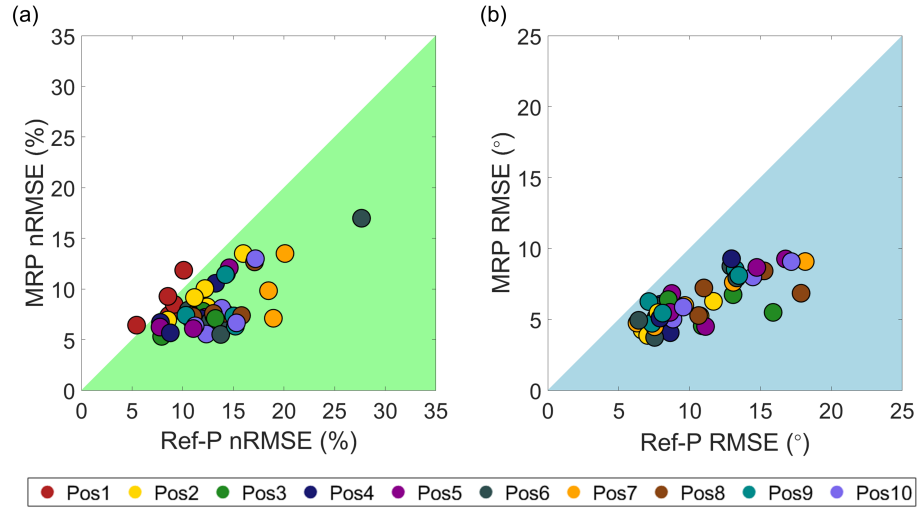


Figure 5.1: The centred and off-centre positions magnitude nRMSE evaluations (panel a) and off-centre phase RMSE evaluations (panel b) for the MRPs against the ref-pulses, across all slices. The MRPs improved 47/50 (94%) of magnitude evaluations with a mean reduction in nRMSE of 4.8% ($\sigma = 2.3$). The three degraded evaluations were the centred positions for slices 1, 4, and 5 with increases in nRMSE of 1.8%, 1.0%, and 0.7% respectively. The MRPs improved all 45 off-centre phase evaluations, with a mean reduction in RMSE of 4.5° ($\sigma = 1.5$).

Position	Yaw (°)	Pitch (°)	Roll (°)	Superior (mm)	Right (mm)	Posterior (mm)
2	3.8	1.4	0	0.3	0.8	-0.1
3	9.1	3.4	1.5	1.8	1.5	-0.7
4	-7.1	6.5	-0.3	2.5	-1.4	-1.2
5	-10.4	5.9	-0.8	2.4	-0.4	-0.6
6	-1.3	6.4	2.1	12.2	0.6	-2.5
7	5.2	5.2	1.3	12.4	0.6	-1.7
8	4.6	3.0	-0.7	12.0	-0.4	0.1
9	0.3	1.0	1.1	12.8	0.7	-1.6
10	1.4	1.4	-0.5	10.8	-0.6	-0.8

Table 5.1: Motion parameters generated using AFNI's 3dvolreg function, for registration between each off-centre position and the centred position (position 1). The maximum recorded off-centre rotation was a -10.4° yaw rotation in position 5, and the largest off-centre translation was 12.8 mm in the superior direction, occurring at position 9.

Figure 5.1 shows all 50 magnitude nRMSE (panel a) and all 45 phase RMSE (panel b) evaluations for the MRPs and ref-pulses, considering all slices (omitting phase at the centred position). The MRPs improved 47/50 (94%) of magnitude evaluations with a mean reduction in nRMSE of 4.8% ($\sigma = 2.3$), from 13.1% ($\sigma = 3.6$) to 8.3% ($\sigma = 2.5$). The three degraded evaluations were the centred positions for the inferior-most slice (slice 1), the penultimate superior slice (slice 4), and the superior-most slice (slice 5), with increases in nRMSE up to 1.8%. The MRPs improved 100% of off-centre phase evaluations for all slices, with a mean reduction in RMSE of 4.5° ($\sigma = 1.5$), from 10.8° ($\sigma = 3.4$) to 6.3° ($\sigma = 1.7$). The ref-pulse design produced the largest magnitude nRMSE, 27.7% at position 6. The MRP reduced this error to an nRMSE of 17.0%, which was also the largest MRP error recorded. The largest phase RMSE produced by the ref-pulses was 18.2° at position 7, which the MRP reduced to 9.1° . The largest MRP phase RMSE recorded was 9.3° at position 4, and the ref-pulse RMSE for the same position/slice was 13.0° .

The slice-specific positions improved/degraded by the MRPs, and mean reduction/increase in magnitude nRMSE and phase RMSE are shown in Tables 5.2 and 5.3, respectively. The MRPs improved all magnitude evaluations (centred and off-centre positions) in 2/5 slices. The remaining three slices had only one position degraded (the centred position), increasing nRMSE at the centred position by no more than 1.8%. The largest ref-pulse mean magnitude nRMSE (averaged across slices) was reduced by the equivalent MRP from 16.4% ($\sigma = 4.5$) to 12.7% ($\sigma = 1.7$). The largest slice-specific improvement by an MRP in mean magnitude nRMSE was from 13.2% ($\sigma = 3.1$) to 7.0% ($\sigma = 1.2$). All off-centre phase evaluations were improved by the MRPs, in all slices. The largest improvement in phase RMSE by MRPs was from 14.9° ($\sigma = 2.5$) to 7.7° ($\sigma = 1.5$).

Slice	Magnitude					
	Positions Improved	Positions Degraded	Mean Improvement (%)	σ	Mean Degradation (%)	σ
1	9	1	4.3	2.7	1.8	0
2	10	0	5.1	2.0	0	0
3	10	0	5.1	2.1	0	0
4	9	1	2.7	1.2	1.0	0
5	9	1	6.9	3.1	0.7	0

Table 5.2: The slice-specific number of magnitude nRMSE evaluations improved/degraded by the MRPs, mean reduction/increase in nRMSE (%) and standard deviations (σ). Slices 2 and 3 saw all positions (centres and off-centres) improved by the MRPs, and slices 1, 4, and 5 only degraded the centred positions, by a maximum of 1.8%

Slice	Phase				
	Positions Improved	Positions Degraded	Mean Improvement ($^{\circ}$)	σ	
1	9	0	5.9	1.1	
2	9	0	7.2	2.6	
3	9	0	2.0	0.6	
4	9	0	4.4	1.5	
5	9	0	2.8	0.8	

Table 5.3: The slice-specific number of phase RMSE evaluations improved/degraded by the MRPs, the mean reduction in RMSE($^{\circ}$) and standard deviations (σ). All off-centre phase evaluations for all slices were improved by the MRPs. Slice 2 had the largest mean reduction in RMSE (7.2° , $\sigma = 2.6$) and slice 3 the least (2.0° , $\sigma = 0.6$).

Figure 5.2 shows variation in magnitude nRMSE and phase RMSE across positions for each slice (panel a, panel b) and across slices for each position (panel c, panel d), for the reference pulses (ref-pulses). For magnitude nRMSE, positional variations caused between 5.4% and 27.7% nRMSE across positions and slices, and slice-specific mean nRMSE across positions ranged between 9.1% ($\sigma = 1.8$) and 16.4% ($\sigma = 4.5$). For phase RMSE, positional variations caused between 6.3° and 18.2° RMSE across positions and slices, and slice-specific mean RMSE across positions ranged between 7.5° ($\sigma = 0.7$) and 14.9° ($\sigma = 2.4$).

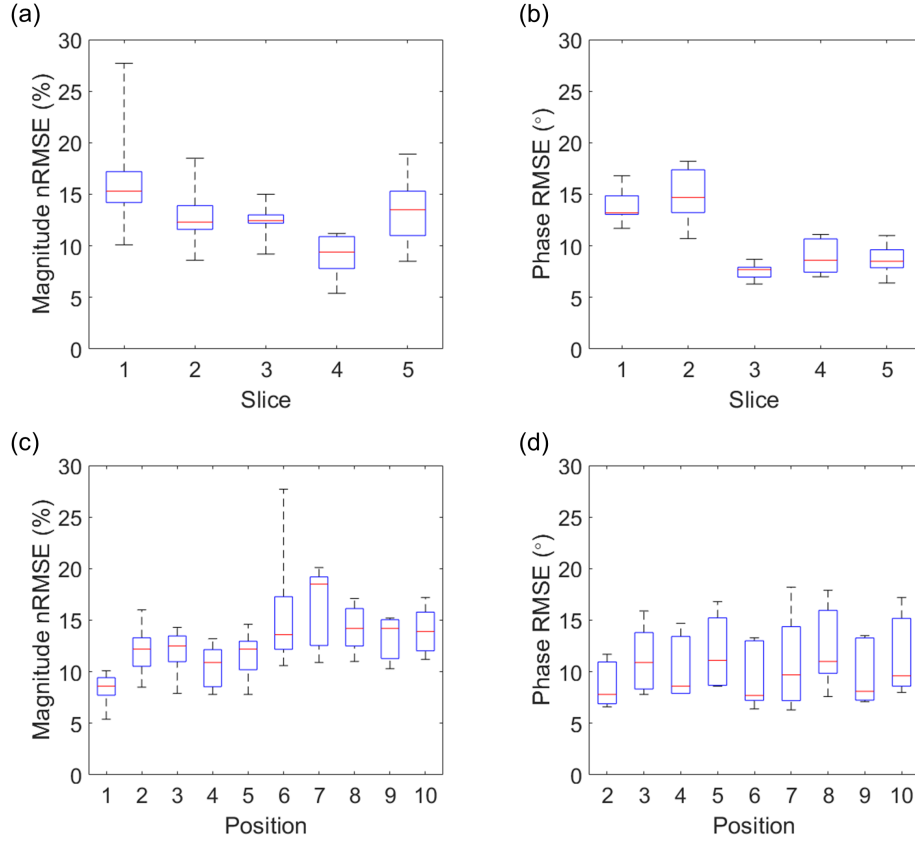


Figure 5.2: Slice-wise variation in magnitude nRMSE (panel a) and phase RMSE (panel b) across all 10 positions (9 for phase, centre omitted) for the five slice-selective reference pulses. Position-wise variation in magnitude nRMSE (panel c) and phase RMSE (panel d) across all slices is also shown. The motion parameters associated with each off-centre position are shown in Table 5.1. Position 1 is the centred position.

The slice-wise variation in magnitude nRMSE and phase RMSE across positions for the MRPs are shown in Figure 5.3(panel a, panel b), respectively. The slices that observed the smallest and largest mean magnitude nRMSEs, and ranges in magnitude nRMSE, were the same for ref-pulses and MRPs. The MRPs reduced magnitude nRMSE error range from (5.4% - 27.7%) to (5.3% - 17.0%), and reduced the largest mean magnitude nRMSE, averaged across positions, from 16.4% ($\sigma = 4.5$) to 12.7% ($\sigma = 1.7$), occurring in the inferior-most

slice (slice 1). The MRPs reduced the smallest mean magnitude nRMSE from 9.1% ($\sigma = 1.8$) to 6.8% ($\sigma = 0.7$), occurring in the penultimate superior slice (slice 4). For phase RMSE, The MRPs reduced the error range from (6.3° - 18.2°) to (3.7° - 9.3°). The largest mean phase RMSE was reduced by MRPs from 14.9° ($\sigma = 2.4$) to 7.7° ($\sigma = 1.5$) for the penultimate inferior slice (slice 2), and the smallest mean phase RMSE from 7.5° ($\sigma = 0.7$) to 5.5° ($\sigma = 0.8$) for the middle slice (slice 3).

Figure 5.3 (panel c, panel d) shows position-wise variation in magnitude nRMSE and phase RMSE across slices, respectively, for the MRPs. The smallest range in nRMSE for ref-pulses occurred at the centred position (position 1), which the MRPs increased from (5.4% - 10.1%) to (6.4% - 11.9%). This was expected as the ref-pulses were optimised for this position only. However, for the off-centre positions, MRPs reduced the smallest magnitude nRMSE range from (10.3% - 15.2%) to (6.3% - 11.4%). The MRPs also reduced the largest mean magnitude nRMSE (averaged across all slices) from 16.3% ($\sigma = 3.6$) to 9.0% ($\sigma = 2.4$). The MRPs reduced the largest mean phase RMSE, averaged across slices, from 12.5° ($\sigma = 3.6$) to 6.6° ($\sigma = 1.2$). The smallest phase RMSE was also reduced, from 8.8° ($\sigma = 2.0$) to 5.0° ($\sigma = 0.9$). The largest MRP mean phase RMSE was smaller than the smallest ref-pulse mean RMSE.

The centred/off-centre positions magnitude and phase excitations for the position most improved by the MRPs in each slice, and profiles of the absolute difference between the off-centre and centred positions excitations, are shown in Figure 5.4. The MRPs were able to remove all areas of high intensity error in phase profiles, and almost all in magnitude. Across slices, the MRPs reduced magnitude nRMSE by up to 11.8% from 18.9% to 7.1% in the inferior-most slice. The MRPs reduced phase RMSE across slices by up to 9.1° from 18.2° to 9.1° in the penultimate superior slice (slice 4). Considering magnitude and

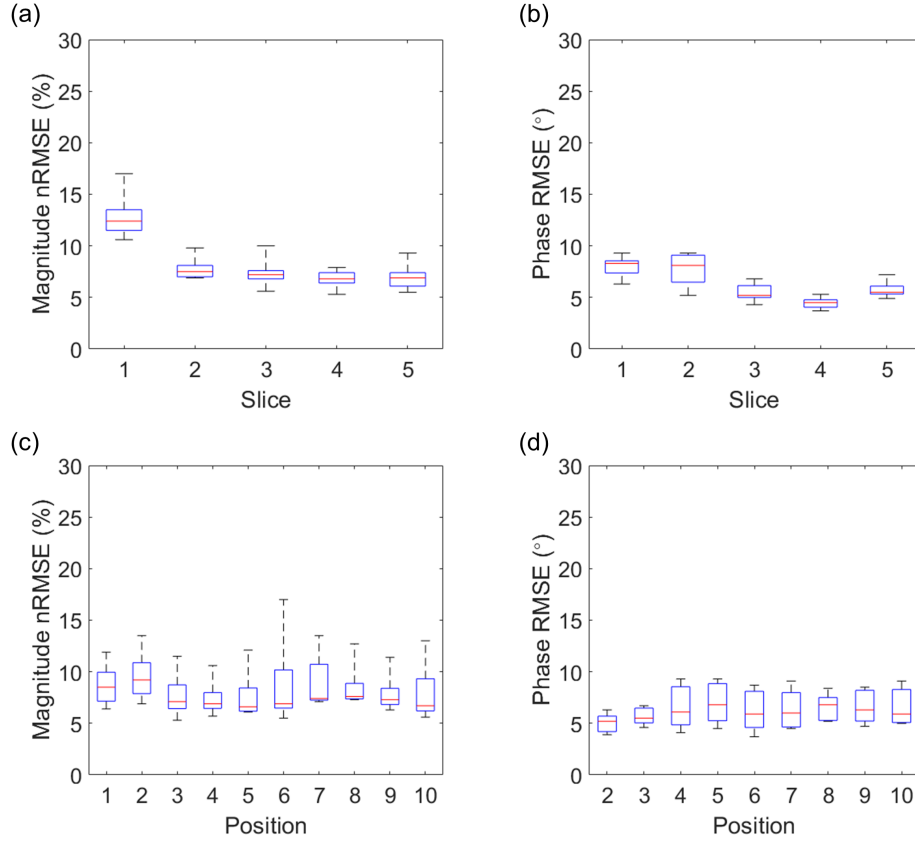


Figure 5.3: Slice-wise variation in magnitude nRMSE (panel a) and phase RMSE (panel b) across all 10 positions (9 for phase, centre omitted) for the five slice-selective MRPs. Position-wise variation in magnitude nRMSE (panel c) and phase RMSE (panel d) across all slices is also shown. The motion parameters associated with each off-centre position are shown in Table 5.1. Position 1 is the centred position.

phase errors, the most improved positions for slices 1 to 5 were positions 6, 7, 10, 8, and 7 respectively, and their motion parameters are displayed in Table 5.1.

The excitation and error profiles for the positions least improved by the MRPs are shown in Figure 5.5. For all slices, the centred position was the least improved position, which was expected as the reference pulses were optimised for this position only. Because there was no target phase profile for the centred

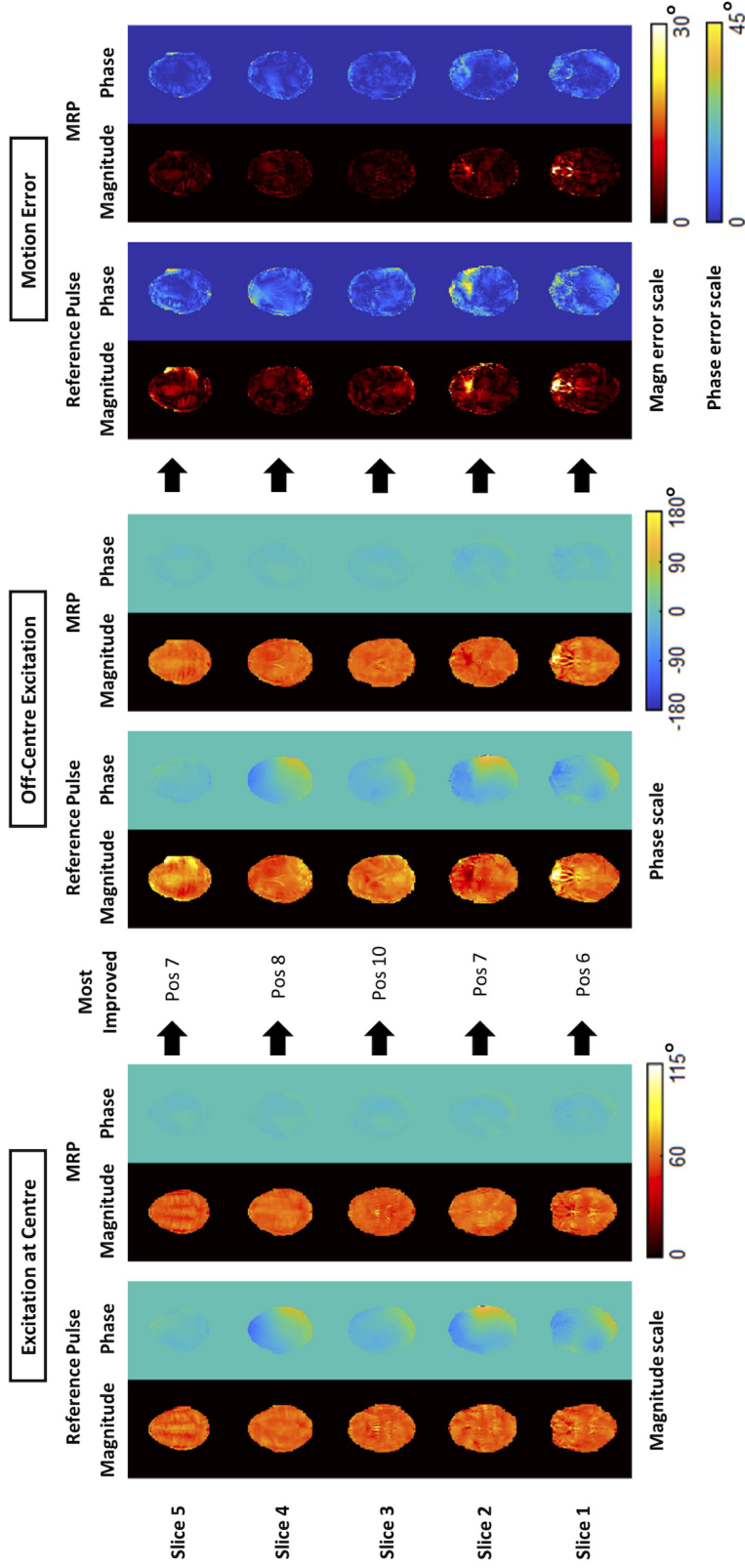


Figure 5.4: Centred and off-centre positions magnitude and phase excitations for the positions most improved by the MRPs for each slice, with profiles of the absolute difference between off-centre and centred positions excitations. For slices 1 to 5, the MRPs reduce magnitude nRMSE from 18.9% to 7.1%, 11.0% to 7.3%, 12.3% to 5.6%, 18.5% to 9.8%, and 27.7% to 17.0%, respectively. The MRPs reduce phase RMSE from 9.7° to 6.0°, 10.6° to 5.3°, 8.0° to 5.1°, 18.2° to 9.1°, and from 12.9° to 8.7° for slices 1 to 5 respectively. Where motion error is shown as zero, this is where the pulses achieved the target flip angle (magnitude), or achieved consistent phase with the centred position.

positions, only the magnitude profiles are displayed. The error profiles are the absolute difference between the centred position magnitude excitation, and a fully homogeneous profile of the target flip-angle (60°). For the penultimate inferior slice (slice 2) and the middle slice (slice 3), the MRPs reduced magnitude nRMSE by up to 1.2%. For the other three slices, the MRPs increased magnitude nRMSE by up to 1.8%. Qualitatively, the MRP performance is very similar to the reference pulses at the centre, and neither pulses produced areas of high intensity errors.

Slice-specific left-tailed paired t-tests (5% significance) for magnitude nRMSE and phase RMSE evaluations showed the benefit of the MRPs was statistically significant in all slices. For both the magnitude and phase evaluations, all slice-specific p -values were $p < 0.001$, except for the inferior-most slice, which was $p = 0.003$.

The mean RF pulse length for the 3-spoke ref-pulses (averaged over all 5 slices) was 6.3 ms ($\sigma = 0.8$). The mean RF pulse length for the 5-spoke MRPs was only 19% larger, at 7.5 ms ($\sigma = 0.4$).

5.4 Discussion

The aim of this study was to identify if the MRP performance demonstrated in Chapters 3.2 and 4 translated into a pseudo in-vivo setting. The five slice-selective MRPs outperformed the equivalent reference pulses in the vast majority (94%) of magnitude nRMSE evaluations, and all phase evaluations. The MRPs proved effective at reducing areas of high intensity absolute error in both magnitude and phase profiles.

Unlike previous investigations into MRPs, each of the 9 off-centre positions experienced changes in all six degrees of freedom of motion (except position 2 which experienced no rotation in roll). The largest translations were along

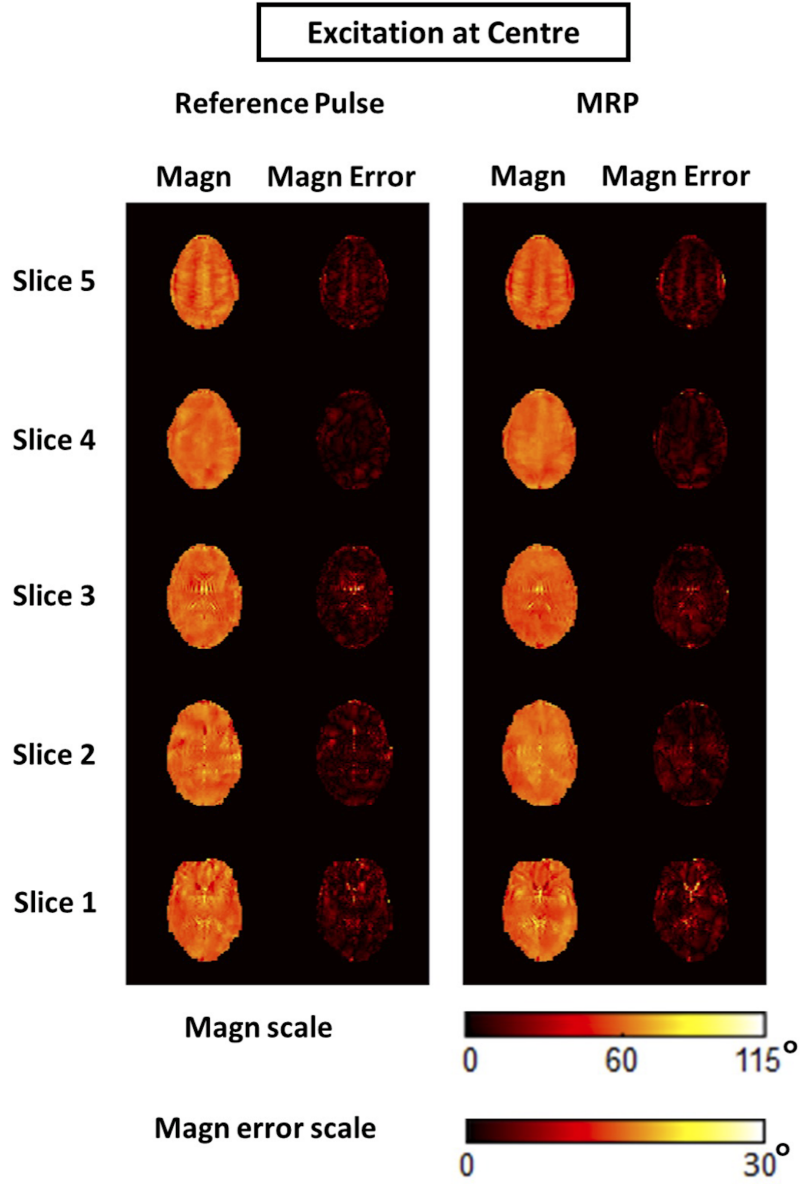


Figure 5.5: Centred position magnitude (magn) excitations and error profiles for each slice-selective reference pulse and MRP for the positions least improved by the MRPs. For each slice, the least improved position was the centred position excitation. Only the magnitude profiles are shown as there is no target phase for the centre. The error profiles are the absolute difference between the centred position excitation and a homogeneous profile of the target flip-angle (60°). For slices 2 and 3, the MRPs reduced magnitude nRMSE from 8.6% to 7.4% and 9.2% to 8.5% respectively. For slices 1, 4, and 5, the MRPs increased magnitude nRMSE by a mean of 1.2% ($\sigma = 0.4$).

the superior-inferior axis, which experienced shifts of up to 14.4 mm. Translations in the left-right axis were less extreme than all other types of motion. The largest rotations were those in the yaw direction (up to 10.4°), followed by pitch, then roll. As all positions had shifts in almost all axes/planes, it was difficult to identify which motion-type produced the largest errors. However, identifying the positions reporting the largest combination of magnitude and phase error showed superior-inferior displacements as a dominant source of error. This would be consistent with in-silico findings presented in Chapter 3.2, where translations of up to 5 mm in the superior-inferior axis also caused large magnitude errors, often similar to 5° rotations in pitch/roll. In this work, translations in the superior-inferior axis were typically much larger than rotations. Chapter 3.2 had identified pitch rotations as the cause of maximum phase error. Similarly, pitch rotations yielded large errors here, although these positions were also coupled with yaw rotations and large superior-inferior displacements. Further work could investigate the effect of each motion-type on both MRPs and reference pulses, in an in-vivo or pseudo in-vivo setting. This could be done by collecting B_1^+ -maps using a phantom that is displaced by a known quantity in each degree of freedom of motion separately.

The MRPs degraded only three evaluations, which were centred position magnitude evaluations. This was expected as the reference pulses were designed with a phase relaxed MLS optimization for the centred position. Despite removing the phase relaxed MLS optimisation for the MRP design, MRPs outperformed the reference pulses at the centre for two slices. This is due to a combination of increasing the number of spokes and optimising candidate spoke selection in the MRP design, which likely outperformed the greedy selection of candidate spokes for the three-spoke reference pulses.

The trade-off between MRP pulse length and magnitude homogeneity was

smaller in this work than in previous Chapters. The MRPs mean RF pulse length, averaged across slices, was only 20% longer than the reference pulses for the pseudo in-vivo pulses, where as in Chapters 3.2 and 4, the MRPs were roughly 150% and 100% longer, respectively. The 3-spoke reference RF pulses in this work were approximately 60% longer than those in Chapters 3.2 and 4. This is likely due to the fact a smaller RF power regularisation term was used in this chapter, resulting in the dwell time being increased to adhere to the maximum B_1^+ amplitude constraint. This was done to be consistent with the MRP design, as candidate spoke locations were not filtered by reference pulse actual 10-g averaged local SAR ($\text{SAR}_{10\text{g-avg}}$) at the centred position, as SAR maps were unavailable. However, both pulse designs were constrained by the same maximum B_1^+ amplitude constraint (30 μT), adjusting the dwell time if it was exceeded.

5.5 Conclusion

Motion-robust pTx excitation pulses, designed and evaluated using in-vivo B_1^+ -maps, showed excellent magnitude homogeneity and phase consistency across off-centre head orientations. Pulses were designed and tested using B_1^+ -maps from positions that experienced shifts in all degrees of freedom of motion simultaneously. The results presented showed further evidence that motion-robust pulses could be an effective method for mitigating the degradation in excitation quality caused by within-scan patient head motion.

Chapter 6

Conclusion

6.1 Thesis Summary

Ultra-high field (UHF) MRI offers higher signal-to-noise and contrast-to-noise ratios compared to lower B_0 -field strengths, which can be leveraged for improved spatial or temporal resolution, but suffers from B_1^+ inhomogeneity, which can lead to artificial signal and contrast variations in the image [3, 9, 16, 17, 20, 21]. To improve B_1^+ homogeneity at UHF, parallel transmission RF excitation (pTx) systems are used [29–31]. Using pTx coils, non-identical RF pulses can be simultaneously applied through multiple independently powered transmit channels, reducing excitation pulse duration and increasing global excitation homogeneity.

Within-scan patient head motion in neuroimaging MRI can lead to imaging artifacts [59–62]. This is because patient motion changes electromagnetic fields, and can rapidly deteriorate flip-angle homogeneity of pTx pulses. The changes in coil-tissue distance exacerbates B_1^+ inhomogeneity and may cause flip-angle inconsistencies when motion occurs mid-acquisition, rendering previ-

ously designed pulses sub-optimal. This results in degraded excitation fidelity and imaging artefacts such as blurring or aliasing [61, 62]. Within-scan patient motion is a common issue when imaging cohorts such as Parkinson’s disease, Alzheimer’s disease and dementia, and paediatrics [51–57]. Sometimes patient conditions require sedation, however this is invasive and doesn’t always eliminate motion-related issues [51, 52, 54, 63]. Prospective and retrospective motion correction techniques are used as non-invasive methods of recovering imaging quality [67–75]. The variation in image contrast caused by within-scan patient motion is related to the RF excitation. This requires prospective motion correction techniques, which perform real-time updating of image acquisition to recover contrast homogeneity [74, 75]. The added complexity of pulse-design for pTx increases computation times past what is feasible for typical prospective motion correction. Therefore an alternative method to prospectively account for within-scan patient motion in pTx is required.

In this thesis, a method was demonstrated in-silico for reducing the effects of patient head motion on radiofrequency field homogeneity for pTx. This was achieved by optimising RF pulses over the centered head position, and eleven off-centre positions during initial pulse design, using B_1^+ -maps simulated within a generic 8-channel pTx transmit array. Slice-selective MRPs were designed and evaluated over 53 simulated positions covering all six degrees of freedom of motion (up to ± 5 mm translations and $\pm 5^\circ$ rotations), and compared to conventionally designed reference pulses (optimised over the centred position only). MRPs improved homogeneity in the flip-angle magnitude over all six degrees of freedom of motion. Further work was performed on improving flip-angle phase consistency across off-centre positions, which if not accounted for, can also lead to image artefacts such as blurring or aliasing. This was done by removing phase relaxation and implementing a quasi brute force optimisation

of the candidate spoke selection during pulse design. This greatly improved off-centre phase consistency, and maintained strong magnitude homogeneity.

The MRPs design requirement of input B_1^+ -maps from multiple head positions would increase scan complexity and required scan time. However, recent work by Plumley *et al.* demonstrated how a deep learning neural network could be used to estimate off-centre B_1^+ -maps from only a single B_1^+ -map, collected at the centred position Ref [1]. This showed potential for improving the practicality of the MRP design, and would allow any desired combination of input B_1^+ -maps. MRPs were designed using estimated off-centre B_1^+ -maps, and when evaluated in simulated off-centre positions, maintained better flip-angle magnitude homogeneity and phase consistency than conventional non-motion-robust pulses. This demonstrated great potential for improving in-vivo MRP practicality while maintaining strong excitation performance in the presence of motion.

Finally a pseudo in-vivo investigation of the MRP design was performed using ten B_1^+ -maps collected in-vivo using an 8-32-channel pTx/Rx coil (Nova Medical, MA, USA) within a Siemens 7T Magnetom scanner (Siemens Healthcare, Erlangen, Germany). Slice-selective MRPs were designed using all ten B_1^+ -maps (one centred and nine off-centre positions), and compared to conventional pulses, designed using only the centred B_1^+ -map. MRPs again were able to maintain superior flip-angle magnitude homogeneity and off-centre phase consistency.

The work done in this thesis has demonstrated in-silico and pseudo in-vivo, the potential of MRPs as a non-invasive and prospective method of accounting for patient head motion within a generic pTx system. The MRP method removes the need for real-time pulse redesign, and if combined with a method for estimating off-centre B_1^+ -maps, can be designed from a single collected B_1^+ -map. Future development of this method could greatly benefit imaging of cohorts af-

ected by within-scan motion such as Parkinson’s, Alzheimer’s, dementia, and paediatrics, by reducing motion-related image artefacts.

6.2 Possible Future Directions

Pre-Designed MRP Library

The results presented in Chapter 3.2 show the effectiveness of optimising the candidate spoke selection during pulse design. The MRPs designed in this work used a 5x5 candidate spoke grid, selecting one and removing it from the candidate selection as each spoke is added, with the DC-point always chosen first. In Chapter 3.2 we analysed the 10 best (highest RF-norm) candidates as each spoke was added, and used a quasi-brute-force approach by designing MRPs for all combinations of the ten best candidates. For a 5-spoke pulse, this led to 10,000 MRPs for each slice. By doing this, and selecting the MRP that produced the lowest magnitude nRMSE over all the design positions, we were able to remove phase relaxation from the MRP design, allowing improved phase consistency across positions. This led to superior magnitude and phase profiles compared to reference pulses. Only a quasi-brute-force optimisation of the candidate spoke selection was applied due to computation time limitations (about 7 hours per slice). However, it would be of interest to design MRPs with a fully brute forced optimisation of candidate spoke selection. For a 5-spoke pulse and a 5x5 candidate spoke grid, this would produce 390,625 MRPs per slice. In a setting where computation time scales linearly with the number of pulses designed, a fully brute force approach to candidate spoke selection would take approximately 270 hours, per slice. However, if designing MRPs for the purpose of building a library or pre-built MRPs, this computation time becomes less important. A library of MRPs designed for many different head sizes/shapes

could be built, similar to the work in Ref [85]. As the B_1^+ -map at the centred position is collected at the start of a scanning session, it could be mapped to the closest matching centred position B_1^+ -map within the MRP library. Then the equivalent pre-built, fully spoke location optimised MRP could be selected and applied, providing a fully “plug and play” approach to motion-robust RF excitation.

Motion-Robust Universal Pulse

Universal pulses have been designed which optimise a single RF pulse for centred position excitation homogeneity over multiple different head models [86]. This provides a “plug and play” calibration-free approach to pTx excitation. An investigation into how within-scan patient motion would deteriorate the magnitude and phase excitation quality of these pulses would be of interest, and if it could be mitigated by combining the motion-robust approach discussed in this work with universal pulse approach. By extending the optimisation to also include off-centre B_1^+ for multiple heads, a motion-robust universal pulse could be designed. If motion-robust universal pulses demonstrated the ability to maintain high quality off-centre excitations, with minimal detriment to the excitation at the centred position, and acceptable RF pulse lengths and SAR, then this could be another approach to calibration-free motion-robust RF excitation.

Dynamic RF Pulse and Real-Time Pulse Redesign

During dynamic RF shimming, different RF transmit channel coefficients/weightings are calculated on a slice-by-slice basis [26, 85]. The shim settings are adjusted dynamically to these weightings as the imaging sequences progresses through each slice, allowing for improved excitation quality across slices. The MRPs designed in this work were slice-selective, with channel weightings optimised on a slice-by-slice basis. It is anticipated that the MRP design could be extended

to a whole brain shimming scheme, however this may reduce performance as shimming for the whole brain, as well as multiple positions, may overly stress the optimisation and lead to poor quality excitations. Further work is needed to understand how the MRP design would perform for whole brain scanning and multi-slice excitation.

As discussed in Section 4.1 of Chapter 4, real-time pulse redesign is a method of accounting for within-scan patient motion. It involves updating RF pulses as motion occurs, optimising channel weightings for the new patient position in real time, and can be used as an effective method for reducing motion-related magnitude and phase inhomogeneity [76]. This requires knowledge of the coil sensitivity distribution (B_1^+) at the new patient position, which can be estimated using a deep learning approach such as in Ref [1]. While MRPs provide a "plug and play" approach that does not require the additional computational resources needed for real-time pulse redesign, it is likely that MRPs cannot perform as well as redesigned pulses that are tailored specifically to the new patient position. Further investigation into how the MRPs perform against a real-time pulse redesign method is needed.

Incorporating B_0 , off-resonance effects, and fully in-vivo experiments

Variations in the B_0 -field must also be considered during pulse design, and within-scan patient motion can lead to variations in B_0 inhomogeneity [94, 95]. Therefore, it is necessary to investigate MRPs with B_0 -field considerations. The shortening of RF pulses made possible by pTx coils has been shown to reduce sensitivity B_0 inhomogeneity, and therefore may not drastically affect the motion-robust design [30, 78]. To investigate the effects of B_0 , the currently designed motion-robust pulses, designed assuming a homogeneous B_0 -field, can be compared to motion-robust pulses designed also using multiple input off-centre B_0 -maps, concatenated and treated similarly to the B_1^+ .

Shorter RF pulses have also been shown to be less sensitive to off-resonance effects [30, 35, 78]. Grissom *et al.* demonstrated that when designing spokes pulses using their proposed “interleaved greedy and local spokes pulse design” method, incorporating a measured off-resonance map in pulse design substantially reduced the excitation error of pTx pulses [35]. When investigating the MRP design fully in-vivo, off-resonance and B_0 inhomogeneity considerations should be made.

While a pseudo in-vivo investigation of MRPs showed very promising results, a fully in-vivo investigation that incorporates structural scanning using the motion-robust excitation pulses is required. Once the B_0 inhomogeneity and off-resonance effects are incorporated into the design, if showing good results in-silico or in a pseudo in-vivo setting, then investigating fully in-vivo and evaluating structural scan images would be the natural progression of this work. When investigating MRPs in-vivo, like other prospective motion correction techniques, MRPs would require motion tracking for image reconstruction [79, 88, 89].

To conclude, the ideas discussed here lead to several different possible future implementations of the MRP design. One is patient-tailored MRPs, combined with estimated off-centre B_1^+ -maps. A second is a pre-built library of more extensively optimised MRPs (more candidate spokes evaluated and using scanned off-centre B_1^+ -maps), selecting the most appropriate MRP on a patient-specific basis. And a third is optimising MRPs over multiple different head shapes and sizes, and their equivalent off-centre positions, to produce a motion-robust universal pulse.

Bibliography

- [1] Alix Plumley, Luke Watkins, Matthias Treder, Patrick Liebig, Kevin Murphy, and Emre Kopanoglu. Rigid motion-resolved prediction using deep learning for real-time parallel-transmission pulse design. *Magnetic Resonance in Medicine*, 87(5):2254–2270, 2022.
- [2] Felix Bloch. Nuclear induction. *Physical review*, 70(7-8):460, 1946.
- [3] GH Glover, CE Hayes, NJ Pelc, WA Edelstein, OM Mueller, HR Hart, CJ Hardy, M O’donnell, and WD Barber. Comparison of linear and circular polarization for magnetic resonance imaging. *Journal of Magnetic Resonance (1969)*, 64(2):255–270, 1985.
- [4] Emre Kopanoglu, VB Erturk, and Ergin Atalar. Analytic expressions for the ultimate intrinsic signal-to-noise ratio and ultimate intrinsic specific absorption rate in mri. *Magnetic resonance in medicine*, 66(3):846–858, 2011.
- [5] DI Hoult. NMR imaging. Rotating frame selective pulses. *Journal of Magnetic Resonance (1969)*, 38(2):369–374, 1980.
- [6] Peter M Joseph, Leon Axel, and Matthew O’Donnell. Potential problems with selective pulses in NMR imaging systems. *Medical physics*, 11(6):772–777, 1984.

- [7] John Pauly, Patrick Le Roux, Dwight Nishimura, and Albert Macovski. Parameter relations for the Shinnar-Le Roux selective excitation pulse design algorithm (NMR imaging). *IEEE transactions on medical imaging*, 10(1):53–65, 1991.
- [8] Matt A Bernstein, Kevin F King, and Xiaohong Joe Zhou. *Handbook of MRI pulse sequences*. Elsevier, 2004.
- [9] Qing X Yang, Jinghua Wang, Xiaoliang Zhang, Christopher M Collins, Michael B Smith, Haiying Liu, Xiao-Hong Zhu, J Thomas Vaughan, Kamil Ugurbil, and Wei Chen. Analysis of wave behavior in lossy dielectric samples at high field. *Magnetic resonance in medicine: an official journal of the international society for magnetic resonance in medicine*, 47(5):982–989, 2002.
- [10] David Moratal, A Vallés-Luch, Luis Martí-Bonmatí, and Marijn E Brummer. k-space tutorial: an MRI educational tool for a better understanding of k-space. *Biomedical imaging and intervention journal*, 4(1), 2008.
- [11] Thomas A Gallagher, Alexander J Nemeth, and Lotfi Hacein-Bey. An introduction to the Fourier transform: relationship to MRI. *American journal of roentgenology*, 190(5):1396–1405, 2008.
- [12] David I Hoult and RE Richards. The signal-to-noise ratio of the nuclear magnetic resonance experiment. *Journal of Magnetic Resonance (1969)*, 24(1):71–85, 1976.
- [13] WA Edelstein, GH Glover, CJ Hardy, and RW Redington. The intrinsic signal-to-noise ratio in NMR imaging. *Magnetic resonance in medicine*, 3(4):604–618, 1986.

- [14] David I Hoult. Sensitivity and power deposition in a high-field imaging experiment. *Journal of Magnetic Resonance Imaging*, 12(1):46–67, 2000.
- [15] Bastien Guérin, Jorge F Villena, Athanasios G Polimeridis, Elfar Adalsteinsson, Luca Daniel, Jacob K White, and Lawrence L Wald. The ultimate signal-to-noise ratio in realistic body models. *Magnetic resonance in medicine*, 78(5):1969–1980, 2017.
- [16] Joseph S Gati, Ravi S Menon, Kâmil Uğurbil, and Brian K Rutt. Experimental determination of the BOLD field strength dependence in vessels and tissue. *Magnetic resonance in medicine*, 38(2):296–302, 1997.
- [17] Anja G Van der Kolk, Jeroen Hendrikse, Jaco JM Zwanenburg, Fredy Visser, and Peter R Luijten. Clinical applications of 7 T MRI in the brain. *European journal of radiology*, 82(5):708–718, 2013.
- [18] Daniel Stucht, K Appu Danishad, Peter Schulze, Frank Godenschweger, Maxim Zaitsev, and Oliver Speck. Highest resolution in vivo human brain MRI using prospective motion correction. *PloS one*, 10(7):e0133921, 2015.
- [19] Falk Lüsebrink, Alessandro Sciarra, Hendrik Mattern, Renat Yakupov, and Oliver Speck. T1-weighted in vivo human whole brain MRI dataset with an ultrahigh isotropic resolution of 250 μm . *Scientific data*, 4(1):1–12, 2017.
- [20] Paul A Bottomley and E Raymond Andrew. RF magnetic field penetration, phase shift and power dissipation in biological tissue: implications for NMR imaging. *Physics in Medicine & Biology*, 23(4):630, 1978.
- [21] Laurel S Morris, Prantik Kundu, Sara Costi, Abigail Collins, Molly Schneider, Gaurav Verma, Priti Balchandani, and James W Murrough. Ultra-high field MRI reveals mood-related circuit disturbances in depression: a com-

- parison between 3-Tesla and 7-Tesla. *Translational Psychiatry*, 9(1):1–11, 2019.
- [22] Oliver Kraff, Anja Fischer, Armin M Nagel, Christoph Mönninghoff, and Mark E Ladd. MRI at 7 Tesla and above: demonstrated and potential capabilities. *Journal of Magnetic Resonance Imaging*, 41(1):13–33, 2015.
- [23] Kamil Uğurbil, Junqian Xu, Edward J Auerbach, Steen Moeller, An T Vu, Julio M Duarte-Carvajalino, Christophe Lenglet, Xiaoping Wu, Sebastian Schmitter, Pierre Francois Van de Moortele, et al. Pushing spatial and temporal resolution for functional and diffusion MRI in the human connectome project. *Neuroimage*, 80:80–104, 2013.
- [24] Kamil Uğurbil. Imaging at ultrahigh magnetic fields: History, challenges, and solutions. *Neuroimage*, 168:7–32, 2018.
- [25] Kawin Setsompop, R Kimmlingen, E Eberlein, Thomas Witzel, Julien Cohen-Adad, Jennifer A McNab, Boris Keil, M Dylan Tisdall, P Hoecht, Peter Dietz, et al. Pushing the limits of in vivo diffusion MRI for the human connectome project. *Neuroimage*, 80:220–233, 2013.
- [26] Francesco Padormo, Arian Beqiri, Joseph V Hajnal, and Shaihan J Malik. Parallel transmission for ultrahigh-field imaging. *NMR in Biomedicine*, 29(9):1145–1161, 2016.
- [27] Daniel K Sodickson and Warren J Manning. Simultaneous acquisition of spatial harmonics (smash): fast imaging with radiofrequency coil arrays. *Magnetic resonance in medicine*, 38(4):591–603, 1997.
- [28] Klaas P Pruessmann, Markus Weiger, Markus B Scheidegger, and Peter Boesiger. Sense: sensitivity encoding for fast MRI. *Magnetic Resonance*

in Medicine: An Official Journal of the International Society for Magnetic Resonance in Medicine, 42(5):952–962, 1999.

- [29] Ulrich Katscher, Peter Börnert, Christoph Leussler, and Johan S Van Den Brink. Transmit sense. *Magnetic Resonance in Medicine: An Official Journal of the International Society for Magnetic Resonance in Medicine*, 49(1):144–150, 2003.
- [30] Peter Ullmann, Sven Junge, Markus Wick, Frank Seifert, Wolfgang Ruhm, and Jürgen Hennig. Experimental analysis of parallel excitation using dedicated coil setups and simultaneous RF transmission on multiple channels. *Magnetic Resonance in Medicine: An Official Journal of the International Society for Magnetic Resonance in Medicine*, 54(4):994–1001, 2005.
- [31] Cem M Deniz. Parallel transmission for ultrahigh field MRI. *Topics in magnetic resonance imaging: TMRI*, 28(3):159, 2019.
- [32] Priti Balchandani, John Pauly, and Daniel Spielman. Designing adiabatic radio frequency pulses using the Shinnar-Le Roux algorithm. *Magnetic resonance in medicine*, 64(3):843–851, 2010.
- [33] Suwit Saekho, Chun-yu Yip, Douglas C Noll, Fernando E Boada, and V Andrew Stenger. Fast-kz three-dimensional tailored radiofrequency pulse for reduced b1 inhomogeneity. *Magnetic Resonance in Medicine: An Official Journal of the International Society for Magnetic Resonance in Medicine*, 55(4):719–724, 2006.
- [34] Kawin Setsompop, Vijayanand Alagappan, Borjan Gagoski, Thomas Witzel, Jonathan Polimeni, Andreas Potthast, Franz Hebrank, Ulrich Fontius, Franz Schmitt, Lawrence L Wald, et al. Slice-selective RF pulses for in vivo b inhomogeneity mitigation at 7 tesla using parallel RF excitation with a 16-element coil. *Magnetic Resonance in Medicine: An Official*

Journal of the International Society for Magnetic Resonance in Medicine, 60(6):1422–1432, 2008.

- [35] William A Grissom, Mohammad-Mehdi Khalighi, Laura I Sacolick, Brian K Rutt, and Mika W Vogel. Small-tip-angle spokes pulse design using interleaved greedy and local optimization methods. *Magnetic resonance in medicine*, 68(5):1553–1562, 2012.
- [36] Kawin Setsompop, Lawrence L Wald, Vijayanand Alagappan, Borjan Gagoski, Franz Hebrank, Ulrich Fontius, Franz Schmitt, and Elfar Adalsteinsson. Parallel RF transmission with eight channels at 3 Tesla. *Magnetic Resonance in Medicine: An Official Journal of the International Society for Magnetic Resonance in Medicine*, 56(5):1163–1171, 2006.
- [37] Eight-channel transmit/receive body MRI coil at 3T, author=Vernickel, P and Röschmann, P and Findekle, C and Lüdeke, K-M and Leussler, Ch and Overweg, J and Katscher, U and Grässlin, I and Schünemann, K, journal=Magnetic Resonance in Medicine: An Official Journal of the International Society for Magnetic Resonance in Medicine, volume=58, number=2, pages=381–389, year=2007, publisher=Wiley Online Library.
- [38] Kawin Setsompop, Lawrence L Wald, Vijayanand Alagappan, Borjan A Gagoski, and Elfar Adalsteinsson. Magnitude least squares optimization for parallel radio frequency excitation design demonstrated at 7 Tesla with eight channels. *Magnetic Resonance in Medicine: An Official Journal of the International Society for Magnetic Resonance in Medicine*, 59(4):908–915, 2008.
- [39] Thomas M Fiedler, Mark E Ladd, and Andreas K Bitz. SAR Simulations & Safety. *NeuroImage*, 168:33–58, 2018.

- [40] Aurelien Massire, Martjin A Cloos, Michel Luong, Alexis Amadon, Alexandre Vignaud, Christopher J Wiggins, and Nicolas Boulant. Thermal simulations in the human head for high field MRI using parallel transmission. *Journal of Magnetic Resonance Imaging*, 35(6):1312–1321, 2012.
- [41] Emre Kopanoglu, Cem M Deniz, M Arcan Erturk, and Richard G Wise. Specific absorption rate implications of within-scan patient head motion for ultra-high field MRI. *Magnetic resonance in medicine*, 84(5):2724–2738, 2020.
- [42] Matthias Hampe. Specific absorption rate in human tissues: Accurate and approximated values. In *2013 International Symposium on Electromagnetic Compatibility*, pages 143–148. IEEE, 2013.
- [43] International Electrotechnical Commission et al. Medical electrical equipment-part 2-33: Particular requirements for the basic safety and essential performance of magnetic resonance equipment for medical diagnosis. *IEC 60601-2-33 Ed. 3.0*, 2010.
- [44] Andreas Christ, Wolfgang Kainz, Eckhart G Hahn, Katharina Honegger, Marcel Zefferer, Esra Neufeld, Wolfgang Rascher, Rolf Janka, Werner Bautz, Ji Chen, et al. The Virtual Family—development of surface-based anatomical models of two adults and two children for dosimetric simulations. *Physics in Medicine & Biology*, 55(2):N23, 2009.
- [45] Frank Seifert, Gerd Wübbeler, Sven Junge, Bernd Ittermann, and Herbert Rinneberg. Patient safety concept for multichannel transmit coils. *Journal of Magnetic Resonance Imaging: An Official Journal of the International Society for Magnetic Resonance in Medicine*, 26(5):1315–1321, 2007.
- [46] Zhangwei Wang, James C Lin, Weihua Mao, Wanzhan Liu, Michael B Smith, and Christopher M Collins. Sar and temperature: simulations and

- comparison to regulatory limits for MRI. *Journal of Magnetic Resonance Imaging: An Official Journal of the International Society for Magnetic Resonance in Medicine*, 26(2):437–441, 2007.
- [47] Fernando Bardati, Antonello Borrani, Annamaria Gerardino, and Giorgio A Lovisolo. SAR optimization in a phased array radiofrequency hyperthermia system. *IEEE Transactions on biomedical engineering*, 42(12):1201–1207, 1995.
- [48] Ingmar Graesslin, Hanno Homann, Sven Biederer, Peter Börnert, Kay Nehrke, Peter Vernickel, Giel Mens, Paul Harvey, and Ulrich Katscher. A specific absorption rate prediction concept for parallel transmission MR. *Magnetic resonance in medicine*, 68(5):1664–1674, 2012.
- [49] Emre Kopanoglu. Patient specific parallel transmit pulses are patient position dependent while safety models are fixed: safety implications. *ISMRM proceedings*.
- [50] Ettore Flavio Meliadó, Alessandro Sbrizzi, Cornelis AT van den Berg, Bart R Steensma, Peter R Luijten, and Alexander JE Raaijmakers. Conditional safety margins for less conservative peak local sar assessment: A probabilistic approach. *Magnetic resonance in medicine*, 84(6):3379–3395, 2020.
- [51] S Malviya, Terri Voepel-Lewis, Odd Petter Eldevik, David T Rockwell, JH Wong, and AR Tait. Sedation and general anaesthesia in children undergoing MRI and CT: adverse events and outcomes. *British journal of anaesthesia*, 84(6):743–748, 2000.
- [52] Jeana E Havidich, Michael Beach, Stephen F Dierdorf, Tracy Onega, Gautham Suresh, and Joseph P Cravero. Preterm versus term children: analy-

- sis of sedation/anesthesia adverse events and longitudinal risk. *Pediatrics*, 137(3), 2016.
- [53] Michael D Mallory, Curtis Travers, Courtney E McCracken, James Hertzog, and Joseph P Cravero. Upper respiratory infections and airway adverse events in pediatric procedural sedation. *Pediatrics*, 140(1), 2017.
- [54] Juan P Boriosi, Jens C Eickhoff, Kristi B Klein, and Gregory A Hollman. A retrospective comparison of propofol alone to propofol in combination with dexmedetomidine for pediatric 3T MRI sedation. *Pediatric Anesthesia*, 27(1):52–59, 2017.
- [55] Stefan T Schwarz, Mohammed Afzal, Paul S Morgan, Nin Bajaj, Penny A Gowland, and Dorothee P Auer. The ‘swallow tail’ appearance of the healthy nigrosome—a new accurate test of parkinson’s disease: a case-control and retrospective cross-sectional MRI study at 3T. *PloS one*, 9(4):e93814, 2014.
- [56] Verinder Prasher, Stuart Cumella, K Natarajan, E Rolfe, Saeed Shah, and MS Haque. Magnetic resonance imaging, down’s syndrome and alzheimer’s disease: research and clinical implications. *Journal of Intellectual Disability Research*, 47(2):90–100, 2003.
- [57] Deanna J Greene, Jessica A Church, Nico UF Dosenbach, Ashley N Nielsen, Babatunde Adeyemo, Binyam Nardos, Steven E Petersen, Kevin J Black, and Bradley L Schlaggar. Multivariate pattern classification of pediatric Tourette syndrome using functional connectivity MRI. *Developmental science*, 19(4):581–598, 2016.
- [58] David C Van Essen, Stephen M Smith, Deanna M Barch, Timothy EJ Behrens, Essa Yacoub, Kamil Ugurbil, Wu-Minn HCP Consortium, et al.

- The WU-Minn human connectome project: an overview. *Neuroimage*, 80:62–79, 2013.
- [59] Emre Kopanoglu, Alix Plumley, Cem M Deniz, Arcan M Erturk, and Richard G Wise. Implications of within-scan patient head motion on b1+ homogeneity and specific absorption rate at 7T. *ISMRM 27th Annual Meeting Exhibition*, 2019.
- [60] R Bammer, B Zhang, W Deng, GC Wiggins, AV Stenger, and DK Sodickson. Impact of motion on parallel transmission. *Proc 19th Scientific Meeting ISMRM*, 2011.
- [61] Qing-San Xiang and R Mark Henkelman. K-space description for MR imaging of dynamic objects. *Magnetic resonance in medicine*, 29(3):422–428, 1993.
- [62] Maxim Zaitsev, Julian Maclaren, and Michael Herbst. Motion artifacts in MRI: A complex problem with many partial solutions. *Journal of Magnetic Resonance Imaging*, 42(4):887–901, 2015.
- [63] Kevin T Chen, Stephanie Salcedo, Daniel B Chonde, David Izquierdo-Garcia, Michael A Levine, Julie C Price, Bradford C Dickerson, and Ciprian Catana. MR-assisted PET motion correction in simultaneous PET/MRI studies of dementia subjects. *Journal of Magnetic Resonance Imaging*, 48(5):1288–1296, 2018.
- [64] Steven Kecsckemeti, Alexey Samsonov, Julia Velikina, Aaron S Field, Patrick Turski, Howard Rowley, Janet E Lainhart, and Andrew L Alexander. Robust motion correction strategy for structural MRI in unsedated children demonstrated with three-dimensional radial mpnrage. *Radiology*, 289(2):509–516, 2018.

- [65] Marco Gemma, Elisa Scola, Cristina Baldoli, Marta Mucchetti, Silvia Pontesilli, Assunta De Vitis, Andrea Falini, and Luigi Beretta. Auditory functional magnetic resonance in awake (nonsedated) and propofol-sedated children. *Pediatric Anesthesia*, 26(5):521–530, 2016.
- [66] Xiaolin Liu, Kathryn K Lauer, B Douglas Ward, Christopher Roberts, Suyan Liu, Suneeta Gollapudy, Robert Rohloff, William Gross, Guangyu Chen, Zhan Xu, et al. Propofol attenuates low-frequency fluctuations of resting-state fMRI BOLD signal in the anterior frontal cortex upon loss of consciousness. *Neuroimage*, 147:295–301, 2017.
- [67] Richard L Ehman and Joel P Felmlee. Adaptive technique for high-definition MR imaging of moving structures. *Radiology*, 173(1):255–263, 1989.
- [68] Xiaoping Hu and Seong-Gi Kim. Reduction of signal fluctuation in functional MRI using navigator echoes. *Magnetic resonance in medicine*, 31(5):495–503, 1994.
- [69] Matthew D Robson, Adam W Anderson, and John C Gore. Diffusion-weighted multiple shot echo planar imaging of humans without navigation. *Magnetic resonance in medicine*, 38(1):82–88, 1997.
- [70] Jason Mendes, Eugene Kholmovski, and Dennis L Parker. Rigid-body motion correction with self-navigation MRI. *Magnetic Resonance in Medicine: An Official Journal of the International Society for Magnetic Resonance in Medicine*, 61(3):739–747, 2009.
- [71] Joseph Y Cheng, Marcus T Alley, Charles H Cunningham, Shreyas S Vasanaawala, John M Pauly, and Michael Lustig. Nonrigid motion correction in 3D using autofocusing with localized linear translations. *Magnetic resonance in medicine*, 68(6):1785–1797, 2012.

- [72] Ruud B van Heeswijk, Gabriele Bonanno, Simone Coppo, Andrew Coristine, Tobias Kober, and Matthias Stuber. Motion compensation strategies in magnetic resonance imaging. *Critical Reviews™ in Biomedical Engineering*, 40(2), 2012.
- [73] Ghislain Vaillant, Claudia Prieto, Christoph Kolbitsch, Graeme Penney, and Tobias Schaeffter. Retrospective rigid motion correction in k-space for segmented radial MRI. *IEEE transactions on medical imaging*, 33(1):1–10, 2013.
- [74] Heidi A Ward, Stephen J Riederer, Roger C Grimm, Richard L Ehman, Joel P Felmlee, and Clifford R Jack Jr. Prospective multiaxial motion correction for fMRI. *Magnetic Resonance in Medicine: An Official Journal of the International Society for Magnetic Resonance in Medicine*, 43(3):459–469, 2000.
- [75] Julian Maclaren, Michael Herbst, Oliver Speck, and Maxim Zaitsev. Prospective motion correction in brain imaging: a review. *Magnetic resonance in medicine*, 69(3):621–636, 2013.
- [76] Emre Kopanoglu. Near real-time parallel-transmit pulse design. *Proceedings of the Joint Meeting of the ISMRM and the ESMRMB*, 3392, 2018.
- [77] Sebastian Schmitter, Xiaoping Wu, Kâmil Uğurbil, and Pierre-François Van de Moortele. Design of parallel transmission radiofrequency pulses robust against respiration in cardiac MRI at 7 Tesla. *Magnetic resonance in medicine*, 74(5):1291–1305, 2015.
- [78] William Grissom, Chun-yu Yip, Zhenghui Zhang, V Andrew Stenger, Jeffrey A Fessler, and Douglas C Noll. Spatial domain method for the design of RF pulses in multicoil parallel excitation. *Magnetic Resonance in Medicine*:

An Official Journal of the International Society for Magnetic Resonance in Medicine, 56(3):620–629, 2006.

- [79] Maxim Zaitsev, Christian Dold, Georgios Sakas, Jürgen Hennig, and Oliver Speck. Magnetic resonance imaging of freely moving objects: prospective real-time motion correction using an external optical motion tracking system. *Neuroimage*, 31(3):1038–1050, 2006.
- [80] E Neufeld, MC Gosselin, D Sczcerba, M Zefferer, and N Kuster. Sim4life: A medical image data based multiphysics simulation platform for computational life sciences. In *Proceedings of the VPH 2012 Congress (VPH 2012)*, 2012.
- [81] Emre Kopanoglu. Actual patient position versus safety models: Specific Absorption Rate implications of initial head position for Ultrahigh Field Magnetic Resonance Imaging. *NMR in Biomedicine*, 36(5):e4876, 2023.
- [82] Andreï Nikolaevich Tikhonov, Vasilii IAkovlevich Arsenin, VY Arsenin, et al. *Solutions of ill-posed problems*. Vh Winston, 1977.
- [83] Fa-Hsuan Lin, Kenneth K Kwong, John W Belliveau, and Lawrence L Wald. Parallel imaging reconstruction using automatic regularization. *Magnetic Resonance in Medicine: An Official Journal of the International Society for Magnetic Resonance in Medicine*, 51(3):559–567, 2004.
- [84] Emre Kopanoglu, Ugur Yilmaz, Yildiray Gokhalk, and Ergin Atalar. Specific absorption rate reduction using nonlinear gradient fields. *Magnetic Resonance in Medicine*, 70(2):537–546, 2013.
- [85] Raphaël Tomi-Tricot, Vincent Gras, Bertrand Thirion, Franck Mauconduit, Nicolas Boulant, Hamza Cherkaoui, Pierre Zerbib, Alexandre Vignaud, Alain Luciani, and Alexis Amadon. Smartpulse, a machine learning

- approach for calibration-free dynamic RF shimming: preliminary study in a clinical environment. *Magnetic Resonance in Medicine*, 82(6):2016–2031, 2019.
- [86] Vincent Gras, Alexandre Vignaud, Alexis Amadon, Denis Le Bihan, and Nicolas Boulant. Universal pulses: a new concept for calibration-free parallel transmission. *Magnetic resonance in medicine*, 77(2):635–643, 2017.
- [87] Ian Goodfellow, Jean Pouget-Abadie, Mehdi Mirza, Bing Xu, David Warde-Farley, Sherjil Ozair, Aaron Courville, and Yoshua Bengio. Generative adversarial nets. *Advances in neural information processing systems*, 27, 2014.
- [88] Gary H Glover and John M Pauly. Projection reconstruction techniques for reduction of motion effects in MRI. *Magnetic resonance in medicine*, 28(2):275–289, 1992.
- [89] James G Pipe. Motion correction with PROPELLER MRI: application to head motion and free-breathing cardiac imaging. *Magnetic Resonance in Medicine: An Official Journal of the International Society for Magnetic Resonance in Medicine*, 42(5):963–969, 1999.
- [90] HP Fautz, M Vogel, P Gross, A Kerr, and Y Zhu. B1 mapping of coil arrays for parallel transmission. In *Proceedings of the 16th Annual Meeting of ISMRM, Toronto, Canada*, volume 1247, 2008.
- [91] Daniel S Marcus, Timothy R Olsen, Mohana Ramaratnam, and Randy L Buckner. The extensible neuroimaging archive toolkit. *Neuroinformatics*, 5(1):11–33, 2007.
- [92] RW Cox. Afni: software for analysis and visualization of functional magnetic resonance neuroimages. *Comput Biomed Res*, 29:162–173, 1996.

- [93] Robert W Cox and James S Hyde. Software tools for analysis and visualization of fMRI data. *NMR in Biomedicine: An International Journal Devoted to the Development and Application of Magnetic Resonance In Vivo*, 10(4-5):171–178, 1997.
- [94] Jinghua Wang, Weihua Mao, Maolin Qiu, Michael B Smith, and R Todd Constable. Factors influencing flip angle mapping in MRI: RF pulse shape, slice-select gradients, off-resonance excitation, and B_0 inhomogeneities. *Magnetic Resonance in Medicine: An Official Journal of the International Society for Magnetic Resonance in Medicine*, 56(2):463–468, 2006.
- [95] Jiaen Liu, Jacco A de Zwart, Peter van Gelderen, Joseph Murphy-Boesch, and Jeff H Duyn. Effect of head motion on MRI B_0 field distribution. *Magnetic resonance in medicine*, 80(6):2538–2548, 2018.